Dissertation
submitted to the
Combined Faculties for the Natural Sciences and for Mathematics
of the Ruperto-Carola University of Heidelberg, Germany
for the degree of
Doctor of Natural Sciences

Put forward by
Dipl.-Phys. Oliver Matula
Born in Winsen (Luhe), Germany
Oral examination: 21.05.2014

Atomic Processes with Twisted Particles:

Photoionization and Radiative Recombination

Referees: Priv.-Doz. Dr. Andrey Surzhykov
Priv.-Doz. Dr. Antonino Di Piazza

Atomic Processes with Twisted Particles:
Photoionization and Radiative Recombination

Twisted photons and electrons are freely-propagating particles that carry orbital angular momentum (OAM) along their propagation direction. These twisted particles currently attract considerable interest in both fundamental and applied research and extensive studies have been performed to explore their basic properties and potential applications. In particular, much attention has been focused on how the "twistedness" of a particle may affect its interaction with light and matter. Two fundamental processes that can provide substantial insights into this (light-matter) interaction are the *photoionization* of atoms or ions as well as its (time-reversed) counterpart: *radiative recombination*.

In this work, we develop a novel theoretical formalism to study (a) the ionization of hydrogen-like ions by twisted photons and (b) the radiative capture of twisted electrons by bare ions. For both processes, special attention is paid to the properties of the emitted particles—photons and electrons—as characterized by their angular distribution or polarization state. Calculations are performed based on the non-relativistic first-order perturbation theory and the density matrix approach. The obtained results show that the OAM of the incident twisted particle beam may significantly affect the properties of the outgoing particles in both, the ionization (a) and the recombination process (b). We demonstrate that such (OAM-dependent) effects can be observed most easily in the so-called *non-paraxial* beam regime where the magnitude of the transverse linear momentum of the incoming beam is of the same order as the longitudinal one.

Atomare Prozesse mit getwisteten Teilchen:
Photoionisation und Radiative Rekombination

Getwistete Photonen und Elektronen sind frei propagierende Teilchen, die einen Bahndrehimpuls entlang der Propagationsrichtung besitzen. Diese getwisteten Teilchen erwecken zur Zeit großes Interesse in der fundamentalen sowie angewandten Forschung und zahlreiche Studien wurden durchgeführt, um die grundsätzlichen Eigenschaften und die potentiellen Anwendungen dieser Teilchen zu erkunden. Insbesondere wurde viel Aufmerksamkeit darauf gelenkt, wie der "Twist" eines Teilchens die Wechselwirkung mit Licht und Materie beeinflussen kann. Zwei fundamentale Prozesse, die wesentliche Einsichten in diese (Licht-Materie) Wechselwirkung liefern können, sind die *Photoionisation* von Atomen oder Ionen sowie ihr (zeitinvertiertes) Gegenstück, die radiative Rekombination.
In dieser Arbeit entwickeln wir einen neuartigen theoretischen Formalismus um (a) die Ionisation von wasserstoffähnlichen Ionen durch getwistete Photonen und (b) den radiativen Einfang getwisteter Elektronen durch "nackte" Ionen zu studieren. Für beide Prozesse werden insbesondere die Eigenschaften der emittierten Photonen bzw. Elektronen betrachtet wie z.B. ihre Winkelverteilung oder ihr Polarisationszustand. Die zugehörigen Rechnungen basieren auf der nicht-relativistischen Störungstheorie erster Ordnung und auf dem Dichtematrixansatz. Die erlangten Resultate zeigen, dass der Bahndrehimpuls des einlaufenden getwisteten Teilchenstrahls die emittierten Teilchen im (a) Ionisations- oder (b) Rekombinationsprozess signifikant beeinflussen kann. Solche vom Bahndrehimpuls abhängigen Effekte können am einfachsten im nicht-paraxialem Strahlregime beobachtet werden, in dem der lineare Transversalimpuls des einlaufenden Strahls von der selben Größenordnung wie der longitudinale Impuls ist.

Publications

The author has contributed to the following publications

- O. Matula, S. Fritzsche, F. J. Currell and A. Surzhykov, "Angular correlations in radiative cascades following resonant electron capture by highly charged ions", Phys. Rev. A **84**, 052723 (2011).

- O. Matula, S. Fritzsche and A. Surzhykov, "Polarization correlations in radiative cascades following dielectronic recombination with high-Z ions", J. Phys. B **45**, 215004 (2012).

- O. Matula, S. Fritzsche and A. Surzhykov, "Polarization correlations between photons emitted in dielectronic recombination of high-Z ions", Phys. Scr. **T156**, 014051 (2013).

- A. G. Hayrapetyan, O. Matula, A. Surzhykov, S. Fritzsche, "Bessel beams of two-level atoms driven by a linearly polarized laser field", Eur. Phys. J. D **10**, 1140 (2013).

- O. Matula, A. G. Hayrapetyan, V. G. Serbo, A. Surzhykov and S. Fritzsche, "Atomic ionization of hydrogen-like ions by twisted photons: angular distribution of emitted electrons", J. Phys. B **46**, 205002 (2013).
  - Press coverage: E. Cartlidge, *How light can put atoms in a twist*, accessed January 12, 2014, "http://physicsworld.com/cws/article/news/2013/oct/15/how-light-can-put-atoms-in-a-twist".
  - Selected by Journal of Physics B as one of the highlights of the year 2013.

- A. G. Hayrapetyan, O. Matula, A. Aiello, A. Surzhykov and S. Fritzsche, "Interaction of relativistic electron vortex beams with few-cycle laser pulses", *to be published in* Phys. Rev. Lett.

- O. Matula, A. G. Hayrapetyan, V. G. Serbo, A. Surzhykov and S. Fritzsche, "Radiative capture of twisted electrons by bare ions", arXiv:1401.1646 (2014), *submitted to* New J. Phys.

Contents

1. Introduction

In 1909 Poynting proposed that circularly polarized light carries an intrinsic angular momentum of magnitude $\hbar$ along or counter to its propagation direction [1]. About 30 years later Beth experimentally confirmed this statement by measuring the torque exerted onto a half-wave plate by such a circularly polarized light beam [2]. Nowadays the so-called *spin angular momentum* (SAM) of light is employed in many different applications such as optical cooling and trapping of atoms [3, 4], quantum computing [5], quantum cryptography [6, 7] and 3D-cinema systems [8].

Contrary to the long history of SAM, it was discovered only recently that light beams in vacuum may also possess a well-defined projection of *orbital angular momentum* (OAM) along their propagation direction [9,10]. These beams are commonly referred to as *twisted* or *vortex* light beams. As shown by Allen and coworkers [9,10], the OAM $\hbar m$ along the propagation direction of such a vortex beam originates from a helical phase dependency $\exp(\mathrm{i}m\varphi)$ around the beam center. The values of m, also called the topological charge of the beam, are only restricted by the requirement that the phase factor is single-valued. Thus m can be of any integer value $0, \pm 1, \pm 2, \ldots$, so that the OAM state space of a vortex beam is theoretically infinite-dimensional. This is in stark contrast to the two-dimensional SAM state space of a "standard" (circularly polarized) light beam.

The helical phase factor $\exp(\mathrm{i}m\varphi)$ imposes severe restrictions on the intensity distribution of the light beam. That is, in order to avoid a discontinuity of the phase factor within the beam center for a non-zero topological charge m, it inevitably follows that the central intensity of the light beam must vanish. This dark central line of a twisted light beam is also denoted as its vortex.

There exists a variety of different methods to produce twisted light beams in the laboratory. All of these methods rely on specially designed devices such as astigmatic mode converters [10], spiral phase plates [11], Q-plates [12, 13], axicons [14], (nonlinear) crystals [15], ring resonators [16] or helical undulators [17, 18]. But probably the most widely used device is the diffraction grating [19–24]. This is due to the fact that nowadays such gratings can be realized by spatial light modulators (SLMs). A SLM is a device that can impose an arbitrary spatial (phase or intensity) modulation onto an incident light beam. The exact form of the modulation is controlled by an external signal, e.g. electronically with a computer. The SLM can be configured in such a way that the resulting light beam exhibits the characteristic phase factor $\exp(\mathrm{i}m\varphi)$ and is therefore twisted. This can be accomplished, for example, if one im-

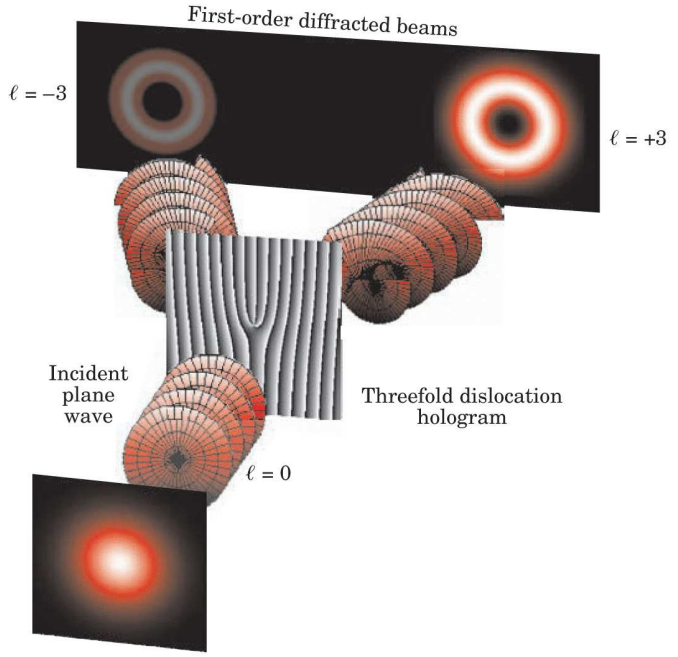

Figure 1.1. – Creation of vortex light beams. A TEM_{00} is impinged onto a diffraction grating with a fork-like dislocation in the center. Depending on the order l of the grating's dislocation (here threefold corresponding to $l = 3$), one obtains vortex light beams with topological charge $-l$ or $+l$ for the first-order diffraction patterns. Image has been taken from [24].

pinges an ordinary transverse electromagnetic ground mode (TEM_{00}) as originating from a standard laser onto a SLM that mimics a diffraction grating with a fork-like slit structure as shown in Fig. 1.1.

The topological charge of the emerging twisted light beam depends crucially on the number of (dislocated) extra slits in the upper half plane of the fork-like diffraction grating with respect to its lower half plane. This number is also called the order of the fork-like dislocation. For example, the first-order diffracted light beams carry a topological charge that is (up to a sign) exactly equal to the order of the grating's dislocation (cf. Fig. 1.1). Since one can easily vary the order of the dislocation with the help of a SLM, one obtains access to a wide range of different OAM states. An OAM along the beam's propagation direction of up to a few hundred $\hbar$ can be created with such types of diffraction gratings [23]. We note, moreover, that there exist other efficient techniques to create twisted light beams with an even higher OAM along the propagation direction (up to $5000\,\hbar$) [25], but in contrast to the methods that use SLMs, these techniques do not allow for a dynamic control of the OAM state.

The creation of vortex light beams with the help of diffraction gratings does not work equally well for all wave lengths. In order to produce a grating that operates

properly, the spatial width of the slits embedded in the grating material has to be comparable to the wave length of the incident light. This is easily realizable for visible light that has a wavelength in the submicrometer regime. But for the generation of extreme ultraviolet (EUV) or even x-ray twisted light, one should turn to different methods. For instance, it is possible to produce high-energetic twisted light at a synchrotron facility by placing a special construct of planar and helical undulators within the beam line of its particle accelerator [17, 18]. Moreover, it has been proposed that the Compton back-scattering of twisted optical light on ultra-relativistic electrons can be utilized to produce vortex light beams not only in the EUV or x-ray domain but also in the energy region of GeV [26, 27].

Over the last decades extensive studies have been performed, both in experiment and theory, to understand the physical properties of vortex light beams. In particular, these investigations revealed that the well-defined OAM along the propagation axis is not only a characteristic property of the total beam but also of each individual photon [28–30]. Moreover, in analogy to SAM-entangled photons [31–33], a pair of *twisted* photons can also exhibit quantum entanglement between their OAM components [34–36]. For OAM states $|-l\rangle$ and $|+l\rangle$ with opposite topological charge l, it was demonstrated experimentally by Zeilinger and coworkers that an entanglement can be achieved even up to $l = 300$ [36].

Apart from the fundamental properties of vortex light beams, much attention has been paid to their applications. For example, the scattering of twisted photons from a spinning object leads to a frequency shift of the on-axis scattered light that can be employed to determine the object's rotation velocity [37]. Vortex light beams applied in an optical tweezer cannot only trap microparticles but also set them into a particular rotation state, thus generating some kind of micro-motor [38, 39]. Furthermore, a debate is currently going on to clarify if twisted photons can be used to boost data transmission rates [40–43]. One could certainly extend the list of examples presented here much more. However, already the small selection shown above makes it clear that twisted photons have opened up new and exciting possibilities in many different research areas in the last years.

Photons are particles without a rest mass and without an electric charge. However, the nature of a quantum state to be twisted is not restricted by these properties. It has been theoretically proposed therefore that electrons can also exist as a twisted state [44]. Only a few years ago, the experimental verification of this prediction has been carried out [45, 47]. In these studies, similar devices as for the production of twisted photons have been used to generate the twisted electron state such as spiral phase plates [45, 46] or diffraction gratings [47–50]. This portability of the well-established techniques is possible because of the wave nature of the electrons as characterized by the wave-particle duality. At present, such methods allow to produce twisted electrons with an energy of up to 300 keV and with a topological charge as high as 90 [51] or 100 [52].

Twisted electrons carry an electrical charge and are thus influenced by electromagnetic fields. Such an electromagnetic interaction can be sensitive to the OAM state of the electron beam. In particular, twisted electrons moving in a uniform or a delta-like magnetic field that is aligned with the center of the electron beam exhibit modified Landau and Aharonov-Bohm levels, respectively [53, 54]. A superposition of electron vortex beams with different topological charges experiences a spatial rotation in a uniform magnetic field known as the vacuum Faraday effect [55]. Furthermore, twisted electrons passing through some special arrangement of magnetic lenses can undergo novel Larmor and Gouy rotations [56, 57].

As illustrated above, twisted photons and electrons possess unique properties that are extensively studied nowadays, particularly with regard to novel applications. Most studies, however, focus either on the fundamental understanding of these particles or on their interaction with mesoscopic and macroscopic systems [53–59]. Only a few investigations exist up to now that consider processes with twisted particles on the atomic level. Here one has to mention the work of Babiker *et al.* [60] or Afanasev and coworkers [61] who explored the radiative excitation of atoms by twisted photons and analyzed the related OAM exchange. The scattering process of twisted photons and electrons on atomic systems has been studied in [62] and [63, 64], respectively. A group in Spain, moreover, analyzed the electron dynamics for the ionization of hydrogen atoms by twisted Laguerre-Gaussian light beams [65, 66]. Laguerre-Gaussian beams, however, are so-called *paraxial* beams, that is, the light waves that compose these beams have to possess a momentum transverse to their propagation direction that is much smaller than the longitudinal one [67]. Recently we performed a *complementary study of the photoionization process* [68] that greatly extended the previous work by employing Bessel light waves—light waves whose magnitude of the transverse momentum is not restricted and which can exist, therefore, in a *non-paraxial* state. Our work was also covered by the media [69] and has been selected by Journal of Physics B as one of the highlights of the year 2013. In the first half of this thesis, we will report in detail on this study.

Photoionization of ions and atoms is one of the fundamental processes in atomic physics [70–73]. Therefore a large number of studies have been performed to investigate its total ionization cross sections and their dependence on photon energy as well as on the electronic configuration of the atoms [74–77]. Such studies are not only of fundamental interest but are also required to understand the formation of charge state distributions in stellar as well as laboratory plasmas [78]. Apart from the total rates, much attention has been focused on the angular distribution of the photoelectrons [79–82]. These angle-differential studies are often more sensitive to the electronic structure of the atoms or ions, and have yielded important insights on relativistic, many-electron or quantum electrodynamical (QED) effects in the basic photon-electron interaction.

As mentioned above, studies of the photoionization process have revealed important details on the fundamental interaction of light with matter. To gain additional insights into such an interaction, it can be very rewarding to explore also the time-reversed atomic photoionization process: *radiative recombination* of electrons with ions. Especially for high-Z ions, where photon sources with a sufficiently high energy for inner-shell ionization of atoms are sparse, an analysis of the radiative recombination process is much more feasible. Studies of both processes, photoionization and radiative recombination, are therefore necessary to gain the most information about atomic systems, their dynamics and the underlying light-matter interactions. Therefore many studies have been performed at storage ring and electron beam ion trap facilities to analyze the *total capture rates* as well as the *angular emission pattern* and *polarization state* of the emitted RR photons for different ionic systems and collision energies [83–94]. As expected, these studies provided valuable, supplementary information on relativistic, many-body or QED effects in the dynamics of electrons and photons.

RR investigations are usually restricted to "standard" plane wave electron beams—beams that do not carry an OAM along their propagation direction. A new *degree of freedom* as given by a non-zero (projection of) OAM can be introduced to the RR studies by using *twisted* instead of plane wave electron beams. The great advantage of such beams is that they may allow to explore the basic role of OAM for the electron-photon interaction. In the second part of this thesis, we will therefore perform a complementary study to the atomic ionization process with twisted photons and analyze the radiative recombination process with twisted electrons.

More specifically, in this thesis we will develop a novel theoretical formalism to analyze the properties of (a) electrons that are emitted in the photoionization process of hydrogen-like ions by twisted photons and of (b) photons that are emitted in the radiative capture of twisted electrons by initially bare ions. To do so, we first need to introduce how we describe the (plane and twisted) particles—photons and electrons—that enter these processes. For photons, this will lead us in Chapter 2 to Maxwell's theory of light. Electrons instead will be characterized in Chapter 3 with the help of Schrödinger's equation. We note that for both, photons and electrons, we will pay special attention to one particular kind of twisted state, the so-called (twisted) *Bessel waves*.

To describe the processes of photoionization and radiative recombination, it is not sufficient to only characterize the states of the (initial and final) particles. We must also know how these particles interact, how we can describe their dynamics for the process in question. In Chapter 4, we will present a well-elaborated method for such a description: the *time-dependent first-order perturbation-theory*. Ultimately, this formalism is based on one entity—the so-called *transition amplitude*—that is central for the description of both processes, the atomic photoionization and the radiative recombination.

After we have collected the basic ingredients—the particle states "plus" the description of their dynamics in terms of the transition amplitudes—we are ready to develop the theoretical formalism for the analysis of the ionization and recombination process. In Chapter 5, we will begin to discuss the ionization process of ions and atoms by twisted photons, in particular for the simplest atomic systems: hydrogen-like ions. There we will especially focus on the properties of the emitted (photo)electrons and provide a detailed analysis of their (angle-differential) *emission pattern* in terms of the corresponding transition amplitudes. However, as a proper starting point for such an analysis, we will first remind the reader how one usually derives the transition amplitudes for photoionization processes with *plane electromagnetic waves*, and how these transition amplitudes can be used in this case to describe the angular distribution of the photoelectrons. This treatment of the plane wave photoionization will provide an appropriate bridge for the analysis of the ionization process with twisted photons. For such a process, we will again first explore the associated transition amplitudes that describe the ionization of the (hydrogen-like) ions by twisted photons. These amplitudes will then serve to characterize the *angular distribution* of the photoelectrons that emerge from the ionization process with twisted photons. We note moreover that our analysis of the atomic ionization with twisted photon beams will go *beyond* the usual *paraxial beam regime*, a regime where the transverse momentum of the beam is much smaller than its longitudinal one. Our analysis of the photoionization process is applicable for arbitrary ratios of the transverse and longitudinal momenta of a twisted electron beam and, hence, also valid in the *non-paraxial* regime.

In addition to the atomic photoeffect of hydrogen-like ions by twisted photons, we will discuss its cross-channel in Chapter 6: the radiative capture of twisted electrons by bare ions. There we will proceed similar as for the ionization process with twisted photons, and will first introduce how one derives the well-known formulas for the radiative recombination process with *plane wave* electrons. Afterwards, we will proceed to calculate the transition amplitudes that describe the radiative capture of twisted electrons by bare ions. These amplitudes provide the basic building blocks of our theory, since they will serve to characterize both, the *angular distribution* as well as the *polarization state* of the emitted photoelectrons. As for the ionization process, our formalism is again valid in both, the *paraxial* and *non-paraxial* regime of the twisted electron beam.

In Chapter 7, we will then apply our theoretical formalism to study the ionization process of *hydrogen atoms* by twisted (Bessel) photons. In particular, we will investigate two ionization scenarios: (i) the hydrogen atom initially resides in the $1s$ ground state or (ii) the hydrogen atom is initially in the "strongly-oriented" $2p_y$-state. Moreover, special attention is paid in this analysis to the role of the atom position with respect to the beam center of the incoming twisted light beam. Regardless of the initial state, we find that the position of the atom with respect to the center of the light beam significantly affects the ionization process, as can be seen, for example,

from the shape of the angular photoelectron distribution. For both scenarios, (i) and (ii), we explicitly show that when the atom is close to the beam center, the emission pattern of the photoelectrons will be completely different than the one that corresponds to the ionization process with plane wave beams. Far away from the beam center, however, the ionization process with twisted photons behaves as the one with plane wave photons. Detailed explanations for such a behavior will be given within the chapter.

In Chapter 8, we will discuss the radiative capture of twisted electrons into the K-shell of (finally) hydrogen atoms. In particular, we study such a process for the case where a twisted electron beam collides with a *macroscopic* ion beam whose density distribution in the planes perpendicular to the propagation direction follows a Gaussian function. For this scenario it is demonstrated how the angular distribution as well as the polarization of the recombination photons depend on the parameters of the incoming electron beam. We find that the angular and polarization properties of the emitted photons are sensitive to both, the transverse momentum of the photon beam as well as its topological charge. To observe especially the effects of the topological charge on these (angular and polarization) properties, we propose an experiment that relies on the coherent superposition of two twisted electron beams.

Finally, we will provide a summary of the main results and an outlook in Chapter 9.

Hartree atomic units $m_e = e = \hbar = 4\pi\epsilon_0 = 1$ are used throughout this work unless stated otherwise. Here m_e is the electron rest mass, e the electron charge, $\hbar$ the reduced Planck's constant and ϵ_0 the electric permittivity in vacuum. In this system of units the speed of light is $c = 1/\alpha$ with the electromagnetic fine-structure constant $\alpha \approx 1/137$. Symbols in **bold** denote vector quantities and symbols with a hat $\wedge$ denote operators. The most important relations are encircled by a $\boxed{\text{box}}$.

2. Theoretical Description of Photons: Maxwell's Theory of Light

When we analyze an atomic process—whether in experiment or theory—we always have to specify three steps: (i) how we prepare the initial states of the occurring particles, (ii) how the particles interact, and (iii) how we measure the final states of the outgoing particles. In the next two chapters, we will especially focus on the initial and final states of the particles that are relevant for the atomic photoionization and radiative recombination process. More specifically, we will characterize the *plane wave* and *twisted wave* states of photons and electrons as well as the *hydrogenic* bound states of electrons. For the photon states, this requires to provide a brief introduction to *Maxwell's theory of light* (this chapter), whereas for the electron states we need to introduce *Schrödinger's equation* (Chapter 3).

2.1. Maxwell's Equations

All states of light are characterized by Maxwell's equations [95–97]. Within the vacuum, these equations read

$$\nabla \cdot \mathbf{E}(\mathbf{r}, t) = 0, \tag{2.1}$$

$$\nabla \cdot \mathbf{B}(\mathbf{r}, t) = 0, \tag{2.2}$$

$$\nabla \times \mathbf{E}(\mathbf{r}, t) = -\frac{\partial \mathbf{B}(\mathbf{r}, t)}{\partial t}, \tag{2.3}$$

$$\nabla \times \mathbf{B}(\mathbf{r}, t) = \alpha^2 \, \frac{\partial \mathbf{E}(\mathbf{r}, t)}{\partial t}, \tag{2.4}$$

where

$$\mathbf{E}(\mathbf{r}, t) = \big(E_x(\mathbf{r}, t),\, E_y(\mathbf{r}, t),\, E_z(\mathbf{r}, t)\big)^T \tag{2.5}$$

is the electric and

$$\mathbf{B}(\mathbf{r},t) = \big(B_x(\mathbf{r},t),\, B_y(\mathbf{r},t),\, B_z(\mathbf{r},t)\big)^T \tag{2.6}$$

the magnetic field of the light. These fields are allowed to be complex for reasons of mathematical convenience, but it is only their real part

$$\boldsymbol{\mathcal{E}}(\mathbf{r},t) = \mathrm{Re}\,\mathbf{E}(\mathbf{r},t), \quad \boldsymbol{\mathcal{B}}(\mathbf{r},t) = \mathrm{Re}\,\mathbf{B}(\mathbf{r},t) \tag{2.7}$$

that is physically observable. Furthermore, the quantities $\mathbf{r} = (x,y,z)^T$ and t in Eqs. (2.1)–(2.7) denote the spatial and time coordinates, $\times$ denotes the cross and $\cdot$ the scalar product between two vectors, and $\nabla = \partial/\partial\,\mathbf{r}$ is the directional derivative. To solve Eqs. (2.1)–(2.4), one usually re-writes the electric and magnetic fields in terms of a scalar $\phi(\mathbf{r},t)$ and a vector potential $\mathbf{A}(\mathbf{r},t)$:

$$\mathbf{E}(\mathbf{r},t) = -\nabla\phi(\mathbf{r},t) - \frac{\partial\mathbf{A}(\mathbf{r},t)}{\partial t}, \tag{2.8}$$

$$\mathbf{B}(\mathbf{r},t) = \nabla\times\mathbf{A}(\mathbf{r},t). \tag{2.9}$$

Relations (2.8)–(2.9) do not unambiguously determine the functions $\phi(\mathbf{r},t)$ and $\mathbf{A}(\mathbf{r},t)$, since a gauge transformation of the form

$$\mathbf{A}(\mathbf{r},t) \to \mathbf{A}'(\mathbf{r},t) = \mathbf{A}(\mathbf{r},t) + \nabla\chi(\mathbf{r},t), \tag{2.10}$$

$$\phi(\mathbf{r},t) \to \phi'(\mathbf{r},t) = \phi(\mathbf{r},t) - \frac{\partial\chi(\mathbf{r},t)}{\partial t}, \tag{2.11}$$

with an arbitrary scalar function $\chi(\mathbf{r},t)$ leaves the electric and magnetic fields (2.5)–(2.6) invariant. We can choose the function $\chi(\mathbf{r},t)$ in such a way that

$$\phi(\mathbf{r},t) = 0,\ \nabla\cdot\mathbf{A}(\mathbf{r},t) = 0. \tag{2.12}$$

Such a choice constitutes the so-called Coulomb gauge [96], which we will use exclusively from now on.

The introduction of the scalar and vector potentials (2.8)–(2.9) has the great advantage that the form of Maxwell's equations (2.1)–(2.4) significantly simplifies. By inserting the defining relations (2.8)–(2.9) for the potentials into Maxwell's equations (2.1)–(2.4) and by adopting the Coulomb gauge (2.12), we are left with a simple differential equation for the vector potential

$$\nabla^2 \mathbf{A}(\mathbf{r},t) - \alpha^2 \, \frac{\partial^2 \mathbf{A}(\mathbf{r},t)}{\partial t^2} = 0. \tag{2.13}$$

As seen from expression (2.13), each component of the vector potential $\mathbf{A}(\mathbf{r},t)$ is independently characterized by a wave equation

$$\nabla^2 A_j(\mathbf{r},t) - \alpha^2 \, \frac{\partial^2 A_j(\mathbf{r},t)}{\partial t^2} = 0, \;\; j = x,y,z. \tag{2.14}$$

An interconnection between the different components of $\mathbf{A}(\mathbf{r},t)$ arises, however, from the gauge condition (2.12). As will be seen later (cf. Sec. 2.3), this interconnection imposes severe restrictions on the form of the vector potential $\mathbf{A}(\mathbf{r},t)$.

In comparison to Maxwell's original equations (2.1)–(2.4), the wave equation (2.13) together with the gauge condition (2.12) provide a completely equivalent but much simpler form for the description of light fields in vacuum. They serve not only as a basis to characterize the plane but also the twisted light waves. To further advance in the theoretical description of these states, we will go to the frequency-momentum space—sometimes also named reciprocal or Fourier space—by using the following Fourier transformations [98]:

$$\widetilde{\mathbf{A}}(\mathbf{p},\omega) = (2\pi)^{-3/2} \int \mathbf{A}(\mathbf{r},t) \, \mathrm{e}^{-\mathrm{i}\,(\mathbf{p}\cdot\mathbf{r}-\omega\, t)} \, \mathrm{d}t \, \mathrm{d}^3\mathbf{r}, \tag{2.15}$$

$$\mathbf{A}(\mathbf{r},t) = (2\pi)^{-3/2} \int \widetilde{\mathbf{A}}(\mathbf{p},\omega) \, \mathrm{e}^{\mathrm{i}\,(\mathbf{p}\cdot\mathbf{r}-\omega\, t)} \, \mathrm{d}\omega \, \mathrm{d}^3\mathbf{p}. \tag{2.16}$$

Here $\mathbf{p}$ and ω represent the momentum and frequency coordinates within the Fourier space. At first, the introduction of the additional transformations (2.15)–(2.16) may seem like an unnecessary hurdle and one could well ask why we do not continue our discussion on the normal rather than the Fourier-transformed vector potential. However, there are many properties such as the angular momentum of a light field that are easier to describe within the Fourier space. We will therefore perform the basic construction of the vector potential for the plane and also for the twisted electromagnetic waves in the frequency-momentum space. Once this construction is finished, however, we will transform the vector potential $\widetilde{\mathbf{A}}(\mathbf{p},\omega)$ from the Fourier space back to the position-time coordinates by the help of Eq. (2.16).

By plugging relation (2.16) into Eq. (2.13), one obtains the wave equation within the frequency-momentum space:

$$(\mathbf{p}^2 - \alpha^2 \, \omega^2) \, \widetilde{\mathbf{A}}(\mathbf{p},\omega) = 0. \tag{2.17}$$

Expression (2.17) is a simple algebraic equation for the Fourier-transformed vector potential $\widetilde{\mathbf{A}}(\mathbf{p},\omega)$. The structure of this equation shows that $\widetilde{\mathbf{A}}(\mathbf{p},\omega)$ must be zero everywhere except for the points where $\mathbf{p}^2 = \alpha^2\,\omega^2$. In other words, this relation shows that the frequency ω is (up to a sign) completely defined by the absolute value of the linear momentum vector:

$$\omega_{\pm}(p) = \pm\, p/\alpha, \quad p = |\mathbf{p}|\,. \tag{2.18}$$

If we neglect the sign, moreover, we can interpret Eq. (2.18) as the well-known dispersion relation [96, cf. Eq. (7.4)] of a light field in vacuum

$$\omega(p) = p/\alpha. \tag{2.19}$$

Taking now relation (2.17) into account, it follows that the vector potential within the Fourier space is of the form

$$\widetilde{\mathbf{A}}(\mathbf{p},\omega) = \delta(\mathbf{p}^2 - \alpha^2\,\omega^2)\,\mathbf{a}(\mathbf{p},\omega)\,. \tag{2.20}$$

Here the delta distribution $\delta(\mathbf{p}^2-\alpha^2\,\omega^2)$ ensures that the frequency of the light field is determined by relation (2.18). Furthermore, we have introduced the vector function $\mathbf{a}(\mathbf{p},\omega)$ in Eq. (2.20) to characterize all remaining dependencies of $\widetilde{\mathbf{A}}(\mathbf{p},\omega)$ on $\mathbf{p}$ and ω.

One can use the following property [71, cf. Eq. (2.33g)]

$$\delta\big(h(x)\big) = \sum_k \frac{\delta(x-x_k)}{\big|h'(x_k)\big|} \tag{2.21}$$

of the delta distribution to further simplify Eq. (2.20) for the vector potential. In Eq. (2.21), the x_k denote the roots of the function $h(x)$, whereas $h'(x)$ is the first derivative of $h(x)$. With the help of Eq. (2.21), one may write

$$\delta(\mathbf{p}^2 - \alpha^2\,\omega^2) = \frac{\delta(p-\alpha\,\omega)}{2\,p} + \frac{\delta(p+\alpha\,\omega)}{2\,p} \tag{2.22}$$

and thus arrives at the following form of the vector potential:

$$\widetilde{\mathbf{A}}(\mathbf{p},\omega) = \frac{\delta(p-\alpha\,\omega)}{2\,p}\,\mathbf{a}(\mathbf{p},+\omega(p)) + \frac{\delta(p+\alpha\,\omega)}{2\,p}\,\mathbf{a}(\mathbf{p},-\omega(p)). \tag{2.23}$$

It can be seen from Eq. (2.23) that the vector potential $\widetilde{\mathbf{A}}(\mathbf{p},\omega)$ consists of two parts. The main difference between these two parts is that the associated frequencies have an opposite sign. It is sufficient, therefore, to deal with only one of the terms in Eq. (2.23), since the other can be re-obtained if necessary by inverting the sign of the frequency $\omega(p)$. Let us restrict ourselves from now on to the first term with the positive frequency and rewrite Eq. (2.23) as

$$\widetilde{\mathbf{A}}(\mathbf{p},\omega) = \delta(p - \alpha\,\omega)\,\widetilde{\mathbf{a}}(\mathbf{p}), \tag{2.24}$$

where we have combined the dependency on $\mathbf{p}$ into the function

$$\widetilde{\mathbf{a}}(\mathbf{p}) = \frac{\mathbf{a}(\mathbf{p},+\omega(p))}{2\,p}. \tag{2.25}$$

The vector potential $\widetilde{\mathbf{A}}(\mathbf{p},\omega)$ is subject to a further restriction that originates from the gauge condition (2.12). If we write the gauge condition (2.12) within the frequency-momentum space, we obtain

$$\mathbf{p}\cdot\widetilde{\mathbf{A}}(\mathbf{p},\omega) = 0. \tag{2.26}$$

The vector potential $\widetilde{\mathbf{A}}(\mathbf{p},\omega)$ must therefore always be orthogonal to the linear momentum $\mathbf{p}$. Condition (2.26) is also known as the transversality property of an electromagnetic wave [71].

Up to now, the construction of the potential $\widetilde{\mathbf{A}}(\mathbf{p},\omega)$ as given by Eq. (2.24) is most general and not restricted to a particular state of light. In the next section we will show how to obtain this potential for the special case of a plane electromagnetic wave. Afterwards, we will proceed with the more complicated derivation of $\widetilde{\mathbf{A}}(\mathbf{p},\omega)$ for a twisted light wave.

2.2. Plane Electromagnetic Waves: Construction of Vector Potential

The wave equation (2.17) together with the transversality condition (2.26) provide the general basis for the description of any light state in terms of the vector potential $\widetilde{\mathbf{A}}(\mathbf{p},\omega)$. To recover a special type of solutions of these equations, one has to impose additional restrictions onto the vector potential $\widetilde{\mathbf{A}}(\mathbf{p},\omega)$. This can be done, for example, by requiring that $\widetilde{\mathbf{A}}(\mathbf{p},\omega)$ is a simultaneous eigenfunction to a set of appropriate operators. It is a necessary condition, of course, that these operators mutually commute with each other in order to ensure that such a simultaneous eigenfunction exists. In the following, let us elaborate on how such a set of operators should look like for the case of plane electromagnetic waves.

2.2.1. Linear Momentum of Plane Waves

Plane electromagnetic waves are states of light that possess a well-defined linear momentum denoted in the following as $\mathbf{k}$. Their vector potential must therefore be an eigenstate to each component $\widehat{p}_j$, $j = x, y, z$, of the momentum operator with the associated eigenvalue k_j. Within reciprocal space, where the momentum operator acts component-wise just as a multiplication ($\widehat{p}_j = p_j$, $j = x, y, z$), such an eigenstate can be represented by a simple delta distribution:

$$\widehat{p}_j \, \delta^3(\mathbf{p} - \mathbf{k}) = k_j \, \delta^3(\mathbf{p} - \mathbf{k}). \tag{2.27}$$

The delta distribution $\delta^3(\mathbf{p}-\mathbf{k})$ can therefore be used to mathematically describe the linear momentum of a plane wave. Before we do so, however, we must also discuss the polarization properties of the plane waves.

2.2.2. Polarization of Plane Electromagnetic Waves

Apart from a well-defined linear momentum $\mathbf{k}$, plane electromagnetic waves also possess a particular polarization. The polarization of a light wave characterizes how the directions of the (physically observable) electric and magnetic field vectors (see Eq. (2.7)) change in time. There exists, of course, a huge variety of polarization states that a plane electromagnetic wave can be in such as elliptical, circular or linear polarization. The only restriction for these states is that the associated vector potential has to comply with the transversality condition (2.26).

In this work, we are especially interested in the structure of circularly polarized light waves, since they will be employed later to construct the vector potential of twisted photons. The electric (and also the magnetic) field vector of such circularly polarized waves performs, as time progresses, a circular motion around the wave's propagation direction (which is given by the momentum $\mathbf{k}$ of the wave). The rotation of the electric field vector may either be clockwise or counter-clockwise if one looks in the direction of the wave's momentum $\mathbf{k}$. The case of a clockwise rotation is referred to as right-handed, whereas the counter-clockwise rotation is called left-handed (some references also define right- and left-handed the other way round). We illustrate this definition graphically in Fig. 2.1. The construction of the vector potential that corresponds to such spiraling electric fields will be done in the following.

It is well-known [1,96,99] that the circular polarization of a plane electromagnetic wave originates from a spin angular momentum (SAM) of $\pm\hbar$ along its propagation direction. If the projection of spin is aligned (counter-aligned) with the propagation direction, the electric field performs a clockwise (counter-clockwise) rotation. Such a projection of SAM onto the propagation direction is usually called *helicity* [96]. To describe these helicity states, we need to introduce the explicit form of the (vectorial)

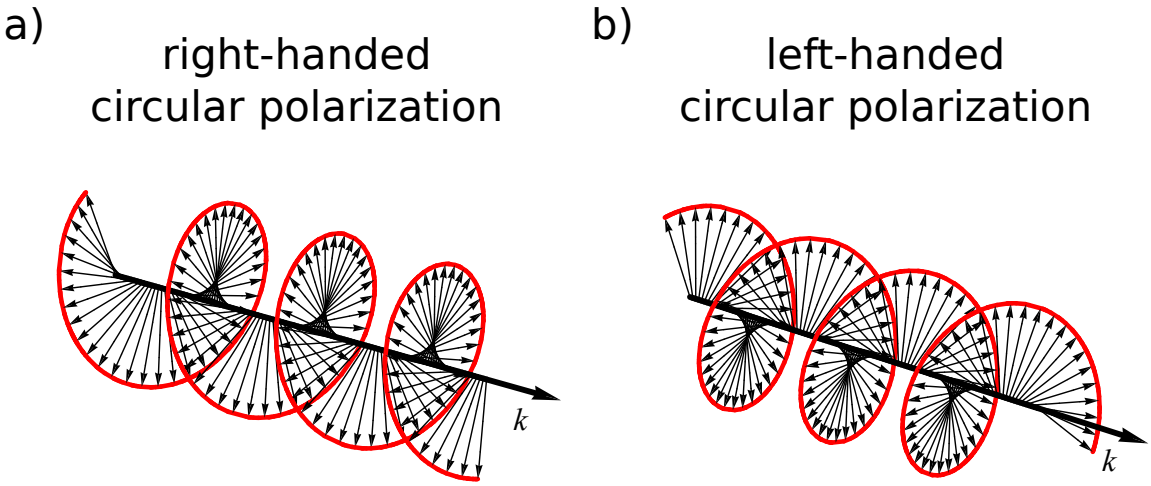

Figure 2.1. – Definition of right-handed and left-handed circular polarization. (a) A plane electromagnetic wave has a right-handed circular polarization if its electric field performs (in time) a clockwise circular motion as one looks in the direction of the wave's momentum. (b) Otherwise, if the rotation is counter-clockwise the wave possesses a left-handed circular polarization.

SAM operator. Each component of this spin operator must be a 3×3-matrix, since the description of light within the Fourier space is done in terms of the vector potential $\widetilde{\mathbf{A}}(\mathbf{p},\omega)$. The explicit form of these matrices is given, for example, in Ref. [99] and reads

$$\widehat{S}_x = \begin{pmatrix} 0 & 0 & 0 \\ 0 & 0 & -\mathrm{i} \\ 0 & \mathrm{i} & 0 \end{pmatrix}, \quad \widehat{S}_y = \begin{pmatrix} 0 & 0 & \mathrm{i} \\ 0 & 0 & 0 \\ -\mathrm{i} & 0 & 0 \end{pmatrix}, \quad \widehat{S}_z = \begin{pmatrix} 0 & -\mathrm{i} & 0 \\ \mathrm{i} & 0 & 0 \\ 0 & 0 & 0 \end{pmatrix}. \tag{2.28}$$

To quantify the amount of SAM along an arbitrary momentum component $\mathbf{p}$ of the vector potential $\widetilde{\mathbf{A}}(\mathbf{p},\omega)$, one constructs with the help of Eq. (2.28) the helicity operator

$$\widehat{\Lambda} = \left(\mathbf{p}\cdot\widehat{\mathbf{S}}\right)/\left|\mathbf{p}\right| \tag{2.29}$$

in the momentum space. The helicity operator (2.29) serves to characterize the helicity states by the following eigenvalue problem:

$$\widehat{\Lambda}\,\mathbf{e}_{\mathbf{p}\lambda} = \lambda\,\mathbf{e}_{\mathbf{p}\lambda}. \tag{2.30}$$

By using spherical coordinates

$$p = \sqrt{p_x^2 + p_y^2 + p_z^2}, \quad \varphi_p = \arctan(p_y/p_x), \quad \theta_p = \arccos(p_z/p), \tag{2.31}$$

solutions of the eigenvalue problem (2.30) can be written as (see Appendix A)

$$\mathbf{e}_{\mathbf{p}\lambda} = \frac{-\lambda}{\sqrt{2}} \begin{pmatrix} \cos\theta_p \cos\varphi_p - \mathrm{i}\lambda \sin\varphi_p \\ \cos\theta_p \sin\varphi_p + \mathrm{i}\lambda \cos\varphi_p \\ -\sin\theta_p \end{pmatrix}. \tag{2.32}$$

This vector, also called *helicity vector*, fulfills the transversality condition (2.26),

$$\mathbf{p} \cdot \mathbf{e}_{\mathbf{p}\lambda} = 0, \tag{2.33}$$

and is normalized as

$$\mathbf{e}^*_{\mathbf{p}\lambda} \cdot \mathbf{e}_{\mathbf{p}\lambda'} = \delta_{\lambda\lambda'}, \tag{2.34}$$

where $\delta_{\lambda\lambda'}$ is a Kronecker delta [71]. Now that we have introduced both, the momentum and helicity eigenfunctions, we can proceed to construct the vector potential of circularly polarized plane waves.

2.2.3. Final Form of Vector Potential

Combining Eqs. (2.24), (2.27), and (2.32), we may write

$$\widetilde{\mathbf{A}}^{\mathrm{pl}}_{\mathbf{k}\lambda}(\mathbf{p}, \omega) = (2\pi)^{3/2}\, \alpha\, \delta(p - \alpha\,\omega)\, \delta^3(\mathbf{p} - \mathbf{k})\, \mathbf{e}_{\mathbf{p}\lambda} \tag{2.35}$$

for the vector potential of a plane electromagnetic wave with well-defined linear momentum $\mathbf{k}$ and helicity λ. Here $(2\pi)^{3/2}\,\alpha$ is an appropriate normalization constant. It is straightforward to obtain the associated vector potential $\mathbf{A}^{\mathrm{pl}}_{\mathbf{k}\lambda}(\mathbf{r}, t)$ in position-time coordinates by using the transformation formula (2.16):

$$\mathbf{A}^{\mathrm{pl}}_{\mathbf{k}\lambda}(\mathbf{r}, t) = \mathbf{e}_{\mathbf{k}\lambda}\, \mathrm{e}^{\mathrm{i}(\mathbf{k}\cdot\mathbf{r} - \omega(k)\, t)}, \tag{2.36}$$

where $\omega(k)$ is given by Eq. (2.19). From Eq. (2.36) one can derive that the vector potential $\mathbf{A}^{\mathrm{pl}}_{\mathbf{k}\lambda}(\mathbf{r}, t)$ is normalized as

$$\int \mathbf{A}^{\mathrm{pl},*}_{\mathbf{k}\lambda}(\mathbf{r}, t) \cdot \mathbf{A}^{\mathrm{pl}}_{\mathbf{k}'\lambda'}(\mathbf{r}, t)\, \mathrm{d}^3\mathbf{r} = (2\pi)^3\, \delta(\mathbf{k} - \mathbf{k}')\, \delta_{\lambda\lambda'}. \tag{2.37}$$

We note that it is often convenient to distinguish between the spatial- and the time-dependent part of the vector potential (2.36) so that we may write

$$\mathbf{A}^{\mathrm{pl}}_{\mathbf{k}\lambda}(\mathbf{r},t) = \mathbf{A}^{\mathrm{pl}}_{\mathbf{k}\lambda}(\mathbf{r})\,\mathrm{e}^{-\mathrm{i}\,\omega(k)\,t}, \quad \mathbf{A}^{\mathrm{pl}}_{\mathbf{k}\lambda}(\mathbf{r}) = \mathbf{e}_{\mathbf{k}\lambda}\,\mathrm{e}^{\mathrm{i}\,\mathbf{k}\cdot\mathbf{r}}. \tag{2.38}$$

Eq. (2.38) provides the final form of the vector potential in position-time coordinates for plane electromagnetic waves with a particular linear momentum $\mathbf{k}$ and a definite helicity λ.

For completeness, we will also calculate the (complex) electric and magnetic field of a circularly polarized plane wave. By using Eqs. (2.8)–(2.9), we obtain for the plane electromagnetic waves (2.38) the well-known expressions [96]:

$$\mathbf{E}^{\mathrm{pl}}_{\mathbf{k}\lambda}(\mathbf{r},t) = -\frac{\partial}{\partial t}\,\mathbf{A}^{\mathrm{pl}}_{\mathbf{k}\lambda}(\mathbf{r},t) = \mathrm{i}\,\omega(k)\,\mathbf{A}^{\mathrm{pl}}_{\mathbf{k}\lambda}(\mathbf{r},t), \tag{2.39}$$

$$\mathbf{B}^{\mathrm{pl}}_{\mathbf{k}\lambda}(\mathbf{r},t) = \nabla\times\mathbf{A}^{\mathrm{pl}}_{\mathbf{k}\lambda}(\mathbf{r},t) = \big(1/\omega(k)\big)\,\big(\mathbf{k}\times\mathbf{E}^{\mathrm{pl}}_{\mathbf{k}\lambda}(\mathbf{r},t)\big). \tag{2.40}$$

As follows from Eqs. (2.39)–(2.40), the electric and magnetic fields $\mathbf{E}^{\mathrm{pl}}_{\mathbf{k}\lambda}(\mathbf{r},t)$ and $\mathbf{B}^{\mathrm{pl}}_{\mathbf{k}\lambda}(\mathbf{r},t)$ of a plane wave as well as the wave vector $\mathbf{k}$ are perpendicular to each other. This concludes our brief discussion on the (circularly polarized) plane waves and in the next section we will come now to the description of the *twisted* light states.

2.3. Twisted Electromagnetic Waves: Construction of Vector Potential

In the previous section, we discussed circularly polarized plane waves which carry a well-defined SAM along their propagation direction. Likewise, one may ask if it is also possible that light waves possess a definite value of OAM along their direction of propagation. Behind this question lies a complex theory with a long history and there are many studies that elaborate on this point [100–104]. For a recent and extensive overview on this topic see [105]. Here we would like, however, not to delve too deep into the underlying theory and rather *motivate* a short and simple answer to the above question on a level that is sufficient for the discussion of the twisted photon states.

To construct in a gauge invariant way a light state that carries a well-defined OAM along the propagation direction is *impossible* (or only approximately possible). This impossibility originates from an OAM-SAM coupling inherent to every light wave due to the gauge condition (2.12). To see this, we turn to the description of a light field in terms of its vector potential $\mathbf{A}(\mathbf{r},t)$ and consider the OAM operator in position space [71, 106]

$$\widehat{\mathbf{L}} = (\mathbf{r} \times \widehat{\mathbf{p}}) = -\mathrm{i}\ (\mathbf{r} \times \nabla)\,. \tag{2.41}$$

If we act with this operator on the vector potential $\mathbf{A}(\mathbf{r}, t)$, it will probe the spatial behaviour of the potential by the derivative $\nabla = \partial/\partial\,\mathbf{r}$. The spatial dependency of $\mathbf{A}(\mathbf{r}, t)$, however, is restricted by the gauge (transversality) condition (2.12). More specifically, this condition interrelates the vectorial character of $\mathbf{A}(\mathbf{r}, t)$ to its spatial behaviour, i.e. it connects the OAM of the light wave to the vector structure of the potential $\mathbf{A}(\mathbf{r}, t)$.

We recall now that the SAM operator (2.28) acts solely on the vectorial part of the potential $\mathbf{A}(\mathbf{r}, t)$; that is, the SAM of a light field is determined by the vectorial structure of its vector potential. Overall, both the SAM and OAM of a light wave are connected to the vectorial part of the potential $\mathbf{A}(\mathbf{r}, t)$ and therefore they mutually affect each other. In other words, the gauge condition (2.12) effectively imposes a coupling between the SAM and the OAM of a light wave.

Every vector field (including the potential $\mathbf{A}(\mathbf{r}, t)$) possesses a non-zero SAM:

$$\widehat{\mathbf{S}}^2\mathbf{A}(\mathbf{r}, t) = \left[\begin{pmatrix} 0 & 0 & 0 \\ 0 & 1 & 0 \\ 0 & 0 & 1 \end{pmatrix} + \begin{pmatrix} 1 & 0 & 0 \\ 0 & 0 & 0 \\ 0 & 0 & 1 \end{pmatrix} + \begin{pmatrix} 1 & 0 & 0 \\ 0 & 1 & 0 \\ 0 & 0 & 0 \end{pmatrix}\right] \mathbf{A}(\mathbf{r}, t) = 2\,\mathbf{A}(\mathbf{r}, t). \tag{2.42}$$

Since the SAM of a light field is non-zero, it will always affect an emerging OAM of the light due to the inherent SAM-OAM coupling. Thus the coupling between the spin and orbital angular momenta due to the gauge condition (2.12) is the reason that one can in principal not construct light fields with a well-defined OAM along the propagation direction.

2.3.1. Definition of Twisted Light States

Having the preceding discussion in mind, the question arises what we understand under a twisted light wave if it is not a state with a particular OAM along the propagation direction. In order to motivate the definition of such a state, let us point out that our reasoning from above has imposed no restrictions on the *total angular momentum* (TAM) of a light wave. And indeed, as will be seen later, it is possible to construct electromagnetic waves that carry a well-defined TAM along their propagation direction. From now on, let us refer to such electromagnetic waves as *twisted light*.

Our definition of a twisted light state needs some further explanations. It may seem that there exists a contradiction between the characterization of twisted light as done here and as performed in the introductory chapter. As a reminder, in the

introduction we have stated that it is possible to produce light waves with a well-defined OAM along their propagation direction. How is such a statement compatible with our reasoning here? The twisted light states can be constructed in such a way that for certain values of their linear momentum components the OAM and SAM approximately decouple. In this so-called *paraxial* regime, one can therefore unambiguously speak of the OAM and SAM along the propagation direction of the twisted light beam. Nearly all studies so far have been performed to investigate the fundamental properties and basic applications of twisted light beams within this paraxial regime. That is the reason why we have only talked about the OAM and not the TAM of a light beam in the introduction. In this work, we will go beyond the paraxial approximation and, therefore, we consider the "complete" description of a twisted light beam that is based on the TAM. This full and *non-paraxial* form of a twisted light state allows, moreover, to easily recover the paraxial electromagnetic waves as will be seen later.

2.3.2. Interplay between Linear Momentum and TAM of Twisted Light Waves

As has been hinted at within the previous paragraph, the linear momentum of a twisted light beam determines if the OAM and SAM along the beam's propagation direction can be unambiguously separated (paraxial regime) or couple to a TAM (non-paraxial regime). Let us now comment more thoroughly on the interplay between the linear momentum and the TAM of a twisted light wave. To do so, we will adopt the propagation direction of the twisted light wave as the (quantization) z-axis.

Imagine a twisted electromagnetic wave that carries a well-defined TAM along the z-axis, which we will also denote as the *longitudinal* TAM. The projection of the TAM along the z-axis is characterized by the following operator

$$\widehat{J}_z = \widehat{L}_z + \widehat{S}_z, \tag{2.43}$$

where the corresponding projections of the OAM and SAM operators in the position space read

$$\widehat{L}_z = -\mathrm{i}\left(x\,\frac{\partial}{\partial y} - y\,\frac{\partial}{\partial x}\right), \quad \widehat{S}_z = \begin{pmatrix} 0 & -\mathrm{i} & 0 \\ \mathrm{i} & 0 & 0 \\ 0 & 0 & 0 \end{pmatrix}. \tag{2.44}$$

The operator $\widehat{J}_z$ does not commute with the components $\widehat{p}_x = -\mathrm{i}\,\partial/\partial x$ and $\widehat{p}_y = -\mathrm{i}\,\partial/\partial y$ of the linear momentum operator:

$$\left[\widehat{J}_z, \widehat{p}_x\right] = \left[\widehat{L}_z, \widehat{p}_x\right] = \mathrm{i}\,\widehat{p}_y, \tag{2.45}$$

$$\left[\widehat{J}_z, \widehat{p}_y\right] = \left[\widehat{L}_z, \widehat{p}_y\right] = -\mathrm{i}\,\widehat{p}_x, \tag{2.46}$$

where the commutator of two operators is defined as

$$\left[\widehat{A}, \widehat{B}\right] = \widehat{A}\,\widehat{B} - \widehat{B}\,\widehat{A}. \tag{2.47}$$

Operators that do not commute cannot have simultaneous eigenfunctions. It thus follows from Eqs. (2.45)–(2.46) that a twisted light state with a definite TAM along the z-axis cannot have a well-defined linear momentum along the x- or y-axes. This behaviour is completely different from the plane electromagnetic waves (2.38), for which all components of the linear momentum vector possess a precise value. We notice here, moreover, that the linear momentum of a twisted light wave in z-direction, also called the longitudinal linear momentum, poses no such problem, since

$$\left[\widehat{J}_z, \widehat{p}_z\right] = 0, \quad \widehat{p}_z = -\mathrm{i}\,\partial/\partial z. \tag{2.48}$$

Although the individual operators $\widehat{p}_x$ and $\widehat{p}_y$ do not commute with $\widehat{J}_z$ as seen from Eqs (2.45)–(2.46), it is still possible to construct from them an operator that does. The squared absolute value of the linear momentum transverse to the propagation direction of the twisted light beam is defined by

$$\widehat{p}_\perp^2 = \widehat{p}_x^2 + \widehat{p}_y^2. \tag{2.49}$$

If we calculate the commutator of $\widehat{p}_\perp^2$ with $\widehat{J}_z$, we obtain

$$\left[\widehat{J}_z, \widehat{p}_\perp^2\right] = \left[\widehat{L}_z, \widehat{p}_\perp^2\right] = \left[\widehat{L}_z, \widehat{p}_x^2\right] + \left[\widehat{L}_z, \widehat{p}_y^2\right] = 2\mathrm{i}\,\widehat{p}_x\,\widehat{p}_y - 2\mathrm{i}\,\widehat{p}_x\,\widehat{p}_y = 0. \tag{2.50}$$

Since $\widehat{p}_\perp^2$ commutes with $\widehat{J}_z$, a twisted light wave can possess a well-defined absolute value of the linear momentum transverse to the propagation direction. From now on, let us refer to this quantity as the *transverse linear momentum*. Altogether, we conclude that a twisted electromagnetic wave can have simultaneously a well-defined longitudinal TAM and longitudinal linear momentum as well as a transverse linear momentum.

Above we have seen that twisted electromagnetic waves may carry a well-defined linear momentum along and transverse to the propagation direction. Such a special

type of a twisted light state is also referred to within the literature as a *Bessel* electromagnetic wave [107]. In the next section, we will construct the vector potential for such Bessel light waves. The resulting form of the vector potential will show us that the term "Bessel" for these waves is well-justified.

2.3.3. Vector Potential of Twisted Bessel Waves

The characterization of a twisted Bessel light wave is done in a similar way as for the plane electromagnetic waves. For the plane waves, we have chosen an appropriate set of operators and required that the vector potential should be a simultaneous eigenstate to these operators. Let us discuss now how such a set should look like for the Bessel electromagnetic waves. We note that some parts of this discussion closely follow the corresponding sections in our published paper [68].

Transverse and Longitudinal Momentum of Bessel Waves

In Sec. 2.3 we found that twisted light waves can possess a well-defined transverse as well as longitudinal linear momentum, which we will denote here as $\varkappa$ and k_z, respectively. As mentioned, such special kinds of twisted light states are named Bessel waves. To construct the vector potential of these Bessel states, we return to the Fourier space by using Eqs. (2.15)–(2.16). Then we can write the well-definedness of the transverse and longitudinal linear momenta as the following eigenvalue problem:

$$\widehat{p}_z \, \widetilde{\mathbf{A}}(\mathbf{p},\omega) = k_z \, \widetilde{\mathbf{A}}(\mathbf{p},\omega), \tag{2.51}$$

$$\widehat{p}_\perp^{\,2} \, \widetilde{\mathbf{A}}(\mathbf{p},\omega) = \left(\widehat{p}_x^{\,2} + \widehat{p}_y^{\,2}\right) \, \widetilde{\mathbf{A}}(\mathbf{p},\omega) = \varkappa^2 \, \widetilde{\mathbf{A}}(\mathbf{p},\omega). \tag{2.52}$$

By employing that the momentum operators act as simple multiplications in Fourier space ($\widehat{p}_z = p_z$, $\widehat{p}_\perp^{\,2} = p_\perp^2 = p_x^2 + p_y^2$), we deduce that solutions of Eqs. (2.51)–(2.52) must be of the form

$$\widetilde{\mathbf{A}}(\mathbf{p},\omega) \propto \delta(p_z - k_z)\, \delta(p_\perp - \varkappa). \tag{2.53}$$

Here the delta distribution $\delta(p_z - k_z)$ ensures that Eq. (2.51) holds true, whereas the delta distribution $\delta(p_\perp - \varkappa)$ provides for condition (2.52).

Eq. (2.53) characterizes light waves with a well-defined transverse momentum $\varkappa$ and longitudinal momentum k_z. As can be deduced from the delta distributions in this equation, all momenta that contribute to the vector potential of the Bessel wave must lie on a "momentum" cone as depicted in Fig. 2.2. The height of this cone is given by the longitudinal momentum k_z, whereas the radius of its circular base area

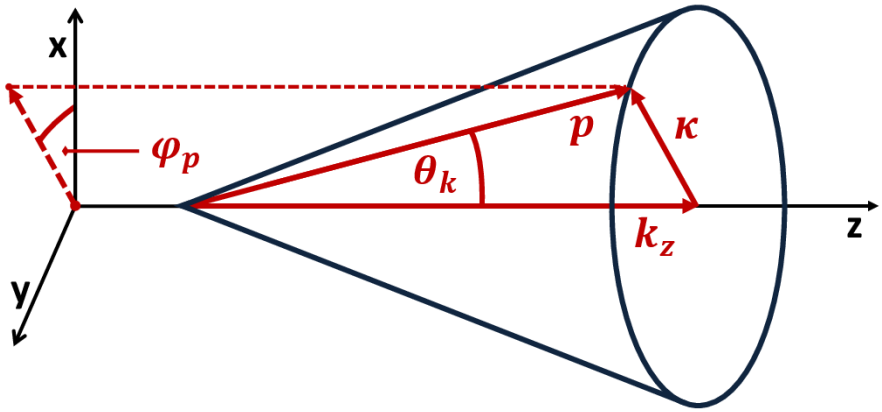

Figure 2.2. – Momentum distribution of a Bessel light wave. The longitudinal (along the z-axis) and transverse (perpendicular to the z-axis) momenta of a Bessel wave are fixed and denoted here by k_z and $\varkappa$, respectively. Thus the momentum vectors constituting the Bessel wave lie on a "momentum" cone with a radius $\varkappa$ of the circular base area and a height k_z. The opening angle of this cone is given by the polar angle $\theta_k = \arctan(\varkappa/k_z)$. The angle φ_p in this figure depicts, moreover, the azimuthal angle of one of the (infinitely many) momentum components of the cone.

is characterized by the transverse momentum $\varkappa$. Moreover, the opening angle of this cone can be written as

$$\theta_k = \arctan(\varkappa/k_z). \tag{2.54}$$

In the following, we will often use the opening angle of the momentum cone as a parameter to characterize the Bessel light waves.

Orbital and Spin Structure of Bessel Waves

Up to now, we have discussed the dependency of the vector potential of a Bessel beam on its linear momentum components. Since Bessel beams are a special type of twisted light waves, they do not only carry linear momentum but also a particular TAM along the propagation (z-)direction. As has been mentioned in Sec. 2.3, this well-defined projection of the TAM arises from a coupling of the longitudinal components of the OAM and SAM. Let us therefore first investigate how states with either a particular orbital or spin angular momentum along the z-axis look like.

Orbital structure—The z-component of the OAM operator has the following form in the frequency-momentum space

$$\widehat{L}_z = -\mathrm{i}\,\frac{\partial}{\partial\varphi_p}, \tag{2.55}$$

where φ_p is the azimuthal angle of the momentum vector $\mathbf{p}$ as defined by Eq. (2.31). It is easy to prove that the functions

$$\Phi_{m_l}(\mathbf{p}) \equiv \Phi_{m_l}(\varphi_p) = \mathrm{e}^{\mathrm{i}\, m_l\, \varphi_p}. \tag{2.56}$$

are eigenfunctions to the operator (2.55) with eigenvalue m_l:

$$\widehat{L}_z\, \Phi_{m_l}(\varphi_p) = m_l\, \Phi_{m_l}(\varphi_p). \tag{2.57}$$

Here the eigenvalue m_l represents the OAM along the z-axis that the functions (2.56) possess. The eigenvalues are only restricted by the requirement that the functions (2.56) are single-valued, i.e. the $\Phi_{m_l}(\varphi_p)$ have to take the same value at $\varphi_p = 0$ and $\varphi_p = 2\pi$. It follows therefore that only integer values $m_l = 0, +1, -1, +2, -2, \ldots$ are allowed. Moreover, the functions $\Phi_{m_l}(\varphi_p)$ are normalized such that

$$\int_0^{2\pi} \Phi^*_{m_l}(\varphi_p)\, \Phi_{m_l'}(\varphi_p)\, \mathrm{d}\varphi_p = 2\pi\, \delta_{m_l m_l'}. \tag{2.58}$$

This concludes our discussion on the OAM-eigenfunctions.

Spin structure—Let us come now to the description of states with a well-defined SAM along the z-axis. The eigenvalue problem for the z-component of the SAM operator $\widehat{S}_z$ reads

$$\widehat{S}_z\, \boldsymbol{\eta}_{m_s} \;=\; m_s\, \boldsymbol{\eta}_{m_s}. \tag{2.59}$$

We note that the operator $\widehat{S}_z$ has the same form in position-time and momentum-frequency space and is thus given by Eq. (2.44). Solving the eigenvalue problem (2.59) leads to the three solutions

$$\boldsymbol{\eta}_{\pm 1} = \frac{\mp 1}{\sqrt{2}} \begin{pmatrix} 1 \\ \pm\mathrm{i} \\ 0 \end{pmatrix}, \quad \boldsymbol{\eta}_0 = \begin{pmatrix} 0 \\ 0 \\ 1 \end{pmatrix}, \tag{2.60}$$

which have been normalized as

$$\boldsymbol{\eta}^*_{m_s} \cdot \boldsymbol{\eta}_{m_s'} = \delta_{m_s m_s'}. \tag{2.61}$$

The vectors $\boldsymbol{\eta}_{m_s}$ describe states with a SAM along the z-axis of either $m_s = 0, \pm 1$. For a plane electromagnetic wave, we have found that the SAM along the propagation

direction can only have the values ± 1 because of the transversality condition (2.26). Plane waves possess, however, a well-defined linear momentum, i.e. all components of the linear momentum vector take a particular value. In contrast to plane light states, a Bessel wave is composed of momentum vectors $\mathbf{p}$ that are oriented on a cone around the propagation direction. In this case, the transversality condition does not forbid the occurrence of the $m_s = 0$ component. Therefore all three vectors $\boldsymbol{\eta}_{m_s}$, $m_s = 0, \pm 1$, might be used to construct the Bessel waves.

Coupling of OAM and SAM to a Longitudinal TAM

It is now our task to couple the spin and the orbital angular momentum states (2.56) and (2.60) together in order to construct a function that possesses a well-defined value of TAM along the z-direction. Let us denote this value by m_γ.

There are only certain combinations of the orbital and spin eigenfunctions that result in a longitudinal TAM of m_γ. The angular momentum along some axis is an additive quantum number, and thus the condition

$$m_\gamma = m_l + m_s \tag{2.62}$$

has to be satisfied. As was introduced earlier, here the quantities m_l and m_s denote the OAM and SAM along the z-axis, respectively. The z-component of the SAM operator can only have the eigenvalues $m_s = -1, 0, +1$, whereas the longitudinal OAM can take any integer value. Therefore Eq. (2.62) is only fulfilled for the following three pairs of m_s and m_l eigenvalues:

$$\begin{aligned} &m_l = m_\gamma - 1 \ \text{ and } \ m_s = +1, \\ &m_l = m_\gamma \ \text{ and } \ m_s = 0, \\ &m_l = m_\gamma + 1 \ \text{ and } \ m_s = -1. \end{aligned} \tag{2.63}$$

Such a requirement is also illustrated graphically in Fig. 2.3.

The most general state that fulfills condition (2.62) is a superposition of OAM and SAM states with eigenvalues as given by Eq. (2.63):

$$\mathbf{U}_{m_\gamma}(\mathbf{p}) = \sum_{m_s = 0, \pm 1} c_{m_s}(p_\perp, p_z)\, \Phi_{m_\gamma - m_s}(\varphi_p)\, \boldsymbol{\eta}_{m_s}. \tag{2.64}$$

Here the φ_p-dependency is completely incorporated into the orbital function $\Phi_{m_\gamma - m_s}$. The superposition coefficients $c_{m_s}(p_\perp, p_z)$, in contrast, depend solely on the transverse ($p_\perp$) and longitudinal (p_z) momenta to ensure that the OAM structure of the state (2.64) as required by Eq. (2.63) is not destroyed. To prove that the state (2.64)

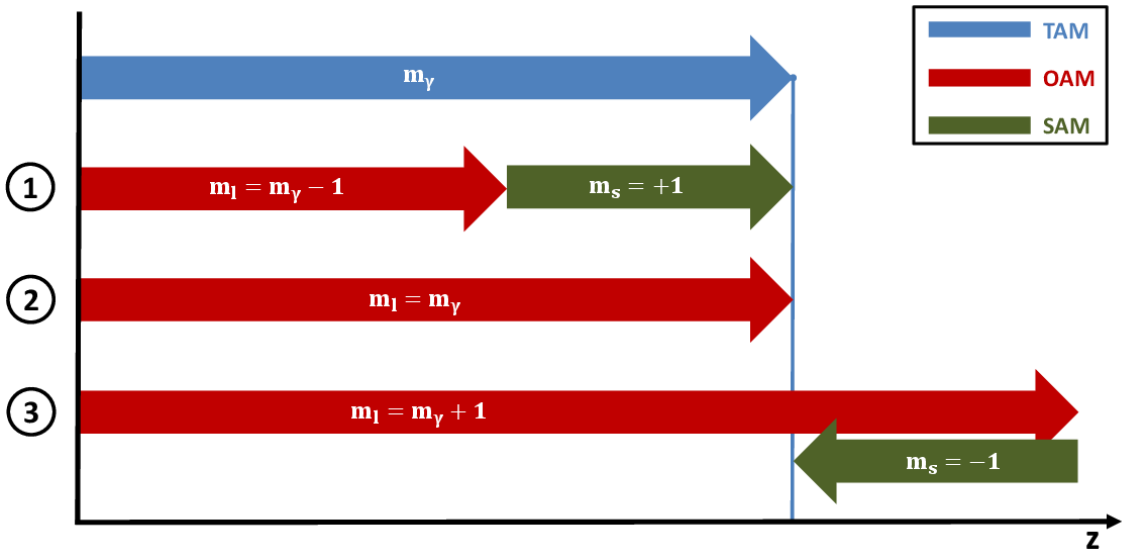

Figure 2.3. – Coupling of SAM and OAM components to result in a TAM m_γ along the z-axis. Three pairs of orbital and spin angular momentum states contribute to the coupling. These pairs have the following quantum numbers: (1) $m_l = m_\gamma - 1$ and $m_s = +1$, (2) $m_l = m_\gamma$ and $m_s = 0$, (3) $m_l = m_\gamma + 1$ and $m_s = -1$.

has a well-defined projection of TAM along the z-axis, we act upon it with the operator $\widehat{J}_z$ and obtain

$$\begin{aligned}\widehat{J}_z\,\mathbf{U}_{m_\gamma}(\mathbf{p}) &= \sum_{m_s=0,\,\pm1} c_{m_s}(p_\perp, p_z)\left[\left(\widehat{L}_z\,\Phi_{m_\gamma-m_s}(\varphi_p)\right)\boldsymbol{\eta}_{m_s} + \Phi_{m_\gamma-m_s}(\varphi_p)\left(\widehat{S}_z\,\boldsymbol{\eta}_{m_s}\right)\right] \\ &= \sum_{m_s=0,\,\pm1} (m_\gamma - m_s + m_s)\,c_{m_s}(p_\perp, p_z)\,\Phi_{m_\gamma-m_s}(\varphi_p)\,\boldsymbol{\eta}_{m_s} \\ &= m_\gamma\,\mathbf{U}_{m_\gamma}(\mathbf{p}).\end{aligned} \tag{2.65}$$

In conclusion, Eq. (2.65) shows that the state (2.64) possesses a value m_γ of the longitudinal TAM.

Form of the Superposition Coefficients

Above, we constructed a vector function with a particular value of TAM along the z-direction. Such a function was written as a superposition of states with well-defined longitudinal OAM and SAM (see Eq. (2.64)). Up to now, however, the superposition coefficients are undefined and allow still for some freedom. To fix them, we can

impose a further condition onto the functions (2.64). In particular, we may require that the superposition coefficients are chosen in such a way that the resulting vector function $\mathbf{U}_{m_\gamma}(\mathbf{p})$ possesses a precise helicity

$$\widehat{\Lambda}\,\mathbf{U}_{m_\gamma}(\mathbf{p}) = \lambda\,\mathbf{U}_{m_\gamma}(\mathbf{p}), \tag{2.66}$$

i.e. the SAM along each momentum component $\mathbf{p}$ is well-defined; the helicity operator $\widehat{\Lambda}$ is given by Eq. (2.29). We note, however, that the SAM along the individual momentum components $\mathbf{p}$ does not determine the SAM along the propagation direction of the wave and one has, therefore, to distinguish carefully between the helicity operator, i.e. the SAM along the momentum components, and the z-component of the SAM operator.

Solving Eq. (2.66) with expression (2.64) as an ansatz leads to the following coefficients $c_{m_s}(p_\perp, p_z) \equiv c_{m_s}(\lambda,\, \theta_p)$:

$$c_{\pm 1}(\lambda,\, \theta_p) = \frac{1}{2}\,(1 \pm \lambda\,\cos\theta_p)\,,\; c_0(\lambda,\, \theta_p) = \frac{\lambda}{\sqrt{2}}\sin\theta_p. \tag{2.67}$$

By using now the explicit form (2.56) of the orbital functions $\Phi_{m_l}(\mathbf{p})$, one obtains

$$\mathbf{U}_{m_\gamma}(\mathbf{p}) \equiv \mathbf{U}_{m_\gamma\lambda}(\mathbf{p}) = \mathrm{e}^{\mathrm{i}\,m_\gamma\,\varphi_p} \sum_{m_s=0,\,\pm 1} c_{m_s}(\lambda, \theta_p)\,\mathrm{e}^{-\mathrm{i}\,m_s\,\varphi_p}\,\boldsymbol{\eta}_{m_s}. \tag{2.68}$$

Moreover, by employing the helicity vector (2.32), the function (2.68) may be written in a very simple form. To do so, we note that the helicity vector (2.32) can be expanded in terms of the spin eigenstates (2.60) as

$$\mathbf{e}_{\mathbf{p}\lambda} = \sum_{m_s=0,\,\pm 1} c_{m_s}(\lambda, \theta_p)\,\mathrm{e}^{-\mathrm{i}\,m_s\,\varphi_p}\,\boldsymbol{\eta}_{m_s}. \tag{2.69}$$

If we compare this expression with Eq. (2.69), we find that $\mathbf{U}_{m_\gamma\lambda}(\mathbf{p})$ simply reads

$$\mathbf{U}_{m_\gamma\lambda}(\mathbf{p}) = \mathrm{e}^{\mathrm{i}\,m_\gamma\,\varphi_p}\,\mathbf{e}_{\mathbf{p}\lambda}. \tag{2.70}$$

As follows from our construction, Eq. (2.70) describes a vector function that possesses a well-defined TAM of m_γ along the z-axis as well as a particular helicity λ. It is also apparent from Eq. (2.70) that $\mathbf{U}_{m_\gamma\lambda}(\mathbf{p})$ complies with the transversality condition (2.26), since $\mathbf{p}\cdot\mathbf{e}_{\mathbf{p}\lambda} = 0$, and can therefore be used for the description of a light state. In the following, we will—depending on convenience—either use the "helicity form" (2.70) of this function or the expansion (2.68) in eigenstates of the longitudinal SAM operator.

Vector Potential of Bessel Waves: Final Form

Above, we have constructed vector functions $\mathbf{U}_{m_\gamma\lambda}(\mathbf{p})$ that possess a well-defined TAM m_γ along the z-direction as well as a helicity λ. If we combine this function with Eqs. (2.24) and (2.53), we may finally express the vector potential of a Bessel wave within the Fourier space as

$$\widetilde{\mathbf{A}}^{\mathrm{tw}}_{\varkappa m_\gamma k_z\lambda}(\mathbf{p},\omega) = \alpha\,\varkappa^{-1/2}\,(-\mathrm{i})^{m_\gamma}\,\mathrm{e}^{\mathrm{i}m_\gamma\varphi_p}\,\delta(p-\alpha\,\omega)\,\delta(p_z-k_z)\,\delta(p_\perp-\varkappa)\,\mathbf{e}_{\mathbf{p}\lambda}. \quad (2.71)$$

Here we introduced the factor $\alpha\,\varkappa^{-1/2}\,(-\mathrm{i})^{m_\gamma}$ as a normalization constant. It follows from our construction that the Bessel waves described by the potential (2.71) carry a transverse and longitudinal linear momentum $\varkappa$ and k_z, a helicity λ as well as a longitudinal TAM m_γ.

By applying the transformation formula (2.16) to Eq. (2.71), we may express the vector potential of a Bessel wave in real space as

$$\begin{aligned}\mathbf{A}^{\mathrm{tw}}_{\varkappa m_\gamma k_z\lambda}(\mathbf{r},t) &= \alpha\,\varkappa^{-1/2}\,(-\mathrm{i})^{m_\gamma}\,(2\pi)^{-3/2}\\ &\quad\times\int\delta(p-\alpha\,\omega)\,\delta(p_z-k_z)\,\delta(p_\perp-\varkappa)\,\mathrm{e}^{\mathrm{i}m_\gamma\varphi_p}\,\mathbf{e}_{\mathbf{p}\lambda}\,\mathrm{e}^{\mathrm{i}(\mathbf{r}\cdot\mathbf{p}-\omega\,t)}\,\mathrm{d}\omega\,\mathrm{d}^3\mathbf{p}.\end{aligned} \quad (2.72)$$

The integral over ω in Eq. (2.72) can be immediately evaluated due to the delta distribution $\delta(p-\alpha\,\omega)$ as

$$\begin{aligned}\mathbf{A}^{\mathrm{tw}}_{\varkappa m_\gamma k_z\lambda}(\mathbf{r},t) &= \varkappa^{-1/2}\,(-\mathrm{i})^{m_\gamma}\,(2\pi)^{-3/2}\\ &\quad\times\int\delta(p_z-k_z)\,\delta(p_\perp-\varkappa)\,\mathrm{e}^{\mathrm{i}m_\gamma\varphi_p}\,\mathbf{e}_{\mathbf{p}\lambda}\,\mathrm{e}^{\mathrm{i}(\mathbf{r}\cdot\mathbf{p}-\omega(p)\,t)}\,\mathrm{d}^3\mathbf{p},\end{aligned} \quad (2.73)$$

where $\omega(p)$ is given by Eq. (2.19). If one compares Eq. (2.73) with the vector potential $\mathbf{A}^{\mathrm{pl}}_{\mathbf{p}\lambda}(\mathbf{r},t)$ of a plane electromagnetic wave as given by Eq. (2.36), one sees that $\mathbf{A}^{\mathrm{tw}}_{\varkappa m_\gamma k_z\lambda}(\mathbf{r},t)$ can be re-written as [26, 27, 68]

$$\mathbf{A}^{\mathrm{tw}}_{\varkappa m_\gamma k_z\lambda}(\mathbf{r},t) = \int a_{\varkappa m_\gamma k_z}(\mathbf{p})\,\mathbf{A}^{\mathrm{pl}}_{\mathbf{p}\lambda}(\mathbf{r},t)\,\mathrm{d}^3\mathbf{p}, \quad (2.74)$$

$$a_{\varkappa m_\gamma k_z}(\mathbf{p}) = \varkappa^{-1/2}\,(-\mathrm{i})^{m_\gamma}\,(2\pi)^{-3/2}\,\mathrm{e}^{\mathrm{i}m_\gamma\varphi_p}\,\delta(p_z-k_z)\,\delta(p_\perp-\varkappa). \quad (2.75)$$

Eqs. (2.74)–(2.75) provide a very intuitive view on the electromagnetic Bessel waves. More specifically, these equations illustrate that the Bessel waves can be interpreted

as a *coherent superposition of circularly polarized plane waves*. Each of these plane waves possesses a *azimuthal phase* as given by the factor $\mathrm{e}^{\mathrm{i}m_\gamma\varphi_p}$ in Eq. (2.75). Moreover, the delta distributions within the function $a_{\varkappa m_\gamma k_z}(\mathbf{p})$ determine that the momentum vectors of the plane waves lie on the momentum cone depicted in Fig. 2.2. The interpretation of a Bessel wave as a superposition of plane waves will be often used in the following in order to illustrate some of the properties of Bessel beams.

We note that often we will only need the transverse structure of the function $a_{\varkappa m_\gamma k_z}(\mathbf{p})$. In this case, we will omit the delta distribution in k_z and write

$$a_{\varkappa m_\gamma}(\mathbf{p}_\perp) = \varkappa^{-1/2}\,(-\mathrm{i})^{m_\gamma}\,(2\pi)^{-3/2}\,\mathrm{e}^{\mathrm{i}m_\gamma\varphi_p}\,\delta(p_\perp-\varkappa). \tag{2.76}$$

So far, we have only re-written the Bessel waves (2.74)–(2.75) in a form that allowed a simple interpretation of these states in terms of plane waves. Now we will perform all remaining integrations in Eq. (2.74) in order to obtain the final result for the vector potential of a Bessel wave in real space. By using the expansion (2.69) of the helicity vector $\mathbf{e}_{\mathbf{p}\lambda}$ and by employing all of the delta distributions in Eqs. (2.74)–(2.75), we are left with a single φ_p-integration:

$$\begin{aligned}\mathbf{A}^{\mathrm{tw}}_{\varkappa m_\gamma k_z\lambda}(\mathbf{r},t) &= (2\pi)^{-3/2}\,\varkappa^{1/2}\,(-\mathrm{i})^{m_\gamma}\\ &\times\sum_{m_s=0,\pm1}\int_0^{2\pi} c_{m_s}(\lambda,\theta_k)\,\mathrm{e}^{\mathrm{i}(m_\gamma-m_s)\varphi_p}\,\mathrm{e}^{\mathrm{i}(\mathbf{r}\cdot\mathbf{p}-\omega(k)\,t)}\,\boldsymbol{\eta}_{m_s}\,\mathrm{d}\varphi_p,\end{aligned} \tag{2.77}$$

where the quantities

$$\mathbf{p}=(\varkappa\cos\varphi_p,\varkappa\sin\varphi_p,k_z)^T,\ k=\sqrt{\varkappa^2+k_z^2},\ \omega(k)=k/\alpha,\ \theta_k=\arctan(\varkappa/k_z) \tag{2.78}$$

have been fixed by the delta distributions in Eq. (2.75). Expression (2.77) can be evaluated even further, if one uses the integral representation

$$\int_0^{2\pi}\mathrm{e}^{\mathrm{i}l\varphi}\mathrm{e}^{\mathrm{i}x\cos(\phi-\varphi)}\mathrm{d}\varphi = 2\pi\,\mathrm{i}^l\,\mathrm{e}^{\mathrm{i}l\phi}J_l(x) \tag{2.79}$$

of the lth order Bessel function $J_l(x)$ [108]. With the help of relation (2.79) and by separating the spatial and time-dependent part, one finally obtains for the vector potential (2.77) the relation

$$\mathbf{A}^{\mathrm{tw}}_{\varkappa m_\gamma k_z\lambda}(\mathbf{r},t) = \mathbf{A}^{\mathrm{tw}}_{\varkappa m_\gamma k_z\lambda}(\mathbf{r})\,\mathrm{e}^{-\mathrm{i}\,\omega(k)\,t}, \tag{2.80}$$

where the spatial part of the vector potential can be written as a sum of three terms [68]:

$$\mathbf{A}^{\mathrm{tw}}_{\varkappa m_\gamma k_z \lambda}(\mathbf{r}) = \sum_{m_s=0,\,\pm 1} A^{\mathrm{tw}}_{\varkappa m_\gamma k_z \lambda m_s}(\mathbf{r})\, \boldsymbol{\eta}_{m_s}. \tag{2.81}$$

The scalar functions $A^{\mathrm{tw}}_{\varkappa m_\gamma k_z \lambda m_s}(\mathbf{r})$ in Eq. (2.81) are given in cylindrical coordinates $(r_\perp, \varphi_r, z)$ by

$$A^{\mathrm{tw}}_{\varkappa m_\gamma k_z \lambda m_s}(\mathbf{r}) = \sqrt{\frac{\varkappa}{2\pi}}\,(-\mathrm{i})^{m_s}\, c_{m_s}(\lambda,\, \theta_k)\, J_{m_\gamma - m_s}(\varkappa r_\perp)\, \mathrm{e}^{\mathrm{i}(m_\gamma - m_s)\,\varphi_r}\, \mathrm{e}^{\mathrm{i}\,k_z z}\,. \tag{2.82}$$

It is seen from expression (2.82) that the functions $A^{\mathrm{tw}}_{\varkappa m_\gamma k_z \lambda m_s}(\mathbf{r})$ carry a well-defined longitudinal OAM of $(m_\gamma - m_s)$ as given by the function $\mathrm{e}^{\mathrm{i}(m_\gamma - m_s)\,\varphi_r}$. Furthermore, they depend on a Bessel function $J_{m_\gamma - m_s}(\varkappa r_\perp)$ that defines their transverse shape. Therefore we finally understand why the Bessel light waves possess the name "Bessel".

Eqs. (2.81)–(2.82) describe the vector potential $\mathbf{A}^{\mathrm{tw}}_{\varkappa m_\gamma k_z \lambda}(\mathbf{r})$ of a twisted electromagnetic Bessel wave. This vector potential has been constructed in such a way that the Bessel waves carry a well-defined transverse ($\varkappa$) and longitudinal (k_z) momentum, a longitudinal TAM of m_γ and a helicity λ. In what follows now, we will deduce the main properties of a Bessel wave from the associated vector potential $\mathbf{A}^{\mathrm{tw}}_{\varkappa m_\gamma k_z \lambda}(\mathbf{r})$.

2.3.4. Separation of OAM and SAM of Bessel Light Waves: Paraxial Regime

As we have discussed above, an electromagnetic Bessel wave is a state of light that carries a specific TAM along its propagation direction, but no well-defined longitudinal OAM and SAM. There exists, however, a certain regime for the parameters of a Bessel light beam where also the longitudinal projections of the OAM and SAM are (approximately) well-defined. This happens when the transverse momentum of the Bessel wave is much smaller than the longitudinal momentum, i.e $\varkappa \ll k_z$. Such a choice of the parameters is denoted as the *paraxial regime*.

To understand this regime in a more intuitive way, we take a closer look at Fig. 2.2 that depicts the conic momentum distribution of a Bessel wave. In the paraxial regime, $\varkappa \ll k_z$, the opening angle $\theta_k = \arctan(\varkappa/k_z)$ of the momentum cone is very small. Therefore the momentum vectors composing the cone are nearly parallel to the z-axis (thus the name paraxial regime). In this regime, therefore, the Bessel wave "behaves" approximately as a single "plane wave".

We will now show that the OAM and SAM are (approximately) well-defined within the paraxial regime. To do this, let us focus on the coefficients c_{m_s} (see Eq. (2.67)) within the three terms (2.82) that contribute to the vector potential (2.81) and see how they behave if $\varkappa \ll k_z$ or equivalently $\theta_k \ll 1$:

$$c_{\pm 1}(\lambda,\, \theta_k) \overset{\varkappa \ll k_z}{\approx} \frac{1}{2}(1 \pm \lambda), \;\; c_0(\lambda,\, \theta_k) \overset{\varkappa \ll k_z}{\approx} 0\,, \tag{2.83}$$

From Eq. (2.83) it follows that in the paraxial regime only the component $c_\lambda(\lambda,\, \theta_k)$ survives and thus in this regime the vector potential can be expressed as

$$\begin{aligned} \mathbf{A}^{\mathrm{tw}}_{\varkappa m_\gamma k_z \lambda}(\mathbf{r}, t) &\overset{\varkappa \ll k_z}{\approx} A^{\mathrm{tw}}_{\varkappa m_\gamma k_z \lambda, m_s = \lambda}(\mathbf{r})\, \mathrm{e}^{-\mathrm{i}\,\omega(k)\, t}\, \boldsymbol{\eta}_\lambda \\ &= \sqrt{\frac{\varkappa}{2\pi}}\, (-\mathrm{i})^\lambda\, c_\lambda(\lambda, \theta_k)\, J_{m_\gamma - \lambda}(\varkappa\, r_\perp)\, \mathrm{e}^{\mathrm{i}(m_\gamma - \lambda)\varphi_r}\, \mathrm{e}^{\mathrm{i} k_z z}\, \mathrm{e}^{-\mathrm{i}\,\omega(k)\, t}\, \boldsymbol{\eta}_\lambda\,. \end{aligned} \tag{2.84}$$

With the help of Eq. (2.84), one can deduce that in the paraxial regime the Bessel waves have a defined OAM of $m_\gamma - \lambda$ and SAM of λ along the propagation direction:

$$\widehat{L}_z\, \mathbf{A}^{\mathrm{tw}}_{\varkappa m_\gamma k_z \lambda}(\mathbf{r}, t) \overset{\varkappa \ll k_z}{\approx} (m_\gamma - \lambda)\, \mathbf{A}^{\mathrm{tw}}_{\varkappa m_\gamma k_z \lambda}(\mathbf{r}, t), \tag{2.85}$$

$$\widehat{S}_z\, \mathbf{A}^{\mathrm{tw}}_{\varkappa m_\gamma k_z \lambda}(\mathbf{r}, t) \overset{\varkappa \ll k_z}{\approx} \lambda\, \mathbf{A}^{\mathrm{tw}}_{\varkappa m_\gamma k_z \lambda}(\mathbf{r}, t)\,. \tag{2.86}$$

Moreover, in the limit $\varkappa \to 0$, where $J_{m_\gamma - \lambda}(\varkappa\, r_\perp) \to \delta_{m_\gamma \lambda}$, Eq. (2.80) reduces to the standard solution for a plane wave that propagates along the z-axis.

2.3.5. Electric and Magnetic Field of Bessel Light Waves

For completeness, we would also like to derive the electric and the magnetic field of the Bessel electromagnetic wave. By plugging expressions (2.80)–(2.82) into Eqs. (2.8)–(2.9), we obtain (following Ref. [109]):

$$\mathbf{E}^{\mathrm{tw}}_{\varkappa m_\gamma k_z \lambda}(\mathbf{r}, t) = -\frac{\partial}{\partial t} \mathbf{A}^{\mathrm{tw}}_{\varkappa m_\gamma k_z \lambda}(\mathbf{r}, t) = \mathrm{i}\,\omega(k)\, \mathbf{A}^{\mathrm{tw}}_{\varkappa m_\gamma k_z \lambda}(\mathbf{r}, t), \tag{2.87}$$

$$\mathbf{B}^{\mathrm{tw}}_{\varkappa m_\gamma k_z \lambda}(\mathbf{r}, t) = \nabla \times \mathbf{A}^{\mathrm{tw}}_{\varkappa m_\gamma k_z \lambda}(\mathbf{r}, t) = -\mathrm{i}\lambda\, \mathbf{E}^{\mathrm{tw}}_{\varkappa m_\gamma k_z \lambda}(\mathbf{r}, t). \tag{2.88}$$

As can be seen from Eqs. (2.87)–(2.88), the electric field is up to a prefactor given by the vector potential $\mathbf{A}^{\mathrm{tw}}_{\varkappa m_\gamma k_z \lambda}(\mathbf{r}, t)$. The magnetic field is just out of phase by $\pi/2$ from the electric field [109]. In stark contrast, moreover, to the electric and magnetic fields of plane electromagnetic waves, both the electric and magnetic field possess a non-vanishing z-component.

2.3.6. Poynting Vector and Intensity Profile of Bessel Light Waves

In the previous section, we have constructed the vector potential and the electric and magnetic fields for the Bessel light waves. Let us use now use the vector potential to derive an important property of the Bessel waves: Bessel waves propagate non-diffractively, that is, their intensity profile does not change in the plane transverse to the propagation direction. In order to show this property, we use the Poynting vector of the light field. This vector describes the energy flux density of an electromagnetic field and is defined [96, cf. Eq. (6.109)] by

$$\mathbf{S} = (\mathrm{Re}\,\mathbf{E}(\mathbf{r},t)) \times (\mathrm{Re}\,\mathbf{B}(\mathbf{r},t))\,. \tag{2.89}$$

By employing Eqs. (2.87)–(2.88) and, furthermore, using (local) basis vectors of a cylindrical coordinate system

$$\mathbf{e}_{r_\perp} = \begin{pmatrix} \cos\varphi_r \\ \sin\varphi_r \\ 0 \end{pmatrix}, \quad \mathbf{e}_{\varphi_r} = \begin{pmatrix} -\sin\varphi_r \\ \cos\varphi_r \\ 0 \end{pmatrix}, \quad \mathbf{e}_z = \begin{pmatrix} 0 \\ 0 \\ 1 \end{pmatrix}, \tag{2.90}$$

one may write the Poynting vector (cf. Eq. (33) in [109]) as

$$\mathbf{S}(\mathbf{r},t) = S_{r_\perp}(\mathbf{r},t)\,\mathbf{e}_{r_\perp} + S_{\varphi_r}(\mathbf{r},t)\,\mathbf{e}_{\varphi_r} + S_z(\mathbf{r},t)\,\mathbf{e}_z, \tag{2.91}$$

with

$$S_{r_\perp}(\mathbf{r},t) \equiv S_{r_\perp}(\mathbf{r}) = 0\,, \tag{2.92}$$

$$\begin{aligned} S_{\varphi_r}(\mathbf{r},t) \equiv S_{\varphi_r}(\mathbf{r}) = \frac{\varkappa\,\omega^2(k)}{4\pi}\,\sin\theta_k\,J_{m_\gamma}(\varkappa\,r_\perp) \\ \times\left(\cos^2(\theta_k/2)\,J_{m_\gamma-\lambda}(\varkappa\,r_\perp) + \sin^2(\theta_k/2)\,J_{m_\gamma+\lambda}(\varkappa\,r_\perp)\right)\,, \end{aligned} \tag{2.93}$$

and

$$S_z(\mathbf{r},t) \equiv S_z(\mathbf{r}) = \frac{\varkappa\,\omega^2(k)}{4\pi}\left(\cos^4(\theta_k/2)\,J^2_{m_\gamma-\lambda}(\varkappa\,r_\perp) - \sin^4(\theta_k/2)\,J^2_{m_\gamma+\lambda}(\varkappa\,r_\perp)\right)\,. \tag{2.94}$$

Eqs. (2.91)–(2.94) demonstrate that no radial component of the Poynting vector is present, which means that no energy flow takes place in the direction transverse to

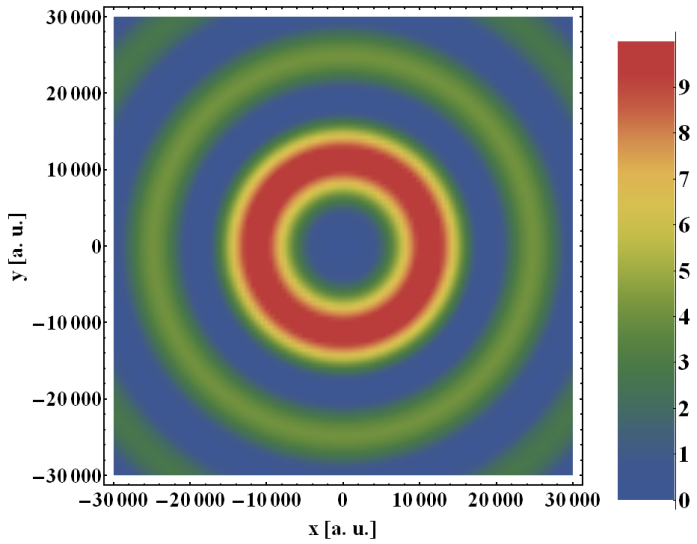

Figure 2.4. – Intensity profile of an electromagnetic Bessel wave as given by Eq. (2.95). The beam parameters are chosen as $k_z = 2.7 \cdot 10^{-2}$ a.u., $\varkappa = 2.7 \cdot 10^{-4}$ a.u., $\lambda = +1$ and $m_\gamma = +3$ corresponding to the paraxial regime. Here the typical ring structure of the intensity pattern with a well-defined (zero intensity) center can be observed.

the propagation axis. We recover therefore the well-known property that the Bessel beams are non-diffractive [107].

The Poynting vector (2.91) represents the direction of energy flow of a Bessel wave. By taking the norm of the z-component of the Poynting vector, one obtains how much energy passes through the plane transverse to the beam direction. This energy distribution is proportional to the transverse intensity profile of the Bessel beam

$$I_\perp(\mathbf{r}, t) \propto |S_z(\mathbf{r}, t)| \ . \tag{2.95}$$

In Fig. 2.4, we depict such a profile for a *paraxial* electromagnetic Bessel wave with beam parameters $k_z = 2.7 \cdot 10^{-2}$ a.u., $\varkappa = 2.7 \cdot 10^{-4}$ a.u., $\lambda = +1$ and $m_\gamma = +3$. As the figure demonstrates, Bessel waves have a complex structure of their intensity profile. As is typical for light beams carrying OAM, the intensity profile possesses a center of zero intensity also called the *vortex* of the light wave. Furthermore, for Bessel waves this dark center is surrounded by alternating low and high intensity rings. With respect to the atomic photoionization, we can expect that this complex intensity profile will have a strong influence on the spatial characteristics of the process.

Finally, we would like to demonstrate that the length scale of the intensity oscillations in the transverse profile of a Bessel beam, i. e. the distance between two

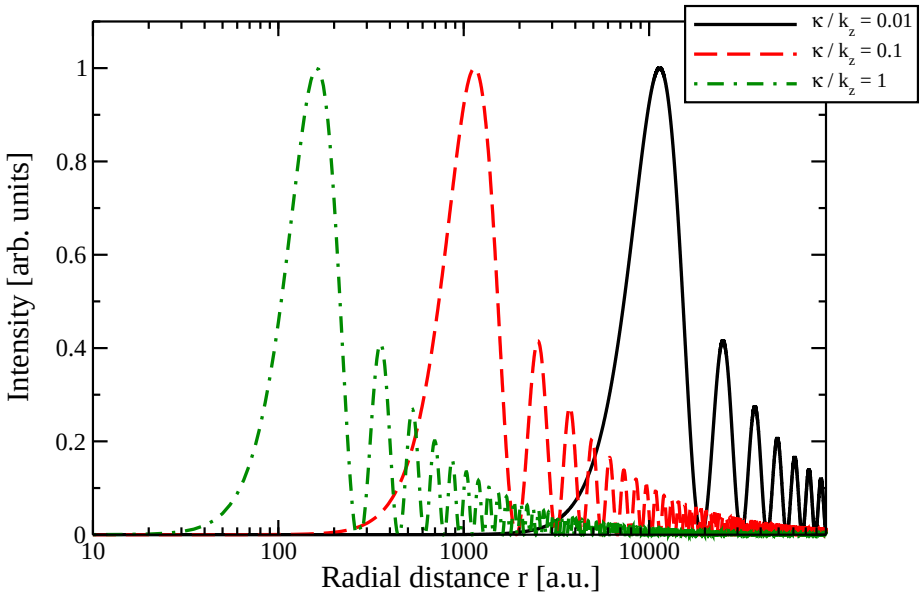

Figure 2.5. – Intensity profile of an electromagnetic Bessel wave (in arb. units) as given by Eq. (2.95) as a function of the radial distance r with respect to the beam center. The energy of the beam is fixed to 100 eV, while the longitudinal TAM and the helicity are chosen as $m_\gamma = +3$ and $\lambda = +1$, respectively. Results are shown for three different values of the ratio $s = \varkappa/k_z$ between the transverse and longitudinal momenta $\varkappa$ and k_z: $s = 0.01$ (black solid line), $s = 0.1$ (red dashed line), and $s = 1$ (green dashed-dotted line). Note that the abscissa has a logarithmic scale.

adjacent intensity maxima, may vary strongly by changing the ratio $s = \varkappa/k_z$ of the transverse and longitudinal momenta and thus the opening angle $\theta_k = \arctan(\varkappa/k_z)$ of the beam. In Fig. 2.5 we display such an intensity profile for three different values of the ratios s, $s = 0.01$ (black solid line), $s = 0.1$ (red dashed line), and $s = 1$ (green dashed-dotted line), as ranging from the paraxial ($s = 0.01$) to the non-paraxial beam regime ($s = 1$). Calculations have been performed for a beam energy of 100 eV, and for a longitudinal TAM $m_\gamma = 3$ and a helicity $\lambda = +1$. Each of the profiles has been normalized such that the first intensity maximum has a (relative) magnitude of 1 arb. unit. We note moreover that the abscissa of the figure has a logarithmic scale in order to accurately display the different length scales of the intensity oscillations. As seen from Fig. 2.5, by increasing the ratio $s = \varkappa/k_z$ and by turning therefore from the paraxial to the non-paraxial beam regime, we significantly decrease the length scale of the intensity oscillations in the beam profile. For example, for the Bessel beam with a ratio of $s = 0.01$ (solid black line), the length scale of the intensity oscillations is approximately 10^4 a.u. However, if we turn to the non-paraxial regime ($s = 1$), the radial distance between to intensity maxima considerably decreases and is of the order of 100 a.u.—two orders of magnitude smaller than for the paraxial case with $s = 0.01$.

property	plane electromagnetic wave	Bessel electromagnetic wave
linear momentum	all components of the linear momentum vector k_x, k_y, k_z are well-defined	only linear momentum k_z along the propagation direction and the absolute value $\varkappa$ of the linear momentum transverse to the propagation direction are well-defined
helicity	helicity is well-defined and either $+1$ or -1	helicity is well-defined and either $+1$ or -1
orbital angular momentum	OAM along the propagation direction is zero	OAM is unambiguously defined only within the paraxial regime $\varkappa \ll k_z$
spin angular momentum	SAM along the propagation direction is either $+1$ or -1	SAM is unambiguously defined only within the paraxial regime $\varkappa \ll k_z$
total angular momentum	TAM along the propagation direction is equal to SAM	TAM along the propagation direction is well-defined and can take any integer value $m_\gamma = 0, \pm 1, \pm 2, \ldots$

Table 2.1. – Comparison of the properties of plane and Bessel electromagnetic waves.

Comparison—Having discussed now the main properties of the Bessel light waves, let us summarize in Tab. 2.1 the similarities and differences between these waves and the plane electromagnetic waves. As seen from the table, the main similarity is that both states carry a well-defined longitudinal helicity. However, in the non-paraxial regime these light waves differ completely in their linear and angular momentum properties: plane waves, for example, carry only SAM along the propagation direction, whereas Bessel waves possess a longitudinal TAM that originates from a coupling of OAM and SAM. Moreover, all linear momentum components of a plane wave are well-defined, whereas only the longitudinal and transverse linear momenta of a Bessel wave have a particular value. Only in the paraxial regime, where the Bessel waves behave like plane waves, these properties start to match. With this comparison, we conclude our discussion on the Bessel light states and turn in the next sections to the description of electron states.

3. Quantum Theory of Electrons: Schrödinger's Equation

In the year 1926, Erwin Schrödinger published his by now famous article on the quantum mechanical description of massive particles such as electrons, atoms or molecules [110]. The heart of his theory is a partial differential equation—nowadays called the Schrödinger equation—which for a system of N particles can be written as

$$\mathrm{i}\frac{\partial}{\partial t}\,\psi(\mathbf{r}_1,\ldots,\mathbf{r}_N,t) = \widehat{\mathrm{H}}(\mathbf{r}_1,\ldots,\mathbf{r}_N,t)\,\psi(\mathbf{r}_1,\ldots,\mathbf{r}_N,t). \tag{3.1}$$

In this equation, the so-called wave function (or wavefunction) $\psi(\mathbf{r}_1,\ldots,\mathbf{r}_N,t)$ characterizes the quantum mechanical state of the particles, where $\mathbf{r}_n$, $n = 1,\ldots,N$, denotes the position coordinate of the nth particle and t the time.

The interpretation of the wave function, i.e. how it relates to the real world, has triggered a long and still ongoing debate. Here we shall adopt the probabilistic view given by the widely-established Copenhagen interpretation of quantum mechanics. A summary of its main ideas can be found in [111–115].

The Schrödinger equation (3.1) describes by its left-hand side the time-evolution of the wave function. The time-evolution is connected by the right-hand side of Eq. (3.1) to a function $\widehat{\mathrm{H}}(\mathbf{r}_1,\ldots,\mathbf{r}_N,t)$ named the Hamiltonian of the system. The Hamiltonian is an operator that acts on the wave function and characterizes the total energy of the particle system.

One usually separates the Hamiltonian into a (time-independent) part $\widehat{\mathrm{T}}(\mathbf{r}_1,\ldots,\mathbf{r}_N)$ that describes the kinetic energy of the particles and into a term $\widehat{\mathrm{V}}(\mathbf{r}_1,\ldots,\mathbf{r}_N,t)$ that represents the interactions between the particles:

$$\widehat{\mathrm{H}}(\mathbf{r}_1,\ldots,\mathbf{r}_N,\,t) = \widehat{\mathrm{T}}(\mathbf{r}_1,\ldots,\mathbf{r}_N) + \widehat{\mathrm{V}}(\mathbf{r}_1,\ldots,\mathbf{r}_N,t). \tag{3.2}$$

The kinetic energy term can be written as

$$\widehat{\mathrm{T}}(\mathbf{r}_1,\ldots,\mathbf{r}_N) = \sum_{n=1}^{N}\frac{\widehat{\mathbf{p}}_n^{\,2}}{2m_n}, \quad \widehat{\mathbf{p}}_n = -\mathrm{i}\,\frac{\partial}{\partial\,\mathbf{r}_n} \tag{3.3}$$

where m_n denotes the (rest) mass of the nth particle.

The term $\widehat{\mathrm{V}}(\mathbf{r}_1, \ldots, \mathbf{r}_N, t)$ corresponds to the (classical) interaction potential of the particles and is therefore characteristic for the system that is examined. Let us discuss in the next chapter how the Hamiltonian looks like for a system of (a) a single free electron and of (b) a hydrogen-like ion. Moreover, for these two cases we will derive the corresponding solutions of the Schrödinger equation, i.e. the wave functions $\psi(\mathbf{r}_1, \ldots, \mathbf{r}_N, t)$.

3.1. Non-Relativistic Electrons in Vacuum

In this work, we will deal with atomic processes whose theoretical analysis require to introduce the quantum states of an electron within the vacuum. We will restrict ourselves here to (relatively) small energies of the particles occurring in these processes such that the electrons can always be treated *non-relativistically*. This non-relativistic limit has certain consequences for the degrees of freedom that are necessary to describe the electrons. The spin of an electron is a purely relativistic property. Therefore we will neglect the spin component of the electron from now on.

For a non-relativistic electron in vacuum only the kinetic energy term of the Hamiltonian (3.2) remains—there are no other particles to interact with—and, hence, we obtain

$$\widehat{\mathrm{H}}_{\mathrm{free}}(\mathbf{r},\, t) = \frac{\widehat{\mathbf{p}}^2}{2}, \tag{3.4}$$

where $\widehat{\mathbf{p}} = -\mathrm{i}\,\partial/\partial\mathbf{r}$ is the momentum operator of the electron. By plugging the Hamiltonian (3.4) into the Schrödinger equation (3.1), one obtains the differential equation

$$\nabla^2\psi(\mathbf{r}, t) + 2\,\mathrm{i}\,\frac{\partial}{\partial t}\psi(\mathbf{r}, t) = 0 \tag{3.5}$$

for the wave function $\psi(\mathbf{r}, t)$ of a single electron in vacuum.

The Schrödinger equation (3.5) for an electron in free space is quite similar to the wave equation (2.13) that we have found for the vector potential of an electromagnetic wave. There are, however, two important differences. First of all, the Schrödinger equation (3.5) has only to deal with a scalar function $\psi(\mathbf{r}, t)$ and not—as for the description of light states—with a vector function $\mathbf{A}(\mathbf{r}, t)$ (cf. Eq. (2.13)). Since the vectorial character is absent for the wave function $\psi(\mathbf{r}, t)$, the electron carries no spin. In contrast to a (twisted) light wave, for which the inherent spin couples to the OAM to result in a longitudinal TAM of the light state, it is possible for a non-relativistic electron due to the absence of spin to possess a precise value of OAM along the propagation direction.

The second main difference is that the time derivative in the Schrödinger equation (3.5) is of first-order and in the wave equation (2.13) for light states of second-order. However, for the light waves it was seen that the spatial- and the time-dependency can be separated within the vector potential (cf. Eq. (2.38)). We note that such a separation is also possible for the wave function of a free electron. Therefore we expect that the free-space Schrödinger equation (3.5) leads to a similar structure of the wave function $\psi(\mathbf{r}, t)$ as has been obtained for the vector potential of a light wave. That is why we will not construct the solutions to the Schrödinger equation (3.5) from scratch but rather "guess" their structure from the knowledge previously gained from both, the plane and twisted light waves.

3.1.1. Electrons in Vacuum: Plane Wave Solutions

We will now study the structure of the wave function for plane wave electrons. To do so, we return to the vector potential of a plane electromagnetic wave (see Eq. (2.36)). By neglecting the vectorial part of this potential, we can "guess" the form of the wave function for plane wave electrons as (cf. [71])

$$\psi_{\mathbf{p}}^{\mathrm{pl}}(\mathbf{r}, t) = \mathrm{e}^{\mathrm{i}(\mathbf{p}\cdot\mathbf{r} - E_{\mathbf{p}}t)}, \tag{3.6}$$

where $\mathbf{p}$ denotes the electron momentum. Indeed, the wave function (3.6) solves the Schrödinger equation (3.5), but only if the dispersion relation

$$E_{\mathbf{p}} = \frac{\mathbf{p}^2}{2} \tag{3.7}$$

for the energy $E_{\mathbf{p}}$ of the free electron is fulfilled.

The electron states (3.6) are the equivalent to the plane electromagnetic light states (2.38). They possess a well-defined momentum $\mathbf{p}$ and energy $E_{\mathbf{p}}$. Nothing more can be said to these states, so that we can proceed now with the construction of the twisted electron states.

3.1.2. Electrons in Vacuum: Twisted Bessel Wave Solutions

Let us come now to the description of twisted electrons in terms of their wave function. For this description we will strongly draw on the knowledge we have gained in Sec. 2.3.3, where we constructed the vector potential of twisted (Bessel) light waves. Nevertheless, we have to be aware of one important difference between the electron and the light states. As has been discussed in Sec. 2.3.3, electromagnetic waves always possess SAM (due to their vectorial character) which inevitably affects an occurring OAM of the light wave. Consequently, we found that SAM and OAM

couple together and provide a particular value of TAM along the light's propagation direction, and as a result the value of OAM is not well-defined.

A non-relativistic electron as considered here does not carry SAM, since it is only a scalar particle. It may possess therefore a well-defined value of OAM along the propagation direction. We call such a (non-relativistic) electron, which carries a particular value of OAM along its propagation, a *twisted* electron. If this state additionally possesses a well-defined transverse momentum $\varkappa$ and a longitudinal momentum p_z, it is named a (twisted) Bessel wave.

A scalar function with a well-defined OAM along its propagation direction as well as transverse and longitudinal momentum has already been introduced by Eq. (2.82). Using Eq. (2.82) and adopting the propagation direction of the electron as the (quantization) z-axis, we can write the wave function of a twisted (Bessel) electron in cylindrical coordinates $(r_\perp, \varphi_r, z)$ as

$$\psi^{\mathrm{tw}}_{\varkappa m_l p_z}(\mathbf{r}, t) = \sqrt{\frac{\varkappa}{2\pi}}\, J_{m_l}(\varkappa\, r_\perp)\, \mathrm{e}^{\mathrm{i}\, m_l\, \varphi_r} \mathrm{e}^{\mathrm{i}(k_z z - E_{\varkappa p_z} t)}, \tag{3.8}$$

where m_l denotes the longitudinal OAM, and $\varkappa$ and p_z are the transverse and longitudinal linear momentum, respectively [26, 27, 116]. This expression satisfies the Schrödinger equation (3.5) if the dispersion relation

$$E_{\varkappa p_z} = \frac{p^2_{\varkappa p_z}}{2}, \quad p_{\varkappa p_z} \equiv p = \sqrt{\varkappa^2 + p_z^2} \tag{3.9}$$

between the energy $E_{\varkappa p_z}$ and the absolute momentum p of the electron is fulfilled.

Eq. (3.8) describes the quantum state of a twisted (Bessel) electron with well-defined (z-)projection of OAM m_l, transverse and longitudinal momentum $\varkappa$ and p_z as well as total energy $E_{\varkappa p_z}$. As for the light waves (cf. Eq. (2.74)), it is possible to expand the twisted electron state into plane waves:

$$\psi^{\mathrm{tw}}_{\varkappa m_l p_z}(\mathbf{r}, t) = \int a_{\varkappa m_l p_z}(\mathbf{p})\, \mathrm{e}^{\mathrm{i}(\mathbf{p}\cdot\mathbf{r} - E_{\varkappa p_z} t)}\, \mathrm{d}^3\mathbf{p}, \tag{3.10}$$

where the (Fourier) coefficients $a_{\varkappa m_l p_z}(\mathbf{p})$ are defined by Eq. (2.75). Similar to the Bessel light waves, all plane waves that contribute to the expansion (3.10) possess momentum vectors $\mathbf{p}$ which lie on a cone with opening angle $\theta_p = \arctan(\varkappa/p_z)$. We have depicted such a momentum cone in Fig. 2.2. Moreover, if we set the opening angle θ_p and thus also the transverse momentum $\varkappa$ to zero, then (i) all plane waves composing the Bessel wave travel along one axis, the z-axis, and (ii) the longitudinal OAM m_l of the Bessel wave must vanish as seen from Eq. (3.8): $J_{m_l}(\varkappa r) \to J_{m_l}(0) =$

δ_{m0}. In this case, therefore, the Bessel beam of electrons behaves like an "ordinary" plane wave beam.

Finally, we would like to illustrate the spatial structure of the electron states (3.8). This structure can be properly characterized by the *probability density* of these states:

$$\varrho_{\varkappa m_l p_z}(\mathbf{r},t) = \psi^{\mathrm{tw},*}_{\varkappa m_l p_z}(\mathbf{r},t)\cdot\psi^{\mathrm{tw}}_{\varkappa m_l p_z}(\mathbf{r},t) = \frac{\varkappa}{2\pi}J^2_{m_l}(\varkappa r_\perp), \tag{3.11}$$

which represents the probability to find the electron at a time t at a position $\mathbf{r}$. As seen from Eq. (3.11), the probability density of a Bessel wave is independent of the azimuthal angle φ_r, the z-coordinate, and of time t. Therefore the Bessel waves (3.8) are said to be *non-dispersing*, i.e. their probability density has the same (time-independent) structure in all planes transverse to the propagation direction. This transverse structure, moreover, is characterized by the squared Bessel functions $J^2_{m_l}(\varkappa r_\perp)$, and is therefore given by concentric rings of high and low electron concentrations. With this remark, let us finish our discussion on the twisted (Bessel) electron waves and turn now to the description of electronic (bound) states for hydrogen-like ions.

3.2. Non-Relativistic Hydrogen-Like Ions

When a single (non-relativistic) electron interacts with the Coulombic field of a (point-like) atomic nucleus with charge Z, the associated Hamiltonian $\widehat{\mathrm{H}}_{\mathrm{hyd}}$ can be written as [71, Eq. (3.4)]

$$\widehat{\mathrm{H}}_{\mathrm{hyd}} = \frac{\widehat{\mathbf{p}}^2}{2} - \frac{Z}{|\mathbf{r}|} \tag{3.12}$$

if we assume that the nucleus is at rest and that the nuclear mass is much larger than the electron mass. Here $\mathbf{r}$ denotes the position of the electron with respect to the nucleus and $\widehat{\mathbf{p}} = -\mathrm{i}\,\partial/\partial\,\mathbf{r}$ is momentum operator of the electron. By using spherical coordinates

$$r = \sqrt{x^2+y^2+z^2}, \quad \theta_r = \arccos(z/r), \quad \varphi_r = \arctan(y/x), \tag{3.13}$$

we can write the solutions of the Schrödinger equation (3.1) with the Hamiltonian (3.12) as

$$\psi(\mathbf{r},t) = \psi(\mathbf{r})\,\mathrm{e}^{-\mathrm{i}E_n t}, \quad \psi(\mathbf{r}) \equiv \psi_{nlm}(\mathbf{r}) = g_{nl}(r)\,Y_{lm}(\theta_r,\varphi_r). \tag{3.14}$$

Here $Y_{lm}(\theta_r, \varphi_r)$ denote spherical harmonics [117, pp. 200–203], whereas the radial wave function $g_{nl}(r)$ is given by [72, Eq. (9.10)]

$$g_{nl}(r) = \sqrt{\left(\frac{2Z}{n}\right)^3 \frac{(n-l-1)!}{2n(n+l)!}}\, \mathrm{e}^{-Z\,r/n} \left(\frac{2Zr}{n}\right)^l L_{n-l-1}^{(2l+1)}(2Zr/n), \tag{3.15}$$

where $L_{n-l-1}^{(2l+1)}(2Zr/n)$ is an associated Laguerre polynomial [71, pp. 166–169].

The parameter n—the so-called principal quantum number—determines the binding energy

$$E_n = Z^2/(2n^2) \tag{3.16}$$

of the electronic bound states (3.14). Moreover, the state (3.14) possesses well-defined values of the modulus and the longitudinal component of the OAM:

$$\widehat{\mathbf{L}}^2\, \psi_{nlm}(\mathbf{r}) = l\,(l+1)\, \psi_{nlm}(\mathbf{r})\,, \tag{3.17}$$

$$\widehat{\mathrm{L}}_z\, \psi_{nlm}(\mathbf{r}) = m\, \psi_{nlm}(\mathbf{r}), \tag{3.18}$$

where l and m denote the orbital and magnetic quantum number, respectively.

Often, we will need the Fourier-transform of the bound states (3.14):

$$\psi_{nlm}(\mathbf{r}) = (2\pi)^{-3/2} \int \widetilde{\psi}_{nlm}(\mathbf{p}')\, \mathrm{e}^{\mathrm{i}\,\mathbf{p}'\cdot\mathbf{r}}\, \mathrm{d}^3\mathbf{p}', \tag{3.19}$$

$$\widetilde{\psi}_{nlm}(\mathbf{p}') = (2\pi)^{-3/2} \int \psi_{nlm}(\mathbf{r})\, \mathrm{e}^{-\mathrm{i}\,\mathbf{p}'\cdot\mathbf{r}}\, \mathrm{d}^3\mathbf{r}. \tag{3.20}$$

For the bound electron states (3.14) the expansion (3.19)–(3.20) is well-known [72, 118]:

$$\begin{aligned}\widetilde{\psi}_{nlm}(\mathbf{p}') = 2^{2l+2}\, l!\, (-\mathrm{i})^l\ n^{-l-2} \sqrt{\frac{2\,(n-l-1)!}{\pi Z^3 (n+l)!}} \left(\frac{p'}{Z}\right)^l \frac{Z^{2l+4}}{(p'^2+\delta^2)^{l+2}} \\ \times\, C_{n-l-1}^{l+1}\left(\frac{p'^2-\delta^2}{p'^2+\delta^2}\right) Y_{lm}(\theta_{p'}, \varphi_{p'}),\end{aligned} \tag{3.21}$$

where $\delta = Z/n$ and $C_{n-l-1}^{l+1}(x)$ is a so-called Gegenbauer polynomial [72, p. 169].

The wave function (3.14) describe the electronic bound state of a hydrogen-like ion with well-defined quantum numbers n, l and m. To illustrate the spatial structure of such a state, we employ the corresponding electron probability density:

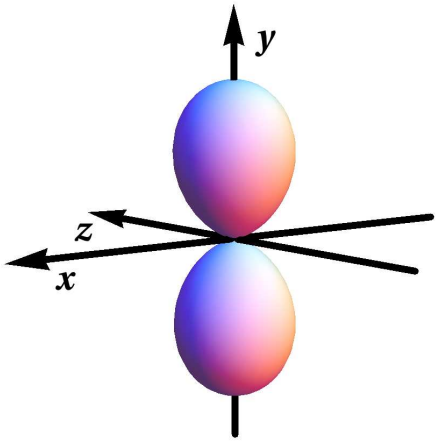

Figure 3.1. – Probability density of the $2p_y$-level of a hydrogen-like ion. The electron cloud of this state is strongly concentrated around the y-axis.

$$\varrho_{nlm}(\mathbf{r}) = \psi^*_{nlm}(\mathbf{r}) \cdot \psi_{nlm}(\mathbf{r}). \tag{3.22}$$

If we plug the wave function (3.14) into Eq. (3.22), we obtain (after some simple algebra) a probability density $\varrho_{nlm}(\mathbf{r}) \equiv \varrho_{nlm}(r, \theta_r)$ that is cylindrical symmetric around the quantization axis. With respect to atomic processes, such a symmetric probability density often leads to measurements—for example, of the angular distribution of electrons in the photoionization process—that reflect this symmetry.

For the analysis of atomic processes, it can be rewarding to break the cylindrical symmetry, and to employ states with a more complex structure of the electron cloud. For example, we consider the $2p_y$-level [71, pp.95–97] of a hydrogen-like ion

$$\psi_{2p_y}(\mathbf{r}) = \frac{1}{\sqrt{2}\,\mathrm{i}} \left(\psi_{2,1,+1}(\mathbf{r}) + \psi_{2,1,-1}(\mathbf{r})\right), \tag{3.23}$$

which is defined as a superposition of the two magnetic substates $n = 2$, $l = 1$, $m = \pm 1$. Such a state can be populated, for example, by optical pumping from the ground state of the ion with light that possesses a linear polarization along the y-axis as is shown in Appendix B. In Fig. 3.1, we display the shape of the probability density of this state. As seen from the figure, the electron cloud of the $2p_y$-state is concentrated around the y-axis and, hence, possesses a pronounced shape that is not spherically symmetric around the quantization z-axis. Both, the "standard" wave functions (3.14) of a hydrogen-like ion as well as the $2p_y$-state, will be used later to analyze the atomic ionization process with twisted photons. This concludes our discussion on the free and bound electron states.

4. Quantum Dynamics of Atomic Processes: Perturbation Theory

So far, we have discussed how to describe the physical states of particles—photons, electrons and ions—that occur in the atomic processes of photoionization and radiative recombination. But when we analyze an atomic process, we must also specify how these particles interact, how we physically "guide" them through the interaction process in question. A well-established and often-used method to describe this "guiding" is given by the *time-dependent first-order perturbation theory*.

We will outline the main ideas of this theory below. Of course, such a well-established theory has been extensively discussed elsewhere [70–72] and thus it is not our aim to provide a lengthy account on the underlying formalism. Here we will rather focus on the basic formulas that are needed to analyze the atomic photoionization and radiative recombination process—both with plane and twisted particle waves.

4.1. Time-Dependent First-Order Perturbation Theory

Suppose a Hamiltonian $\widehat{\mathrm{H}}$ of some quantum system that is separated into a time-independent and a time-dependent part as

$$\widehat{\mathrm{H}}(\mathbf{r},t) = \widehat{\mathrm{H}}_{\mathrm{main}}(\mathbf{r}) + \widehat{\mathrm{H}}_{\mathrm{pert}}(\mathbf{r},t). \tag{4.1}$$

Here $\widehat{\mathrm{H}}_{\mathrm{pert}}$ shall be a "small" (time-dependent) *perturbation*, e.g. some external electromagnetic field, that "disturbs" the (main) Hamiltonian $\widehat{\mathrm{H}}_{\mathrm{main}}$—which describes, for example, some atom, ion, or molecule.

It is well-known that the perturbation $\widehat{\mathrm{H}}_{\mathrm{pert}}(\mathbf{r},t)$ may trigger transitions between the states of the main quantum system $\widehat{\mathrm{H}}_{\mathrm{main}}(\mathbf{r})$ [71, 72]. Assume, for example, that the system resides at some time t_0 in a stationary eigenstate $\psi_i(\mathbf{r})$ of $\widehat{\mathrm{H}}_{\mathrm{main}}$. The perturbation $\widehat{\mathrm{H}}_{\mathrm{pert}}(\mathbf{r},t)$ can then "drive" the system away from this initial state. The probability to find the system in an (eigen)state $\psi_f(\mathbf{r})$ of $\widehat{\mathrm{H}}_{\mathrm{main}}$ at some later time t is given in first-order perturbation theory by [71, cf. Eq. (2.344)]

$$P_{fi}(t) = \left| \int_{t_0}^{t} M_{fi}(t') \, \exp\left[\mathrm{i} \left(E_f - E_i \right) t' \right] \mathrm{d}t' \right|^2 . \tag{4.2}$$

where E_i and E_f characterize the energy of the states labelled by i and f, respectively.

The *transition probabilities* (4.2) mainly depend on the so-called *transition amplitudes*

$$M_{fi}(t') = \int \psi_f^*(\mathbf{r}) \, \widehat{\mathrm{H}}_{\mathrm{pert}}(\mathbf{r}, t') \, \psi_i(\mathbf{r}) \, \mathrm{d}^3\mathbf{r} \tag{4.3}$$

that describe the "guiding" of an (initially) prepared state $\psi_i(\mathbf{r})$ to a (final) state $\psi_f(\mathbf{r})$ as caused by the perturbation Hamiltonian $\widehat{\mathrm{H}}_{\mathrm{pert}}(\mathbf{r}, t)$. These amplitudes, or also called *transition matrix elements*, serve as the basic quantities in order to characterize the transition probabilities (4.2).

Until now, we left undefined the explicit form of the perturbation Hamiltonian, which can take, of course, many different forms. In what follows, however, we will often need the transition probability (4.2) as well as the transition amplitudes (4.3) if the system is influenced by a time-harmonic perturbation.

4.1.1. Transition Probability for Harmonic Perturbations

Assume a perturbation that is harmonic in time with angular frequency ω:

$$\widehat{\mathrm{H}}_{\mathrm{pert}}(\mathbf{r}, t) = \widehat{\mathrm{A}}(\mathbf{r}) \, \mathrm{e}^{\mathrm{i}\omega t} + \widehat{\mathrm{A}}^\dagger(\mathbf{r}) \, \mathrm{e}^{-\mathrm{i}\omega t}, \tag{4.4}$$

where $\widehat{\mathrm{A}}(\mathbf{r})$ is an arbitrary, time-independent operator and $\widehat{\mathrm{A}}^\dagger(\mathbf{r})$ is its adjoint. By inserting the Hamiltonian (4.4) into Eqs. (4.2)–(4.3) and by neglecting the (usually small) interference term, we may derive the (time-dependent) probability that such a perturbation induces a transition between an initial state $\psi_i(\mathbf{r})$ and a final state $\psi_f(\mathbf{r})$ in the form

$$P_{fi}(t) = P_{fi,\,\mathrm{abs}}(t) + P_{fi,\,\mathrm{emis}}(t). \tag{4.5}$$

As seen from Eq. (4.5), the transition probability for a harmonic perturbation can be written as a sum of two terms. These terms may be written as [71, cf. Eq. (2.367)]

$$P_{fi,\,\mathrm{abs}}(t) = 4 \left| M_{if}^* \right|^2 \frac{\sin^2\left[\left(E_f - E_i - \omega \right) t/2 \right]}{\left(E_f - E_i - \omega \right)^2} \tag{4.6}$$

and [71, cf. Eq. (2.370)]

$$P_{fi,\,\mathrm{emis}}(t) = 4\big|M_{fi}\big|^2 \, \frac{\sin^2\!\Big[\Big(E_f - E_i + \omega\Big)t/2\Big]}{\Big(E_f - E_i + \omega\Big)^2}\,. \tag{4.7}$$

The physical meaning of both terms is well-known: while the first term represents the process that the main system absorbs an amount of energy $\Delta E \approx \omega$ delivered by the perturbation, the second term describes the inverse process where an amount of energy $\Delta E \approx \omega$ is emitted by the system—for example, a photon (representing the perturbation) is absorbed or emitted by an atom (the main system).

The evaluation of the transition probabilities (4.6)–(4.7) can be reduced to the (now time-independent) transition amplitudes (see Eq. (4.3))

$$M_{fi} = \int \psi_f^*(\mathbf{r})\, \widehat{\mathrm{A}}(\mathbf{r})\, \psi_i(\mathbf{r})\, \mathrm{d}^3\mathbf{r}. \tag{4.8}$$

These amplitudes provide the main building blocks in order to analyze the transition probabilities for different processes. Moreover, they constitute the *central objects* for our analysis of the atomic ionization with twisted photons or the radiative recombination with twisted electrons. In these processes, they do not only serve to characterize the transition probabilities but also other (related) observables such as *angular or polarization distributions* of the emitted particles. Let us therefore study in the next section how one represents the transition amplitudes in these processes.

4.2. Interaction of Hydrogen-Like Ions with External Electromagnetic Fields

When an electron simultaneously interacts with a (point-like) nucleus of charge Z and an external electromagnetic field characterized by a vector potential $\mathbf{A}(\mathbf{r}, t)$, the associated Hamiltonian reads [71, Eqs. (4.24)–(4.28)]

$$\widehat{\mathrm{H}}(t) = \frac{\widehat{\mathbf{p}}^2}{2} - \frac{Z}{r} + \mathbf{A}(\mathbf{r}, t) \cdot \widehat{\mathbf{p}}, \quad \widehat{\mathbf{p}} = -\mathrm{i}\,\partial/\partial\,\mathbf{r}, \tag{4.9}$$

where we assumed that the electromagnetic field is (relatively) weak and that its vector potential $\mathbf{A}(\mathbf{r}, t)$ satisfies the Coulomb gauge (2.12). The first two terms in Eq. (4.9) describe the Coulombic interaction between the electron and the nucleus, whereas the third term characterizes the electromagnetic interaction between the electron and the external electromagnetic field.

We will only deal with time-harmonic electromagnetic fields in this work and thus we may write the vector potential as

$$\mathbf{A}(\mathbf{r},t) = \mathbf{A}(\mathbf{r})\,\mathrm{e}^{\mathrm{i}\omega t} + \mathbf{A}^*(\mathbf{r})\,\mathrm{e}^{-\mathrm{i}\omega t}. \tag{4.10}$$

In this case, the perturbation theory developed in the previous section is applicable to the Hamiltonian (4.9), and we interpret the electron-nucleus interaction as the unperturbed part, while the external field is considered as a perturbation. The corresponding transition amplitudes (4.8) read

$$M_{fi} = \int \psi_f^*(\mathbf{r}) \left(\mathbf{A}(\mathbf{r}) \cdot \hat{\mathbf{p}}\right) \psi_i(\mathbf{r})\,\mathrm{d}^3\mathbf{r}. \tag{4.11}$$

Eq. (4.11) illustrates that the process of photon emission or absorption is completely determined by the initial and final states $\psi_i(\mathbf{r})$ and $\psi_f(\mathbf{r})$ of the unperturbed Hamiltonian—which describes here the interaction between electron and nucleus—and by the spatial behaviour of the electromagnetic field in terms of its vector potential $\mathbf{A}(\mathbf{r})$. In particular, such a vector potential may represent plane-wave photon beams as well as twisted-wave photon beams. Therefore, Eq. (4.11) provides the basis to analyze the atomic process of photoionization and radiative recombination not only with plane waves but also with twisted wave particles. Such an analysis will be done now within the next chapters.

5. Atomic Photoionization: Advanced Studies

When a light beam transverses some target sample—a solid, liquid, or gas—an electron that is initially bound to one of the target atoms may be emitted out of its atomic shell by absorbing one or several photons from the beam; we referred to such a process as the *atomic photoeffect* or *atomic photoionization*. Several questions immediately arise: how can we experimentally detect this process and what are the characteristic quantities that can be measured—that is, what are the observables? And how can we theoretically describe these observables?

The first question is easy to answer. If a photon of the light beam ionizes an ion (or atom), then the total electric charge of the ion is reduced and one or several free electrons are created. Thus if we detect the "down-charged ions" together with the emitted electrons—which is easily doable with present-day detectors—we know that an atomic ionization process took place.

The answer to the second question is longer, since there are many quantities that can possibly be observed. For example, by counting the number of ionization events, one can infer the so-called *total ionization rate*, i.e. the probability that an ionization process occurs within a unit of time. Such ionization rates have been extensively studied for various atoms and ions as well as for different photon energies, both in experiment and theory [74–77]. These studies have not only provided insights into the kinematics and dynamics of the ionization process itself but have also yielded valuable knowledge on relativistic, many-electron and quantum electrodynamical effects in the fundamental photon-electron interaction.

Beside the total rates, there exist many studies that focus on the *angle-differential* or *angular* distribution of the emitted electrons—that is, how "many" electrons are emitted into a certain direction with respect to the position of the atomic target [79–82]. These angle-differential studies are often more sensitive to the electronic structure of the target atoms (or ions) than measurements of the ionization rates, and may therefore provide an additional and unique tool to gain information of the ionization process and subsequently of the underlying electron-photon interaction. It is therefore that in this work we will solely focus our analysis of the ionization process on the angular distribution of the emitted electrons.

Finally, the third question remains: how do we theoretically describe such an angular distribution of the photoelectrons, in particular, for the atomic photoeffect (of hydrogen-like ions) by twisted (Bessel) electromagnetic waves? The answer to

this question will be the main topic of this chapter. However, to properly answer it we will first take one step back; that is, in the next section we will first introduce how one usually describes the angular distribution of electrons that are emitted in the "standard" photoionization process by *plane wave photons*. Such an analysis will provide an appropriate bridge to the advanced photoionization studies with twisted light beams.

5.1. Atomic Photoionization of Hydrogen-Like Ions by Plane Waves

Before we can analyze the atomic photoeffect with plane electromagnetic waves, we must first agree on the geometrical setup: that is, where we position the atomic target with respect to the photon beam, and in which direction we observe the emitted electron with respect to both, the atomic target and the photon beam. Alongside, we will also introduce an appropriate coordinate system that will later help us to mathematically describe the ionization process.

5.1.1. Geometrical Setup

Let us begin now to characterize the incoming photon beam. For this beam, we choose a circularly-polarized plane wave with helicity λ and wave vector $\mathbf{k}$; the direction of the wave vector will serve, moreover, as the (quantization) z-axis of the coordinate system, i.e. $\mathbf{k} = (0, 0, k_z)$, as depicted in Fig. 5.1. The structure of such a light state in terms of its vector potential was introduced in Sec. 2.2 (cf. Eq. (2.38)).

The atomic target, moreover, shall consist of a single hydrogen-like ion that is positioned within the wave front of the photon beam; the atomic position defines the origin of the coordinate system. We still possess the freedom to fix the internal electronic state of the ion. Here we will distinguish between two cases: the initial (bound) state of the electron is chosen to be either (i) a hydrogenic level with well-defined quantum numbers (n, l, m) (cf. Eq. (3.14)) or (ii) the hydrogenic $2p_y$-level (cf. Eq. (3.21)).

Each of these two scenarios not only requires a different way to characterize the coordinate system but also has different consequences for the emission process of the electron. For the first scenario, the ion "plus" photon system possesses an axial symmetry around the propagation (z-)direction of the light. Thus there is no "natural way" to define the arrangement of the x- and y-axis and we can choose them arbitrarily. The emitted electron will reflect the cylindrical symmetry—that is, the angular distribution of the photoelectrons will be also axially symmetric. In this case, only the polar angle θ_p is needed to characterize the emitted electrons.

For the second scenario, however, the electron cloud of the $2p_y$-level shows a strong orientation along some axis which we will adopt as the y-axis. The x-axis is chosen

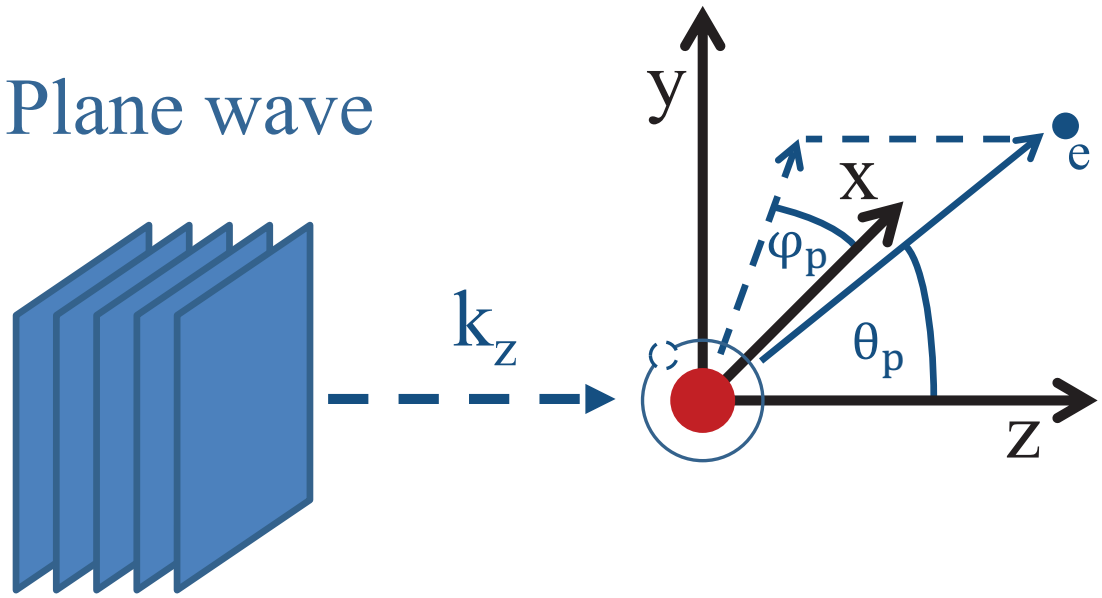

Figure 5.1. – Geometry of atomic photoionization with (circularly polarized) plane electromagnetic waves. The propagation direction of the photon wave defines the (quantization) z-axis. The origin of the coordinate system is given by the position of the (hydrogen-like) ion. The bound state of the electron is either given by (i) a hydrogenic level with well-defined quantum numbers n, l and m or (ii) the hydrogenic $2p_y$-level. For the first case, the system of (circularly polarized) wave "plus" atom is cylindrical symmetric around the z-axis, and one can choose the configuration of the x- and y-axes of the coordinate system arbitrarily. In the second scenario, the electron cloud of the $2p_y$-level is strongly oriented along some axis which thus can be taken as the y-axis.

such that the coordinate system is right-handed. In this scenario, the strongly-oriented $2p_y$-state "breaks" the axial symmetry of the ion-photon system so that two angles, the azimuthal angle φ_p and the polar angle θ_p, are needed to described the direction of the emitted photon.

In the next section, we will begin—using the geometry presented above—with the analysis of the atomic photoionization process by plane wave photons.

5.1.2. Angular Distribution of Photoelectrons

When a plane electromagnetic wave ionizes an atom or ion, one usually finds that the electrons are preferentially emitted in certain directions; if we count how many electrons are emitted into some direction, we obtain an angle-differential emission pattern—the angular distribution of the emitted electrons. In atomic theory, this angular distribution is usually described as the *probability* that an electron is emitted

under some solid angle $\Omega_p = (\theta_p, \varphi_p)$ with respect to the target atom. It is well-known how such a probability can be expressed in first-order perturbation-theory. Following Ref. [71, cf. Eq. (4.202)], we may write such a probability as

$$W_{fi}^{\mathrm{pl}}(\theta_p, \varphi_p) = \mathcal{N}^{\mathrm{pl}} \left| M_{fi}^{\mathrm{pl}}(\theta_p, \varphi_p) \right|^2, \tag{5.1}$$

where $\mathcal{N}^{\mathrm{pl}}$ is an appropriate normalization constant that we will discuss later. Expression (5.1) illustrates that the emission pattern of the electrons crucially depends on the transition amplitudes $M_{fi}^{\mathrm{pl}}(\theta_p, \varphi_p)$ (cf. Eq. (4.8)) that describe here the ionization process with plane wave photons.

To characterize the transition amplitudes, we have to specify three quantities (as discussed in Sec. 4.2): the initial and final state $\psi_i(\mathbf{r})$ and $\psi_f(\mathbf{r})$ of the (bound and subsequently free) electron, and the spatial part of the vector potential $A(\mathbf{r})$ that describes the light beam. Here we consider the ionization process with a plane electromagnetic wave and therefore the vector potential is given by Eq. (2.38). The final state of the electron, which shall describe the electron emission into a solid angle $\Omega_p = (\theta_p, \varphi_p)$, is *approximated* by a plane wave as described by the wave function (3.6). Although such a plane wave approximation, also called Born approximation, neglects the post-interaction of the electron with the atomic nucleus, it is well-justified for small nuclear charges Z and photon energies higher than the ionization threshold (and low enough so that the emitted electron is still non-relativistic) [71]. In this work, we will always work in a regime where the plane wave approximation is valid. Regarding the initial bound state of the electron, we have to consider two possibilities: (i) the electron is either in a hydrogenic bound-state with well-defined quantum numbers (n, l, m) (cf. Eq. (3.14)) or (ii) it is in the hydrogenic $2p_y$-level (cf. Eq. (3.23)).

If we insert the bound and continuum wave functions (3.14) and (3.6) of the electron, and the plane wave vector potential (3.6) of the light beam into expression (4.11) for the transition amplitudes, we obtain for scenario (i) an amplitude of the form

$$M_{fi}^{\mathrm{pl}}(\theta_p, \varphi_p) \equiv M_{nlm}^{\mathrm{pl}}(\theta_p, \varphi_p) = (\mathbf{e}_{\mathbf{k}\lambda} \cdot \mathbf{p}) \int \psi_{nlm}(\mathbf{r})\, \mathrm{e}^{-\mathrm{i}\,(\mathbf{p}-\mathbf{k})\cdot\mathbf{r}}\, \mathrm{d}^3\mathbf{r}, \tag{5.2}$$

where $\mathbf{e}_{\mathbf{k}\lambda}$ is the helicity vector (2.32). The resulting integral for the transition amplitudes can be easily evaluated to [71]

$$M_{nlm}^{\mathrm{pl}}(\theta_p, \varphi_p) = (2\pi)^{3/2}\, (\mathbf{e}_{\mathbf{k}\lambda} \cdot \mathbf{p})\, \widetilde{\psi}_{nlm}(\mathbf{q}) \tag{5.3}$$

by using the Fourier-transform $\widetilde{\psi}_{nlm}$ of the hydrogenic bound state wave function, which has been introduced by Eq. (3.20). Here we defined $\mathbf{q} = \mathbf{p} - \mathbf{k}$, a quantity

which represents the momentum transfer between the incoming photon and the final electron.

The transition amplitudes (5.3) allow us to obtain the angular distribution of the photoelectrons. Inserting the transition amplitudes (5.3) into Eq. (5.1) leads to

$$\begin{aligned} W_{fi}^{\mathrm{pl}}(\theta_p, \varphi_p) \equiv W_{nlm}^{\mathrm{pl}}(\theta_p, \varphi_p) &= \mathcal{N}^{\mathrm{pl}} \left| M_{nlm}^{\mathrm{pl}}(\theta_p, \varphi_p) \right|^2 \\ &= \mathcal{N}^{\mathrm{pl}} \sqrt{2\pi^3}\, p^2 \, \sin^2\theta_p \left| \widetilde{\psi}_{nlm}(\mathbf{q}) \right|^2 , \end{aligned} \tag{5.4}$$

where the $\sin^2\theta_p$-dependency results from the square of the term $(\mathbf{e}_{\mathbf{k}\lambda} \cdot \mathbf{p})$ of the transition amplitudes. Eq. (5.4) provides the final form for the angular distribution of the photoelectrons that are emitted in the ionization process of hydrogen-like ions by circularly polarized plane wave photons. This expression for the angular distribution will be used later in order to understand and interpret the results for the atomic ionization process with twisted wave photons.

For the second scenario—the ionization of the hydrogenic $2p_y$-level—one can trace the associated transition amplitudes back to the ones that have been derived above for the ionization of a hydrogen (n, l, m)-level (cf. Eq. (5.3)). As a reminder, the $2p_y$-level is a superposition of states with the same n and l, $n = 2$ and $l = 1$, but with different magnetic quantum numbers $m = +1$ and $m = -1$. Taking the prefactor $1/(\sqrt{2}\,\mathrm{i})$ of these levels into account, one may write the corresponding transition amplitudes as

$$M_{2p_y}^{\mathrm{pl}}(\theta_p, \varphi_p) = \frac{1}{\sqrt{2}\,\mathrm{i}} \left(M_{2,1,1}^{\mathrm{pl}}(\theta_p, \varphi_p) + M_{2,1,-1}^{\mathrm{pl}}(\theta_p, \varphi_p) \right). \tag{5.5}$$

The angular distribution for this case follows again from Eq. (5.1) and reads

$$W_{2p_y}^{\mathrm{pl}}(\theta_p, \varphi_p) = \mathcal{N}^{\mathrm{pl}} \sqrt{\pi^3/2}\, p^2 \, \sin^2\theta_p \left| M_{2,1,1}^{\mathrm{pl}}(\theta_p, \varphi_p) + M_{2,1,-1}^{\mathrm{pl}}(\theta_p, \varphi_p) \right|^2 \tag{5.6}$$

Eqs. (5.4) and (5.6) describe the photoelectron distribution in the ionization process of different hydrogenic bound states by plane wave photons. We will use these equations to interpret the results for the ionization process with Bessel electromagnetic waves—which will be examined within the next section.

5.2. Atomic Photoionization of Hydrogen-Like Ions by Bessel Waves

In the previous section, we recapitulated how one derives the angular distribution for electrons that are emitted in the atomic photoeffect with non-relativistic photons.

We have done so in order to provide a proper theoretical basis for the analysis of the ionization process with twisted (Bessel) photons, which will be the topic of this section.

5.2.1. Geometrical Setup

Bessel light beams have a completely different structure than plane wave beams and, hence, the ionization process requires a different geometrical setup. Let us elaborate on this setup in more detail.

Imagine a Bessel beam that is propagating (with longitudinal momentum k_z) along some axis, which we will adopt as the (quantization) z-axis of a coordinate system, as shown in Fig. 5.2. As discussed in Sec. 2.3.6, such a twisted light beam possesses a pronounced intensity profile transverse to its propagation direction—alternating concentric rings of high and low intensity. With respect to the ionization process, somewhere within the structure of this Bessel wave we have to place the atomic target. In contrast to plane wave photons (with planar wave fronts), however, the (transverse) atomic position within the wave front of the Bessel beam may play a crucial role for the ionization process. Such an atomic position with respect to the center of the light beam is denoted by us as the (atom-photon) impact parameter and will be labelled as $\mathbf{b}_\perp$. Moreover, the x-axis of our coordinate system is chosen to go through the atomic position, while the origin of the coordinate system shall lie within the beam center, i.e. $\mathbf{b}_\perp = (b, 0, 0)$.

Regarding the bound states of the electron, we will distinguish again—as for the ionization with plane wave photons—between two cases. In the first scenario, the bound electron is described by (i) the hydrogenic state (3.14) with well-defined quantum numbers (n, l, m), whereas in the second scenario we will use (ii) the (strongly-oriented) $2p_y$-state (3.23). For both cases, the direction of the emitted electron will now be described by two angles: the azimuthal angle φ_p and the polar angle θ_p.

5.2.2. Angular Distribution of Photoelectrons

As we have done for the photoeffect with plane electromagnetic waves, we study now the angular distribution of the photoelectrons for the ionization by twisted photons. Again, we can write this angular distribution in the form

$$W_{fi}^{\mathrm{tw}}(\theta_p, \varphi_p) = \mathcal{N}^{\mathrm{tw}} \left| M_{fi}^{\mathrm{tw}}(\theta_p, \varphi_p) \right|^2, \tag{5.7}$$

that relies on the transition amplitudes M_{fi}^{tw} of the ionization process, and where $\mathcal{N}^{\mathrm{tw}}$ is a normalization constant that we will discuss later. The transition amplitudes depend—as for the plane wave case—on the initial (bound) and final (continuum) wave functions ψ_i and ψ_f of the electron as well as on the vector potential $\mathbf{A}^{\mathrm{tw}}_{\varkappa m_\gamma k_z \lambda}(\mathbf{r})$ of the incoming light beam:

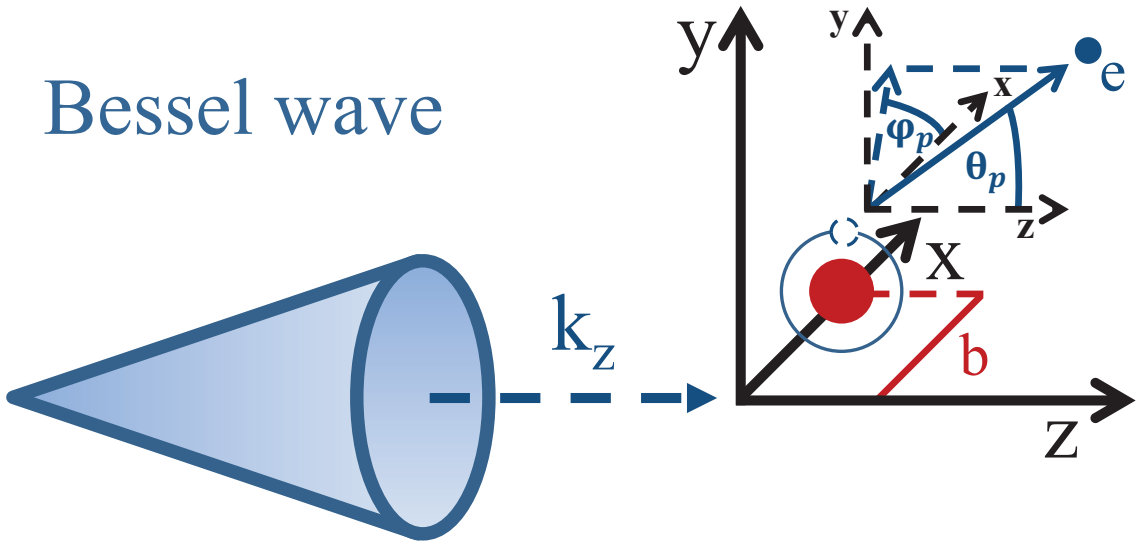

Figure 5.2. – Geometry for the ionization process by Bessel light beams. The propagation direction of the beam serves as the quantization z-axis. The atomic position with regard to the beam center can be used to define the x-axis of the coordinate system. The emitted electron is then described by the axial angle φ_p and the polar angle θ_p.

$$M_{fi}^{\mathrm{tw}}(\theta_p, \varphi_p) = \int \psi_f^*(\mathbf{r}) \left(\mathbf{A}^{\mathrm{tw}}_{\varkappa m_\gamma k_z \lambda}(\mathbf{r}) \cdot \widehat{\mathbf{p}} \right) \psi_i(\mathbf{r} - \mathbf{b}_\perp) \, \mathrm{d}^3\mathbf{r} \,. \tag{5.8}$$

The vector potential in Eq. (5.8) represents a twisted Bessel light wave with (transverse and longitudinal) momenta $\varkappa$ and k_z, helicity λ and longitudinal TAM m_γ, and is therefore given by Eqs. (2.74)–(2.75). With regard to the electron states, the initial (bound) state is again either given by (i) the hydrogenic level (3.14) with well-defined quantum numbers n, l and m, or by (ii) the hydrogenic $2p_y$-state (3.23). It must be noted, however, that in Eq. (5.8) these (initial) states are spatially translated out of the center of the Bessel beam by the transverse vector $\mathbf{b}_\perp$: $\psi_i(\mathbf{r}) \to \psi_i(\mathbf{r} - \mathbf{b}_\perp)$, as demanded by the chosen geometrical setup (see Fig. 5.2). The final state, moreover, shall again—as for the ionization process with plane waves—be approximated by a plane wave with momentum $\mathbf{p} = p\,(\cos\varphi_p \, \sin\theta_p, \sin\varphi_p \, \sin\theta_p, \cos\theta_p)^T$ as given by Eq. (3.6).

For the first scenario (i), by using the plane wave expansion (2.74) of the Bessel waves and the Fourier-transform (3.19) of the electronic bound state, we can write the transition amplitudes (5.8) as

$$M_{fi}^{\mathrm{tw}}(\theta_p,\varphi_p) \equiv M_{nlm}^{\mathrm{tw}}(\theta_p,\varphi_p) = (2\pi)^{-3/2} \int a_{\varkappa m_\gamma k_z}(\mathbf{k})\, \widetilde{\psi}_{nlm}(\mathbf{p}')\ (\mathbf{e}_{\mathbf{k}\lambda}\cdot\mathbf{p}')\ \mathrm{e}^{\mathrm{i}(\mathbf{k}+\mathbf{p}'-\mathbf{p})\cdot\mathbf{r}}\,\mathrm{d}^3\mathbf{k}\,\mathrm{d}^3\mathbf{p}'\,\mathrm{d}^3\mathbf{r}, \tag{5.9}$$

where the functions $a_{\varkappa m_\gamma k_z}(\mathbf{k})$ are given by Eq. (2.75). In expression (5.9) one can easily perform the integration over $\mathbf{r}$ and $\mathbf{p}'$ by using [71, Eq. (2.35)]

$$\int \mathrm{e}^{\mathrm{i}(\mathbf{k}+\mathbf{p}'-\mathbf{p})\cdot\mathbf{r}}\,\mathrm{d}^3\mathbf{r} = (2\pi)^3\delta(\mathbf{k}+\mathbf{p}'-\mathbf{p}), \tag{5.10}$$

so that

$$M_{nlm}^{\mathrm{tw}}(\theta_p,\varphi_p) = (2\pi)^{3/2} \int a_{\varkappa m_\gamma k_z}(\mathbf{k})\, \widetilde{\psi}_{nlm}(\mathbf{p}-\mathbf{k})\ (\mathbf{e}_{\mathbf{k}\lambda}\cdot\mathbf{p})\ \mathrm{d}^3\mathbf{k}, \tag{5.11}$$

We can simplify the amplitudes (5.11) if we employ the explicit form (2.75) of the functions $a_{\varkappa m_\gamma k_z}(\mathbf{k})$ (and especially of the delta distributions within):

$$M_{nlm}^{\mathrm{tw}}(\theta_p,\varphi_p) = (-\mathrm{i})^{m_\gamma}\sqrt{\varkappa}\int_0^{2\pi} \mathrm{e}^{\mathrm{i}m_\gamma\varphi_k}\,\mathrm{e}^{-\mathrm{i}\mathbf{b}_\perp\cdot(\mathbf{p}-\mathbf{k})}\,(\mathbf{e}_{\mathbf{k}\lambda}\cdot\mathbf{p})\,\widetilde{\psi}_{nlm}(\mathbf{p}-\mathbf{k})\,\mathrm{d}\varphi_k \tag{5.12}$$

with $\mathbf{k} = (\varkappa\cos\varphi_k, \varkappa\sin\varphi_k, k_z)$. The remaining integration over φ_k in the matrix elements (5.12) can be evaluated analytically by applying the residue theorem from complex variable theory [119]. However, the calculation is rather tedious and lengthy and therefore we will shift it to Appendix C. As shown there, the final result for the transition amplitude reads

$$\begin{aligned} M_{nlm}^{\mathrm{tw}}(\theta_p,\varphi_p) = 2\pi\, c_{\mathrm{tw}} \sum_{\sigma=0}^{l}\sum_{\mu=-\sigma}^{\sigma}\sum_{\nu=-\infty}^{\infty} \mathrm{i}^{m_\gamma+m+\nu-\mu}\, h_{\sigma,\mu}(\theta_p,\varphi_p) f_\nu(\theta_p,\varphi_p)\,\mathrm{e}^{-\mathrm{i}\mathbf{b}_\perp\cdot\mathbf{p}} \\ \times\Big(\mathrm{i}\,\frac{p_\perp}{\sqrt{2}}\,c_{-1}(\lambda,\theta_k)\,\mathrm{e}^{-\mathrm{i}\varphi_p}\,J_{m_\gamma+m+\nu-\mu+1}(\varkappa b_\perp) + p_z\,c_0(\lambda,\theta_k)\,J_{m_\gamma+m+\nu-\mu}(\varkappa b_\perp) \\ +\mathrm{i}\,\frac{p_\perp}{\sqrt{2}}\,c_{+1}(\lambda,\theta_k)\,\mathrm{e}^{\mathrm{i}\varphi_p}\,J_{m_\gamma+m+\nu-\mu-1}(\varkappa b_\perp)\Big) \end{aligned} \tag{5.13}$$

Here $h_{\sigma,\mu}(\theta_p, \varphi_p)$, $f_\nu(\sigma_p, \varphi_p)$ and $c_{\rm tw}$ denote special mathematical functions (or expressions) that are discussed in Appendix C. Moreover, the functions $c_i(\lambda, \theta_k)$, $i = 0, \pm 1$, are defined by Eq. (2.67). As seen from Eq. (5.13), the transition amplitudes can be written as an *infinite sum* over Bessel functions $J_i(x)$. However, if one restricts the calculations of these amplitudes to low lying hydrogenic levels and to rather small photon energies, it is sufficient to include only the first few terms of the sum in order to get an accurate result.

The amplitudes (5.13) are the main objects in order to investigate the angular distribution of the electrons emitted during the atomic ionization by twisted (Bessel) photons. By plugging these amplitudes into Eq. (5.1), we may obtain the electron angular distribution in the following form:

$$W^{\rm tw}_{nlm}(\theta_p, \varphi_p) = \mathcal{N}^{\rm tw}_{nlm} \left| M^{\rm tw}_{nlm}(\theta_p, \varphi_p) \right|^2 , \tag{5.14}$$

where the electron is assumed to be initially in the hydrogenic (n, l, m)-bound state.

We also have to discuss how we may obtain the angular distribution for the second scenario, where the electron initially resides in the hydrogenic $2p_y$-level. Since the $2p_y$-level is a superposition of two magnetic sublevels, we may relate the associated angular distribution of the photoelectrons to the amplitudes (5.13) as

$$W^{\rm tw}_{2p_y}(\theta_p, \varphi_p) = (\mathcal{N}^{\rm tw}_{2p_y}/2) \left| M^{\rm tw}_{2,1,+1}(\theta_p, \varphi_p) + M^{\rm tw}_{2,1,-1}(\theta_p, \varphi_p) \right|^2 . \tag{5.15}$$

Eq. (5.14)–(5.15) together with the relation (5.13) for the transition amplitude provide the basis to analyze the photoelectron angular distribution for the ionization process by Bessel light beams. In Chapter 7, we will use these equations to analyze the emission pattern of the photoelectrons for different scenarios. Before we do so, however, we will introduce in the next chapter how one can (theoretically) treat the cross-channel to the photoionization process by twisted photons: the radiative recombination with twisted electrons.

6. Radiative Recombination: Advanced Studies

When an electron is captured into a bound state of an atom or ion and emits simultaneously a photon, we speak of the so-called *atomic radiative recombination* [71]. Such a radiative capture process has been in the focus of intense scientific research for decades, both in experiment and theory [83–94]. For example, many studies were performed at storage ring and electron beam ion trap (EBIT) facilities to explore the *total capture rates* of the RR process for a variety of ion species and collision energies [83–87]. These investigations considerably helped to better understand the fundamental electron-photon interaction, particularly with respect to many-electron, relativistic or QED effects.

Beside the total rates, much attention has been paid to the *angular emission patterns* of the recombination photons, again for various ion species and different kinetic energies of the collision partners [88–91]. These angle-differential studies provide a unique tool for atomic structure investigations, since they are often more sensitive to the electronic configurations of the atomic bound states. To describe these distributions in theory, one usually represents them in terms of the *probability* $W(\mathbf{k})$ to emit a photon into a certain direction $\mathbf{k}$. Such a probability can be accurately calculated within the *time-dependent first-order perturbation theory*, as we will show later in Sec. 6.1.2.

In addition to their emission patterns, it is also possible to register the polarization state of the emitted photons with the help of polarization-sensitive detectors [92–94]. Such a polarization-sensitive analysis provides not only complementary information on the (angle-differential) atomic structure investigations but gives also unique insights into how the photon (as well as electron) spin may affect the RR process. Since later in this chapter we will also be confronted with such a polarization analysis, let us discuss in more detail how we may describe the polarization state of RR photons.

In order to quantify the polarization state of the recombination photons, one usually employs the so-called Stokes parameters. These parameters characterize asymmetries between measured intensities of photons in different polarization states. Since these parameters will be of particular importance in the course of this work, let us discuss them here in more detail. To do so, we have to characterize the polarization detector that registers the RR photons. Assume that an electron with momentum $\mathbf{p}$ is traveling along some axis. This electron shall be radiatively captured by an ion

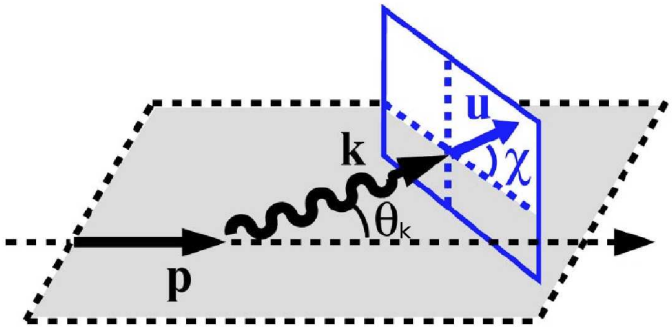

Figure 6.1. – Definition of polarization axis for a polarization-sensitive detector. An electron with momentum **p** is radiatively captured by an ion so that a photon is emitted under a polar angle θ_k with wave vector **k**. Together the electron momentum and photon wave vector form the so-called (electron-photon) *reaction plane* $\mathcal{R}$. Let us further assume that the electron is detected by a polarization-sensitive detector which acts as a polarization filter for linear polarization. The polarization axis **u** of this filter is defined by the angle χ with respect to the reaction plane. Image is taken from [93].

such that a photon with wave vector **k** is emitted under an angle θ_k, as shown in Fig. 6.1. The propagation direction of the electron and the wave vector of the photon form the so-called photon-electron *reaction plane* $\mathcal{R}$. Moreover, we suppose that the photon detector acts as a linear polarization filter with its polarization axis **u** tilted by an angle χ out of the reaction plane: $\chi = \angle(\mathbf{u}, \mathcal{R})$. We denote the number of photon counts (or the count rate) that such a detector registers as $W(\theta_k, \chi)$.

We come back now to the definition of the Stokes parameters (for which we will follow Ref. [117]). The first Stokes parameter P_1 is represented by the relative differences in the count rates of light that is linearly polarized within or perpendicular to the reaction plane:

$$P_1(\theta_k) = \frac{W(\theta_k, 0°) - W(\theta_k, 90°)}{W(\theta_k, 0°) + W(\theta_k, 90°)}, \tag{6.1}$$

whereas for the second Stokes parameter P_2 the polarization axes are rotated by 45°:

$$P_2(\theta_k) = \frac{W(\theta_k, 45°) - W(\theta_k, 135°)}{W(\theta_k, 45°) + W(\theta_k, 135°)}. \tag{6.2}$$

For the definition of the third Stokes parameter, instead of measuring the state of linear polarization, we assume that the polarization-sensitive detector can distinguish between photons that are either left ($\lambda = -1$) or right ($\lambda = +1$) circularly polarized. The corresponding count rates shall be denoted by $W(\theta_k, \lambda)$. Then we can define the third Stokes parameter P_3, also called the *degree of circular polarization*, as

$$P_3(\theta_k) = \frac{W(\theta_k, +1) - W(\theta_k, -1)}{W(\theta_k, +1) + W(\theta_k, -1)}. \tag{6.3}$$

This parameter characterizes the relative difference between the count rates of left and right circularly-polarized photons (that are emitted in the direction θ_k).

As mentioned above, the angular distribution and the polarization state (in terms of the Stokes parameters) of photons emitted in RR have been extensively investigated throughout the years, both in experiment and theory. However, usually the RR studies are restricted to the "standard" case of *plane wave* electron beams—beams with zero OAM along the propagation direction. A new *degree of freedom* may be introduced to these studies by employing *twisted* electron beams which carry a well-defined OAM $\hbar m$ along their propagation direction. These twisted beams promise to provide new insights into the RR process, especially on effects that originate from a transfer of OAM during the radiative capture process.

In this chapter, we will lay out the theoretical foundations to describe the radiative capture of twisted electrons by bare ions. In particular, we will investigate the angular and polarization properties of the RR photons for the radiative capture processes of twisted (Bessel) wave electrons. To obtain a concise description of these properties, it has been found convenient to use the so-called *density matrix formalism*. A brief introduction to this formalism will be given within the next section.

6.1. Density Matrix Formalism: Photon-Spin Density Matrix

Within the density matrix framework, the physical state of a quantum mechanical system is completely described by the so-called *statistical* or *density operator* $\widehat{\rho}$. This operator description is well-elaborated and there exist many text books that report on this topic [117, 120, 121]. Here we are particularly interested in such a description of photon states. To represent the density operator of photons, one usually works within the helicity basis

$$\rho^{\gamma}_{\lambda\lambda'} = \langle \mathbf{k}\lambda | \widehat{\rho}_{\gamma} | \mathbf{k}\lambda' \rangle \,, \tag{6.4}$$

where $|\mathbf{k}\lambda\rangle$ represents the state of a circularly-polarized plane wave with wave vector $\mathbf{k}$ and helicity λ. We call the quantity (6.4) the *photon-spin density matrix* to the density operator $\widehat{\rho}_{\gamma}$.

Two questions arise now: (a) how can we obtain the photon-spin density matrix for the photons that are emitted in the RR process and (b) how do we relate its matrix elements (6.4) to the observables—angular distribution and Stokes parameters—of the RR process? Let us come to the first question within the next section.

6.1.1. Photon-Spin Density Matrix of Recombination Photons

To describe the spin density-matrix (6.4) for the photons that are emitted in the RR process, we will work within the first-order perturbation theory that we introduced in Sec. 4. As we discovered there, the central objects of the perturbation theory are the transition amplitudes of the process in question. With regard to the RR process, it is well-known how one can relate the corresponding transition amplitudes M_{fi} to the spin density matrix (6.4) of the emitted photons [89, 93, 117]:

$$\langle \mathbf{k}\lambda | \widehat{\rho}_\gamma | \mathbf{k}\lambda' \rangle = \sum_f M^*_{fi}(\mathbf{k}, \lambda) M_{fi}(\mathbf{k}, \lambda'). \tag{6.5}$$

Here the sum goes over all final (f) electronic bound states that remain energetically unresolved within the RR process, that is, in the non-relativistic regime one may determine the principal quantum number n of the bound state by energy conservation between the incoming electrons and the emitted photons, but cannot resolve the orbital or magnetic substate (as given by the quantum numbers l and m). As seen from Eq. (6.5), the photon-spin density matrix for the RR process exclusively depends on a sum of products of the transition amplitudes $M_{fi}(\mathbf{k}, \lambda)$. These amplitudes describe the electromagnetic interaction between the electron (that is to be captured) and the emitted (plane wave) RR photon and are given therefore by (see Eq. (4.11)):

$$M_{fi}(\mathbf{k}, \lambda) = \int \psi^*_f(\mathbf{r}) \left(\mathbf{A}^{\mathrm{pl},*}_{\mathbf{k}\lambda}(\mathbf{r}) \cdot \widehat{\mathbf{p}} \right) \psi_i(\mathbf{r}) \, \mathrm{d}^3\mathbf{r}, \tag{6.6}$$

where $\psi_i(\mathbf{r})$ and $\psi_f(\mathbf{r})$ describe the initial (free) and final (bound) electron wave function and where $\mathbf{A}^{\mathrm{pl}}_{\mathbf{k}\lambda}(\mathbf{r})$ is the vector potential of the outgoing photon with momentum $\mathbf{k}$ and helicity λ (see Eq. (2.38)).

Eqs. (6.5)–(6.6) completely determine the density matrix of the photons that are emitted in the RR process (with arbitrary initial (free) and final (bound) states $\psi_i(\mathbf{r})$ and $\psi_f(\mathbf{r})$ of the electron). However, to make use of this density matrix we also have to know how it relates to the observables of the RR process: the angular distributions and polarization states of the RR photons. We will provide these relations in the next section.

6.1.2. Photon-Spin Density Matrix: Relation to Observables

In the previous section we have seen how to calculate the elements of the photon-spin density matrix from the RR transition amplitudes. Yet at the same time, this calculation would be of little use if we would not know how to relate the density matrix to the observables of the RR process. In the following, therefore, we will outline how to represent these observables in terms of the density matrix elements. Such

a representation is well-known and has been discussed at several points throughout the literature [89, 93, 117]. For instance, the photon-spin density matrix (6.4) allows us to express the probability to measure a photon within a certain direction $\mathbf{k}$—the angular distribution of the photons—as [117]

$$W(\mathbf{k}) = \mathcal{N}\big(\langle \mathbf{k}, \lambda = +1 | \widehat{\rho}_\gamma | \mathbf{k}, \lambda' = +1 \rangle + \langle \mathbf{k}, \lambda = -1 | \widehat{\rho}_\gamma | \mathbf{k}, \lambda' = -1 \rangle\big), \tag{6.7}$$

where $\mathcal{N}$ is a normalization constant that we will specify later. As seen from Eq. (6.7), the angular distribution of the RR photons can be simply written as the trace of the density matrix, i.e. the sum over its diagonal elements.

Beside the emission pattern, the spin density matrix (6.4) also enables us to derive the Stokes parameters of the recombination photons as [117]

$$P_1 = -\frac{\langle \mathbf{k}, \lambda = +1 | \widehat{\rho}_\gamma | \mathbf{k}, \lambda' = -1 \rangle + \langle \mathbf{k}, \lambda = -1 | \widehat{\rho}_\gamma | \mathbf{k}, \lambda' = +1 \rangle}{\langle \mathbf{k}, \lambda = +1 | \widehat{\rho}_\gamma | \mathbf{k}, \lambda' = +1 \rangle + \langle \mathbf{k}, \lambda = -1 | \widehat{\rho}_\gamma | \mathbf{k}, \lambda' = -1 \rangle}, \tag{6.8}$$

$$P_2 = \mathrm{i}\,\frac{\langle \mathbf{k}, \lambda = -1 | \widehat{\rho}_\gamma | \mathbf{k}, \lambda' = +1 \rangle - \langle \mathbf{k}, \lambda = +1 | \widehat{\rho}_\gamma | \mathbf{k}, \lambda' = -1 \rangle}{\langle \mathbf{k}, \lambda = +1 | \widehat{\rho}_\gamma | \mathbf{k}, \lambda' = +1 \rangle + \langle \mathbf{k}, \lambda = -1 | \widehat{\rho}_\gamma | \mathbf{k}, \lambda' = -1 \rangle}, \tag{6.9}$$

$$P_3 = \frac{\langle \mathbf{k}, \lambda = +1 | \widehat{\rho}_\gamma | \mathbf{k}, \lambda' = +1 \rangle - \langle \mathbf{k}, \lambda = -1 | \widehat{\rho}_\gamma | \mathbf{k}, \lambda' = -1 \rangle}{\langle \mathbf{k}, \lambda = +1 | \widehat{\rho}_\gamma | \mathbf{k}, \lambda' = +1 \rangle + \langle \mathbf{k}, \lambda = -1 | \widehat{\rho}_\gamma | \mathbf{k}, \lambda' = -1 \rangle}. \tag{6.10}$$

As seen from the above expressions, the Stokes parameters can be expressed (up to some prefactor) as simple ratios of sums and differences of the density matrix elements.

Eqs. (6.5)–(6.10) provide the basis to study the (angular and polarization) properties of photons that are emitted in the RR process. Up to now, these equations are most general; that is, they facilitate the general description of the RR process not only for *plane* but also *twisted* electron beams. Before we begin, however, to analyze the RR process with twisted electrons, let us first examine within the next section the main characteristics of the recombination photons for the capture of *plane wave* electrons. Such a study of the plane wave case will serve as an appropriate introduction to the advance analysis of the recombination process with twisted electrons.

6.2. Radiative Capture of Plane Wave Electrons by Bare Ions

Before we can begin to discuss the radiative capture of plane wave electrons, we need to introduce the geometrical setup of such a process. In particular, we shall

describe such a setup independent of any specific coordinate system. That is, we will characterize the geometrical setup only in terms of the momentum vectors $\mathbf{p}$ and $\mathbf{k}$ of the incoming electron and outgoing photon. Such a *coordinate-free* description enables us to derive the transition amplitudes of the plane wave RR in the most general form—a form with the great advantage that it can be re-used later for the description of the RR process with twisted electrons. We must note here that parts of the following discussion will be similar to our (preprint) manuscript [122] that is submitted to New J. Phys.

6.2.1. Geometrical Setup

Here we will describe the geometrical setup for the RR process with plane wave electrons. Assume that a plane wave electron with momentum $\mathbf{p}$ is captured into a bound state of an (initially) bare ion, while simultaneously a photon with wave vector $\mathbf{k}$ is emitted, as shown in Fig. 6.2. Here we restrict ourselves to the simplest case: the capture into the $1s$ ground state (K-shell) of the ion. Moreover, the emitted photon shall be observed by an appropriate photon detector; which kind of photon detector we take here depends on the quantity that we want to investigate. To measure the angular distribution of the photons, for example, it is sufficient to use a polarization-insensitive detector. However, if we would like to measure the first two Stokes parameters, a detector sensitive to linear polarization should be used (cf. Eqs. (6.1)–(6.2)), whereas for the third Stokes parameter we should use a detector that can distinguish between left- and right-handed circular polarization (cf. Eq. (6.3)).

This concludes our discussion on the geometrical setup for the RR process with plane wave electrons. Based on this setup, we will perform in the next section a theoretical analysis of the plane wave RR process.

6.2.2. Angular Distribution and Polarization of Recombination Photons

In Sec. 6.1.2, we established the theoretical description of the RR process based on the density matrix formalism. Within this formalism, the basic properties of the RR photons are reduced to the spin density matrix (6.4). Eventually, we found that the density matrix can be expressed by the transition amplitudes (6.6) that describe the radiative capture of the electron. The initial and final electron states occurring within these amplitudes should now be chosen accordingly to the geometrical setup of the RR process as introduced in Sec. 6.2.1.

The initial state $\psi_i(\mathbf{r})$ of the free electron should represent an incoming wave with a linear momentum $\mathbf{p}$. Here we will *approximate* this state as a *plane wave* (3.6): $\psi_i(\mathbf{r}) = \psi^{\mathrm{pl}}_{\mathbf{p}}(\mathbf{r})$. Although such a *plane wave* approximation neglects the interaction

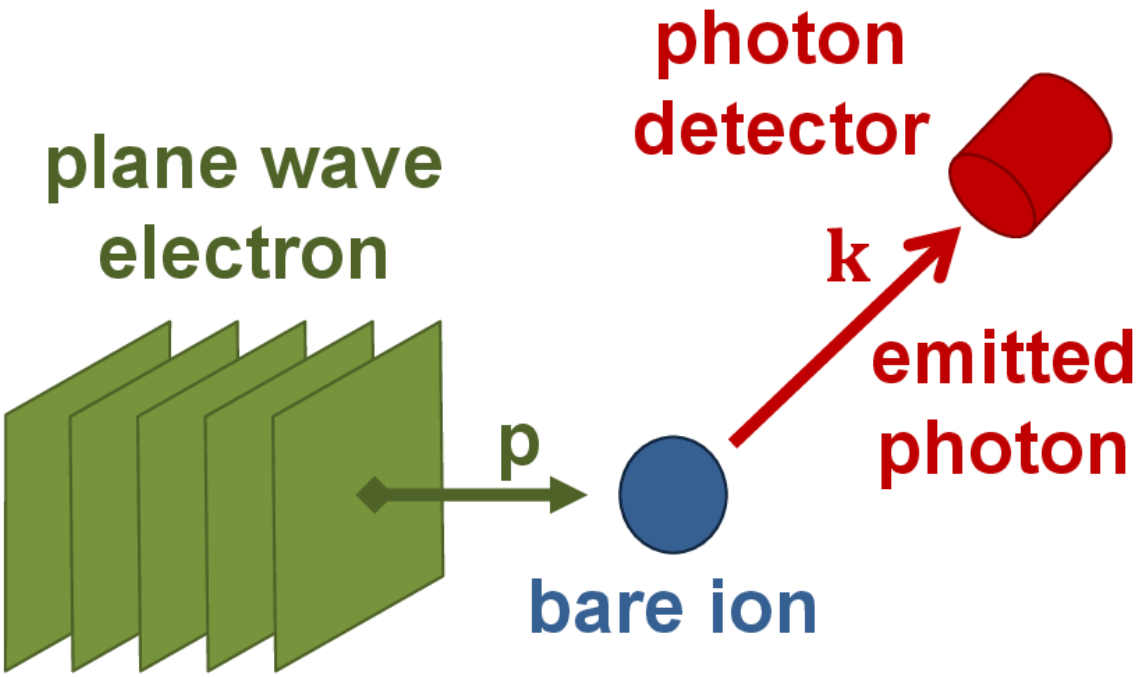

Figure 6.2. – Geometry for radiative recombination with plane wave electrons. An electron with momentum **p** is radiatively captured into the bound state of an ion. Here we restrict ourselves to the capture into the 1*s* ground state (K-shell) of the ion. In the capture process, a photon is emitted, which shall subsequently be detected by a photon detector. To measure only the angular distribution of the photons, it is sufficient to use a polarization-insensitive detector. However, to determine the Stokes parameters, one has to use detectors that measure the (linear or circular) polarization state of the photon.

between the incoming electron and the nucleus before the capture process, it is well-justified for kinetic energies of the incoming electrons that are much higher (but still non-relativistic) in comparison to the ionization threshold of the ion [71]. For the analysis of the RR process, we will always work in a regime of the kinetic energies that is sufficient for the plane wave approximation to be valid. We note moreover that we use such an approximation, since it has the great advantage that one can derive analytical formulas for the transition amplitudes of the electron capture process.

Coming to the (final) bound state of the electron, which should describe an electron within the K-shell of an ion with charge Z, we employ the Schrödinger-solution $\psi_{nlm}(\mathbf{r})$ (cf. Eq. (3.14)) but taken for the (K-shell) quantum numbers $n = 1$, $l = 0$ and $m = 0$, i.e. $\psi_f(\mathbf{r}) \equiv \psi_{1,0,0}(\mathbf{r})$. Employing the wave functions (3.6) and (3.14) and using expression (4.11) for the radiative transition amplitudes, we may derive the matrix element $M_{fi}(\mathbf{k}, \lambda)$ for the emission of a photon into the direction $\mathbf{k}$ and with circular polarization λ as [71]

$$
\begin{aligned}
M_{fi}^{\mathrm{pl}}(\mathbf{k},\lambda) \equiv M_{\mathbf{p}}^{\mathrm{pl}}(\mathbf{k},\lambda) &= \int \psi_{1,0,0}^{*}(\mathbf{r})\, \mathrm{e}^{-\mathrm{i}\mathbf{k}\cdot\mathbf{r}} (\mathbf{e}_{\mathbf{k}\lambda}^{*}\cdot\widehat{\mathbf{p}})\, \psi_{\mathbf{p}}^{\mathrm{pl}}(\mathbf{r})\, \mathrm{d}^3\mathbf{r} \\
&= (\mathbf{e}_{\mathbf{k}\lambda}^{*}\cdot\mathbf{p}) \int \psi_{1,0,0}(\mathbf{r})\, \mathrm{e}^{\mathrm{i}(\mathbf{p}-\mathbf{k})\cdot\mathbf{r}}\, \mathrm{d}^3\mathbf{r} \\
&= (2\pi)^{3/2}\, (\mathbf{e}_{\mathbf{k}\lambda}^{*}\cdot\mathbf{p})\, \widetilde{\psi}_{1,0,0}(\mathbf{k}-\mathbf{p}) = 8\sqrt{\pi}\, Z^{5/2}\, \frac{(\mathbf{e}_{\mathbf{k}\lambda}^{*}\cdot\mathbf{p})}{\big((\mathbf{p}-\mathbf{k})^2+Z^2\big)^2},
\end{aligned}
\tag{6.11}
$$

where the Fourier-transformed bound-state wave functions $\widetilde{\psi}_{1,0,0}$ have been used (see Eq. (3.21)) and where we employed for the second equality that $\psi_{1,0,0}$ is a real function.

By using now the amplitudes (6.11) together with expression (6.5), we obtain the photon-spin density matrix for the K-shell capture of plane wave electrons as

$$
\langle \mathbf{k}\lambda|\widehat{\rho}_{\gamma}|\mathbf{k}\lambda'\rangle = M_{\mathbf{p}}^{\mathrm{pl},*}(\mathbf{k},\lambda)\, M_{\mathbf{p}}^{\mathrm{pl}}(\mathbf{k},\lambda') = 64\,\pi\, Z^5\, \frac{(\mathbf{e}_{\mathbf{k}\lambda}\cdot\mathbf{p})\,(\mathbf{e}_{\mathbf{k}\lambda'}^{*}\cdot\mathbf{p})}{\big((\mathbf{p}-\mathbf{k})^2+Z^2\big)^4}
\tag{6.12}
$$

As was discussed in Sec. 6.1.2, the density matrix (6.12) gives access to the main observables of the RR process. For example, by taking the trace of the density matrix (6.12), one may write the angular distribution of the RR photons as

$$
W(\mathbf{k}) = \mathcal{N}^{\mathrm{pl}} \frac{64\,\pi\, Z^5}{\big((\mathbf{p}-\mathbf{k})^2+Z^2\big)^4} \sum_{\lambda=\pm1} \big|(\mathbf{e}_{\mathbf{k}\lambda}\cdot\mathbf{p})\big|^2.
\tag{6.13}
$$

To simplify this expression, we turn now to the case where the electron momentum $\mathbf{p} = (0,0,p)^T$ is aligned with the z-axis of a coordinate system. Then we recover the well-known formula [71, cf. Eq. (4.208)]

$$
W(\mathbf{k}) \equiv W(\theta_k) = \mathcal{N}^{\mathrm{pl}}\, 64\,\pi\, Z^5\, \frac{p^2\, \sin^2(\theta_k)}{(p^2+k^2-2pk\cos\theta_k+Z^2)^4},
\tag{6.14}
$$

where θ_k denotes the (polar) angle between the propagation directions of the incoming electron and the emitted photon. Expression (6.14) demonstrates that the photon angular distribution for the K-shell capture is axially symmetric around the propagation direction of the incoming electron, and that in the polar direction it mainly follows a $\sin^2(\theta_k)$-distribution—a behaviour that is similar for the electron distribution in the "inverse" process of K-shell ionization by plane electromagnetic waves (see Eq. (5.4)). The angular dependency on $\cos\theta_k$ in the denominator becomes important only for high electron energies (of the order of 1 keV for $Z = 1$).

In the same manner as for the photon angular distribution, one can derive from the density matrix (6.12) the Stokes parameters P_i by using Eqs. (6.8)–(6.10). By taking again the momentum of the incoming electron along the z-axis, $\mathbf{p} = (0, 0, p)^T$, the Stokes parameters can be obtained in a simple form [93]:

$$P_1 = 1, \quad P_2 = 0, \quad P_3 = 0. \tag{6.15}$$

As seen from this expression, only the first Stokes parameter P_1 is non-zero and is furthermore equal to one, $P_1 = 1$, regardless of the emission angle θ_k. In other words, for the capture of a plane wave electron into the K-shell of an ion, the emitted photons are completely linearly polarized and their (linear) polarization vector lies within the photon-electron reaction plane.

Expressions (6.13) and (6.15) completely characterize the emission pattern and the polarization state of photons that are emitted in the radiative capture of electrons to the $1s$ ground state of an initially bare ion. We will use these expressions later in order to understand and interpret the results that we will obtain for the capture process of twisted electrons. Let us finally turn to such a RR process with twisted electrons in the next section.

6.3. Radiative Capture of Twisted Electrons by Bare Ions

In this section, we will provide a detailed account on the radiative recombination of (initially) bare ions and twisted electrons. Before we do so, however, we have to specify how we set up a possible experiment that gives access to the observables of such a capture process, i.e. the emission pattern and the polarization of the recombination photons.

6.3.1. Geometrical Setup

Twisted electrons possess a non-plane wavefront that is characterized by a complex transverse structure of their wave function (3.8). Because of this structure, it is to expect that the radiative capture of twisted electrons by ions proceeds differently than the RR with plane wave electrons. One of these differences, for example, is that the spatial structure of the electron beam will impose certain constraints onto the geometrical setup of a RR experiment. In the following, we will describe one possibility for such a geometrical setup, a setup which will rely on the head-on collision of a twisted electron beam with an ion beam.

The setup shall be as follows: We assume that a (twisted) Bessel beam of electrons is propagating along some axis, whereas a second (target) beam consisting of bare

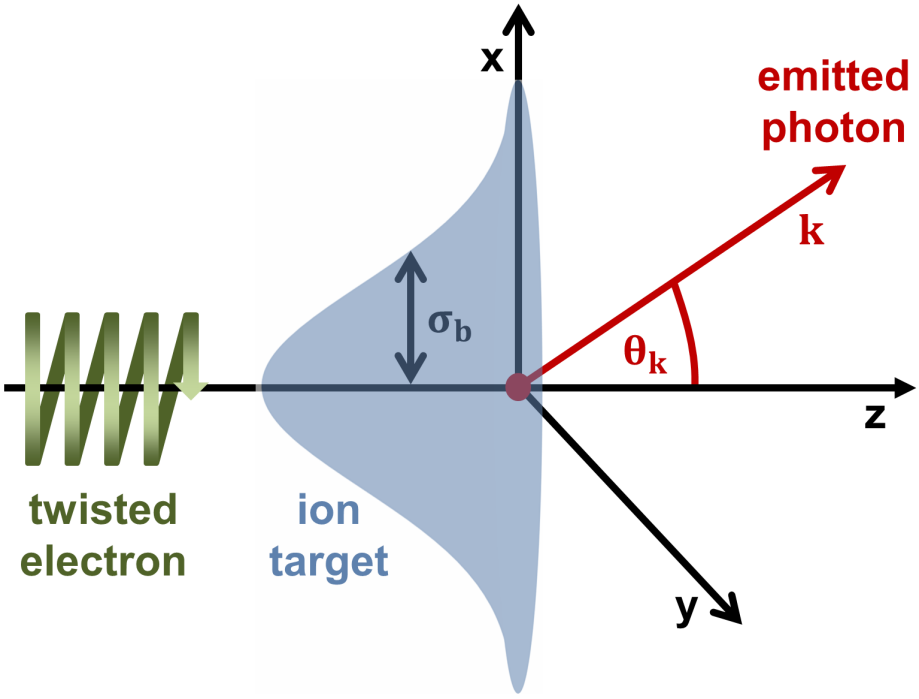

Figure 6.3. – Geometry of radiative recombination with twisted electrons. The propagation direction of the twisted electron beam defines the (quantization) z-axis. An electron of the incoming beam shall be radiatively captured by one of the ions from a counter-propagating ion beam. The density of the ion beam is assumed to follow a Gaussian distribution within the plane transverse to the propagation direction. Moreover, the photon that is emitted in the radiative capture shall be detected under a polar angle θ_k.

ions shall be counter-propagating to this electron beam, as shown in Fig. 6.3. If we let these two beams collide head-on, an electron may be radiatively captured by one of the ions, thus constituting the RR process. The photon emitted in such a radiative capture shall be observed by a photon detector that is placed somewhere around the point where the two beams collide. This detector can be polarization-insensitive if we only want to measure the angular distribution of the RR photons, but if we would like to determine the Stokes parameters, this detector shall act as a polarization filter for either linear or circular polarization. Additionally, this detector shall be able to determine the energy of the emitted photons. If we then suppose that the kinetic energies of electron and ion beam are well-defined and if we consider that the energy is conserved in the RR process, we can determine to which bound state of the ions the electrons were captured. Here we will always consider the simplest case: an electron capture to the $1s$ ground state (K-shell) of the ions.

In the collision process presented above, the electron beam possesses due to its twisted nature a pronounced transverse structure of its electron density. Thus if the

electron beam collides with the ion beam, it may also "notice" the density distribution within the ion beam. Consequently, we also have to specify the (transverse) spatial structure of the ion beam. As typical for electron-ion collision experiments, we assume that the spatial distribution of the ions within the ion beam is given by a Gaussian function

$$f(\mathbf{b}_\perp) = (2\pi\sigma_b^2)^{-1}\, \mathrm{e}^{-\mathbf{b}_\perp^2/(2\sigma_b^2)}, \tag{6.16}$$

where σ_b is the *characteristic width* or *length* of the distribution and $\mathbf{b}_\perp$ denotes the (transverse) distance with respect to the center of the ion beam. Furthermore, we shall suppose that the centers of electron and ion beam are aligned with each other, as shown in Fig. 6.3.

Finally, we would like to define an appropriate coordinate system in which we can properly treat the theoretical analysis of the recombination process. As shown in Fig. 6.3, we take the propagation direction of the twisted electron beam as the (quantization) z-axis. The x-z-plane, moreover, shall coincide with the electron-photon *reaction plane* as given by the directions of the incoming electron beam and the outgoing photon. As a consequence, the direction of the emitted photon can be described by a single (polar) angle, which we denote as θ_k. We note, furthermore, that we will always work within the *rest frame* of the ion beam. This concludes our discussion on the geometrical setup for the RR process with twisted electrons. Based on this setup, we will develop in the next section the theoretical formalism to analyze the radiative capture of twisted electrons by bare ions.

6.3.2. Photon-Spin Density Matrix for RR with Twisted Electrons

Having discussed the geometrical setup for the RR process with twisted electrons, we are ready now to analyze the corresponding photon-spin density matrix as well as the angular distribution and the polarization state of the recombination photons. As for RR with plane wave electrons, the theoretical description of the recombination process with twisted electrons in terms of the photon-spin density matrix (6.5) ultimately depends on the transition amplitudes (6.6), and thus on the initial and final electron wave functions:

$$M_{fi}^{\mathrm{tw}}(\mathbf{k},\lambda) = \int \psi_f^*(\mathbf{r})\, \mathrm{e}^{-\mathrm{i}\mathbf{k}\cdot\mathbf{r}}\, (\mathbf{e}_{\mathbf{k}\lambda}^* \cdot \widehat{\mathbf{p}})\, \psi_i(\mathbf{r})\, \mathrm{d}^3\mathbf{r} \tag{6.17}$$

According to the geometry that we presented in the previous section, the initial state of the electron shall be described by a twisted Bessel wave that propagates along the z-direction. If we denote the transverse and longitudinal momentum of this wave as

$\varkappa$ and p_z and the longitudinal OAM as m, we can represent such an (initially) free electron state as $\psi_i(\mathbf{r}) = \psi^{\mathrm{tw}}_{\varkappa m p_z}(\mathbf{r})$, where $\psi^{\mathrm{tw}}_{\varkappa m p_z}(\mathbf{r})$ is given by Eq. (3.8).

Regarding the final (bound) state of the electron, we will take the $1s$ ground state $\psi_{1,0,0}(\mathbf{r})$ of the ion as characterized by Eq. (3.14). We must note here that the wave function $\psi_{1,0,0}(\mathbf{r})$ in its current form represents a K-shell electron that is bound to a nucleus located at the center of the incoming electron beam. Such a description of the (bound) electron state disagrees, however, with the properties of the ion beam as specified in Sec. 6.3.1; that is, the ion beam possesses some spatial extension (as given by the Gaussian distribution (6.16)) and, hence, there are ions that are located off-axis, i.e. outside the center of the electron beam. To resolve this problem, let us focus for the moment on one ion of the ion beam and denote its transverse position with respect to the beam center as $\mathbf{b}_\perp$. We can incorporate the position $\mathbf{b}_\perp$ into the bound state of the electron, if we translate the wave function $\psi_{1,0,0}(\mathbf{r})$ by the vector $\mathbf{b}_\perp$ out of the center of the electron beam: $\psi_{1,0,0}(\mathbf{r}) \to \psi_{1,0,0}(\mathbf{r} - \mathbf{b}_\perp)$. Before we turn back to the description of the ion beam as a whole, let us further discuss the RR process of this *individual* ion and therefore let us take as the final (bound) wave function $\psi_f(\mathbf{r}) = \psi_{1,0,0}(\mathbf{r} - \mathbf{b}_\perp)$.

By using the initial and final electron wave functions as presented above, we may write the transition amplitudes as

$$M^{\mathrm{tw}}_{fi}(\mathbf{k},\lambda) \equiv M^{\mathrm{tw}}_{\varkappa m p_z \mathbf{b}_\perp}(\mathbf{k},\lambda) = \int \psi^*_{1,0,0}(\mathbf{r} - \mathbf{b}_\perp)\, \mathrm{e}^{-\mathrm{i}\mathbf{k}\cdot\mathbf{r}}\, (\mathbf{e}^*_{\mathbf{k}\lambda} \cdot \widehat{\mathbf{p}})\, \psi^{\mathrm{tw}}_{\varkappa m p_z}(\mathbf{r})\, \mathrm{d}^3\mathbf{r} \quad (6.18)$$

for the RR process of a single ion at a position $\mathbf{b}_\perp$ with respect to the electron center. Inserting the plane wave expansion (3.10) of the twisted electron wave function into Eq. (6.18) and integrating by parts, we obtain

$$M^{\mathrm{tw}}_{\varkappa m p_z \mathbf{b}_\perp}(\mathbf{k},\lambda) = \int \mathrm{e}^{\mathrm{i}\mathbf{b}_\perp\cdot(\mathbf{p}-\mathbf{k})}\, a_{\varkappa m p_z}(\mathbf{p})\, M^{\mathrm{pl}}_{\mathbf{p}}(\mathbf{k},\lambda)\, \mathrm{d}^3\mathbf{p}. \quad (6.19)$$

This equation demonstrates that the matrix elements for the capture of twisted electrons can be expressed as an integral over the amplitudes for the plane wave recombination (times some prefactor). To obtain the spin density matrix, we insert the amplitudes (6.19) into (6.5):

$$\langle \mathbf{k}\lambda | \widehat{\rho}^{\mathrm{tw}}_\gamma(\mathbf{b}_\perp) | \mathbf{k}\lambda' \rangle = M^{\mathrm{tw},*}_{\varkappa m p_z \mathbf{b}_\perp}(\mathbf{k},\lambda)\, M^{\mathrm{tw}}_{\varkappa m p_z \mathbf{b}_\perp}(\mathbf{k},\lambda'). \quad (6.20)$$

So far, we have discussed how the RR process can be described if an electron from the Bessel beam is captured by one particular ion placed at a transverse position $\mathbf{b}_\perp$. To describe the RR process for the whole beam, we have to average the photon-spin density matrix (6.20) over the spatial distribution $f(\mathbf{b}_\perp)$ of the ion beam so that

$$\begin{aligned}\langle \mathbf{k}\,\lambda|\widehat{\rho}_\gamma^{\rm tw}|\mathbf{k}\lambda'\rangle &= \int f(\mathbf{b}_\perp)\;\langle \mathbf{k}\lambda|\widehat{\rho}_\gamma^{\rm tw}(\mathbf{b}_\perp)|\mathbf{k}\lambda'\rangle\;\mathrm{d}^2\mathbf{b}_\perp \\ &= \int f(\mathbf{b}_\perp)\,M^{\rm tw,*}_{\varkappa m p_z \mathbf{b}_\perp}(\mathbf{k},\lambda)\,M^{\rm tw}_{\varkappa m p_z \mathbf{b}_\perp}(\mathbf{k},\lambda')\,\mathrm{d}^2\mathbf{b}_\perp .\end{aligned} \tag{6.21}$$

Using the explicit form (6.16) of $f(\mathbf{b}_\perp)$ and (6.19) of $M^{\rm tw}_{\varkappa m p_z \mathbf{b}_\perp}(\mathbf{k},\lambda)$, we can perform (after a lengthy calculation shown in Appendix D) the $\mathbf{b}_\perp$-integration in Eq. (6.21):

$$\begin{aligned}\langle \mathbf{k}\lambda|\,\widehat{\rho}_\gamma^{\rm tw}\,|\mathbf{k}\lambda'\rangle = \int &\exp\left[-2\varkappa^2\sigma_b^2\sin^2\left(\frac{\varphi_p-\varphi_p'}{2}\right)\right] \\ &\times a^*_{\varkappa m}(\mathbf{p}_\perp)\,a_{\varkappa m}(\mathbf{p}'_\perp)\,M^{\rm pl,*}_{\mathbf{p}}(\mathbf{k},\lambda)\,M^{\rm pl}_{\mathbf{p}'}(\mathbf{k},\lambda')\,\mathrm{d}^2\mathbf{p}_\perp \mathrm{d}^2\mathbf{p}'_\perp\,,\end{aligned} \tag{6.22}$$

where $a_{\varkappa m}(\mathbf{p}_\perp)$ is given by Eq. (2.76). We can evaluate Eq. (6.22) further, if we assume that the width of the ion beam σ_b is much larger than the *characteristic size* $\sigma_\varkappa$ of the twisted electron beam. What do we understand here by the characteristic size $\sigma_\varkappa$ of the twisted electron beam? As discussed in Sec. 3.1.2, the transverse shape of a Bessel beam of electrons consists of concentric rings around the beam center with high and low electron concentrations. The characteristic size of the twisted beam is then given by the radius of the first ring—the ring with the largest electron concentration. This radius, moreover, is approximately given by the ratio $m/\varkappa$ of the topological charge m and the transverse momentum $\varkappa$ of the electron beam. Altogether, it follows that the characteristic size of the electron beam is (approximately) given as $\sigma_\varkappa \approx m/\varkappa$.

If the width σ_b of the ion beam is now much larger then the characteristic size $\sigma_\varkappa$ of the electron beam, i.e. $m/\varkappa \ll \sigma_b$, then the exponential in Eq. (6.22) acts as a delta distribution (up to some factor denoted in the following by c):

$$\exp\left[-2\varkappa^2\sigma_b^2\sin^2\left(\frac{\varphi_p-\varphi_p'}{2}\right)\right] \to c\cdot\delta(\varphi_p-\varphi_p'). \tag{6.23}$$

By inserting this expression into Eq. (6.22) and by using the delta distribution $\delta(p_\perp-\varkappa)$ within the function $a_{\varkappa m}(\mathbf{p}_\perp)$, we can perform nearly all integrations for the photon-spin density matrix and are left with a single integration over the angle φ_p:

$$\langle \mathbf{k}\lambda|\,\widehat{\rho}_\gamma^{\rm tw}\,|\mathbf{k}\lambda'\rangle \propto \int M^{\rm pl,*}_{\mathbf{p}}(\mathbf{k},\lambda)\,M^{\rm pl}_{\mathbf{p}}(\mathbf{k},\lambda')\,\mathrm{d}\varphi_p. \tag{6.24}$$

The integration over the angle φ_p can be performed by means of standard integration techniques (shown in Appendix E), so that we finally obtain

$$\boxed{\langle \mathbf{k}\lambda |\, \widehat{\rho}_\gamma^{\,\mathrm{tw}}\, | \mathbf{k}\lambda' \rangle \propto A(\mathbf{k}) + \lambda\lambda' B(\mathbf{k})\,.} \tag{6.25}$$

As seen from Eq. (6.25), a sum of two functions, $A(\mathbf{k})$ and $B(\mathbf{k})$, characterize the photon-spin density matrix, both independent of the helicity λ. These functions are expressed solely by means of kinematic parameters such as the wave vector $\mathbf{k}$ of the emitted photon as well as the absolute momentum $p = \sqrt{\varkappa^2 + p_z^2}$ and opening angle $\theta_p = \arctan(\varkappa/p_z)$ of the incoming twisted electron beam:

$$A(\mathbf{k}) = \frac{1}{4v^4(1-u^2)^{7/2}} \left(1-u^2\right) \sin^2\theta_p, \tag{6.26}$$

$$\begin{aligned} B(\mathbf{k}) = \frac{1}{8v^4(1-u^2)^{7/2}} \Big[& 2\left(2+3u^2\right) \sin^2\theta_k \cos^2\theta_p - \left(4u+u^3\right) \sin 2\theta_k \sin 2\theta_p \\ & + 2\left(1+4u^2\right) \cos^2\theta_k \sin^2\theta_p \Big]\,, \end{aligned} \tag{6.27}$$

where we used the notations

$$\begin{aligned} u &= \frac{2pk}{v} \sin\theta_p \sin\theta_k,\ 0 \le u < 1, \\ v &= p^2 + k^2 + Z^2 - 2pk\cos\theta_p \cos\theta_k,\ 0 < v\,. \end{aligned} \tag{6.28}$$

Eqs. (6.25)–(6.28) provide the general description of the photon-spin density matrix for the RR process between a twisted electron beam and a *macroscopic* ion beam with a Gaussian density distribution. In the next section, we will use the photon density matrix in order to describe the angular distribution as well as the Stokes parameters of the recombination photons.

6.3.3. Angular Distribution and Polarization of Recombination Photons

Expressions (6.25)–(6.28) completely determine the photon density matrix for the K-shell RR of twisted electrons with (initially) bare ions. Using these expressions together with Eqs. (6.7)–(6.10) allows us to obtain the (angular and polarization) properties of the emitted photons in such a process. For example, by employing Eq. (6.7), we may write the photon angular distribution as:

$$\boxed{W(\mathbf{k}) = \mathcal{N}^{\mathrm{tw}}\big(A(\mathbf{k}) + B(\mathbf{k})\big).} \tag{6.29}$$

As seen from Eq. (6.29), the angular distribution of the RR photons is simply given as the sum of the functions $A(\mathbf{k})$ and $B(\mathbf{k})$, which we found in Sec. 6.3.2 while deriving the photon-spin density-matrix. Furthermore, we can choose the normalization constant $\mathcal{N}^{\mathrm{tw}}$ in Eq. (6.29) such that the angular distribution (6.29) is normalized as

$$\int W(\mathbf{k})\,\mathrm{d}\Omega_k = 4\pi. \tag{6.30}$$

After employing standard integration techniques [108], it follows from Eq. (6.30) that the normalization constant is of the form

$$\mathcal{N}^{\mathrm{tw}} = 3\left[(p^2-k^2)^2 + 2\,Z^2(p^2+k^2) + Z^4\right]^2. \tag{6.31}$$

The Stokes parameters, moreover, can be obtained from the density matrix (6.25) with the help of Eqs. (6.8)–(6.10) as

$$\boxed{P_1 = \frac{B(\mathbf{k}) - A(\mathbf{k})}{A(\mathbf{k}) + B(\mathbf{k})}, \quad P_2 = 0, \quad P_3 = 0.} \tag{6.32}$$

As can be seen from this expression, only the first Stokes parameter is non-zero and can be expressed as a simple fraction of the functions $A(\mathbf{k})$ and $B(\mathbf{k})$.

Eqs. (6.29) and (6.32) describe the emission pattern and the polarization state of photons emitted in the K-shell RR of twisted electrons in the most general case. These expressions are valid for arbitrary values of the transverse and longitudinal momentum $\varkappa$ and p_z of the electron beam. In particular, they are applicable not only for *paraxial* Bessel beams as characterized by small ratios of the transverse and longitudinal momenta, $\varkappa/p_z \ll 1$, but also for *non-paraxial* beams. In the next section, however, let us first discuss how these expressions can be simplified if one restricts them to the (often used) paraxial regime.

6.3.4. Angular Distribution and Polarization of Recombination Photons: Paraxial Regime

Most studies that have been performed on twisted electrons so far considered the *paraxial* beam regime (cf. Refs. [45, 47, 48, 51, 52]) as characterized by small opening angles $\theta_p = \arctan(\varkappa/p_z)$ of the beam's momentum cone (see Fig. 2.2). Let us therefore investigate how the angular distribution (6.29) as well as the Stokes parameters (6.32) behave in such a regime. By turning to the paraxial regime, $\theta_p \ll 1$, we may approximate the functions $A(\mathbf{k})$ and $B(\mathbf{k})$ that appear in the photon-spin density matrix (6.25) as

$$A(\mathbf{k}) = \frac{1}{4v^4} \sin^2\theta_p, \tag{6.33}$$

$$B(\mathbf{k}) = \frac{1}{4v^4} \big(2 \sin^2\theta_k \cos^2\theta_p + \cos^2\theta_k \sin^2\theta_p\big), \tag{6.34}$$

with

$$v = p^2 + k^2 + Z^2 - 2pk\cos\theta_k. \tag{6.35}$$

By inserting these expressions into Eqs. (6.29) and (6.32) for the angular distribution and the first Stokes parameter, respectively, we may write

$$W(\mathbf{k}) \simeq \frac{\mathcal{N}^{\rm tw}}{2} \frac{\sin^2\theta_k + \sin^2\theta_p\, P_2(\cos\theta_k)}{\left(p^2 + k^2 + Z^2 - 2p\,k\cos\theta_k\right)^4}\,, \tag{6.36}$$

$$P_1 \simeq 1 - \frac{\sin^2\theta_p}{\sin^2\theta_k + \sin^2\theta_p\, P_2(\cos\theta_k)}, \tag{6.37}$$

where $P_2(\cos\theta_k) = (3\cos^2\theta_k - 1)/2$ denotes the second-order Legendre polynomial. As seen from Eqs. (6.36)–(6.37), both, the angular distribution and the first Stokes parameter, can be expressed as a sum of two terms. The first term in these expressions describes exactly the dependency that we have found for the RR process with plane wave electrons (cf. Eqs. (6.14)–(6.15)) This is expected, since Bessel beams start to "behave" like plane waves if the opening angle θ_p tends to zero. The second term in both equations, which depends on the opening angle θ_p of the beam, arises purely due to the "twisted nature" of the electron wave. Therefore, this term disappears if we turn to $\theta_p \to 0$, that is, only the plane wave behaviour

$$W(\mathbf{k}) \simeq \frac{\mathcal{N}^{\rm tw}}{2} \frac{\sin^2\theta_k}{\left(p^2 + k^2 + Z^2 - 2p\,k\cos\theta_k\right)^4}\,, \tag{6.38}$$

$$P_1 \simeq 1, \tag{6.39}$$

remains for $\theta_p = 0$. We conclude that simple and intuitive expressions (6.36)–(6.37) describe the properties of the emitted photons for the RR process with a paraxial twisted electron beam.

6.3.5. Radiative Recombination by Twisted Electrons: Coherent Superposition of Two Electron Beams

In the previous sections, we discussed the angular distribution and the polarization of photons that are emitted when a twisted electron is captured to the K-shell of

an (initially) bare ion. These twisted electrons were chosen to be in a pure state with a well-defined longitudinal OAM $\hbar m$. As seen from the density matrix (6.21), however, in this case the properties of the emitted photons are only dependent on the transverse momentum $\varkappa$ of the beam via the opening angle θ_p and are insensitive to the topological charge m. This insensitivity can be overcome if we coherently superimpose two twisted electron beams:

$$\psi_i^{\mathrm{tw}}(\mathbf{r}) = c_1\, \psi^{\mathrm{tw}}_{\varkappa m_1 p_z}(\mathbf{r}) + c_2\, \mathrm{e}^{\mathrm{i}\zeta}\, \psi^{\mathrm{tw}}_{\varkappa m_2 p_z}(\mathbf{r})\,. \tag{6.40}$$

Here m_1 and m_2 denote the OAM along the mutual propagation axis of the beams, whereas ζ is the relative phase between the beams. The (real) weights c_1 and c_2, moreover, fulfill the relation $\sqrt{c_1^2 + c_2^2} = 1$. Such states can be experimentally produced by sending a coherent electron beam onto specially designed diffraction gratings, a method that is outlined in Ref. [57].

Imagine now the same "electron-ion collision scenario" as in the previous sections (cf. Sec. 6.3.1), but instead of an incoming twisted beam with a single topological charge we use a superposition of beams as represented by Eq. (6.40). If we would like to describe the angular distribution and Stokes parameters for this case, we would need to re-derive the photon-spin density matrix (6.4) taken for an initial electron state of the form (6.40). Similar as for an electron beam in a pure OAM state, we can perform the necessary calculations to obtain the corresponding density matrix by inserting the (initial) wave function (6.40) into the transition amplitudes (6.18) and by using these amplitudes together with Eq. (6.24). This eventually leads us to the density matrix in the form

$$\boxed{\begin{aligned}\langle \mathbf{k}\lambda|\, \widehat{\rho}_\gamma^{\mathrm{tw}}\, |\mathbf{k}\lambda'\rangle \propto \int & M^{\mathrm{pl},*}_{\mathbf{p}}(\mathbf{k},\lambda)\, M^{\mathrm{pl}}_{\mathbf{p}}(\mathbf{k},\lambda') \\ & \times \left\{1 + 2|c_1 c_2| \cos\left[\Delta m(\varphi_p - \pi/2) + \zeta\right]\right\} \mathrm{d}\varphi_p,\end{aligned}} \tag{6.41}$$

where $\Delta m = m_2 - m_1$ is the difference between the topological charges of the superimposed beams. As seen from Eq. (6.41), the photon-spin density matrix for a RR process with a superposition of twisted electron beams can be expressed—as for a single beam with well-defined m—in terms of the plane wave matrix elements $M^{\mathrm{pl}}_{\mathbf{p}}(\mathbf{k},\lambda)$. The first term in the bracket of Eq. (6.41) corresponds hereby to the result that has been obtained in the previous section for a single beam in a pure OAM state (cf. Eq. (6.24)). However, a second term proportional to $2|c_1 c_2| \cos\left[\Delta m(\varphi_p - \pi/2) + \zeta\right]$ arises that represents an interference between the two beams that have been superimposed within the wave function (6.40). This interference term depends on the difference $\Delta m = m_2 - m_1$ of the topological charges of the pure beams, and also on their relative phase ζ. To evaluate the interference

beam parameter	first scenario	second scenario
beam energy E_{kin}	2 keV	2 keV
opening angle θ_p	45°	45°
longitudinal momentum p_z	8.57 a.u.	8.57 a.u.
transverse momentum $\varkappa$	8.57 a.u.	8.57 a.u.
relative phase ζ	0	0
weight factor c_1	$1/\sqrt{2}$	$1/\sqrt{2}$
weight factor c_2	$1/\sqrt{2}$	$1/\sqrt{2}$
longitudinal OAM m_1 of first beam	0	0
longitudinal OAM m_2 of second beam	± 1	± 2

Table 6.1. – Parameters of the superposition state (6.40) that will be used later in the analysis of the RR process.

term in Eq. (6.41), we rely on standard numerical integration methods as implemented in modern computer algebra systems. Using these methods, we are able to (numerically) obtain the photon-spin density matrix (6.41) for the RR process with a superposition of two twisted beams. With the help of Eqs. (6.7)–(6.10), these numerical results can then be utilized further to obtain the angular distribution and Stokes parameters of the emitted photons. However, to determine these quantities unambiguously, we must note that—in contrast to a twisted beam with a well-defined longitudinal OAM—an electron state of the form (6.41) possesses a transverse shape of its electron density that is *not* axially symmetric around the propagation axis. With respect to the RR process, it is therefore necessary to specify where around the propagation axis of the incoming electron beam we place the detector that registers the recombination photons (the polar angle of the detector position is still given with respect to the beam's propagation direction as described by Fig. 6.3). To define such an *axial* position of the photon detector, it is convenient to utilize the transverse structure of the superimposed beams. Since this structure depends strongly on the parameters of the superimposed beams such as the longitudinal OAM m_1 and m_2, we shall focus here only on those cases that we will analyze later on in Chapter 8.

In Chapter 8 we will examine the RR process for an electron beam of the form (6.40) that is described by either one of two parameter sets as given by the second or third column of Tab. 6.1, respectively. For both scenarios, the relative phase ζ between the superimposed beams has been set to zero, $\zeta = 0$, and the weight factors have been chosen as $c_1 = c_2 = 1/\sqrt{2}$ such that it is equally probable to find the first or the second beam within the superposition state (6.40).

In the following, we will discuss how we may define the (axial) detector position for the first scenario (cf. second column of Tab. 8.1), for which the OAM along the propagation direction is set to zero for the first beam, $m_1 = 0$, and to either

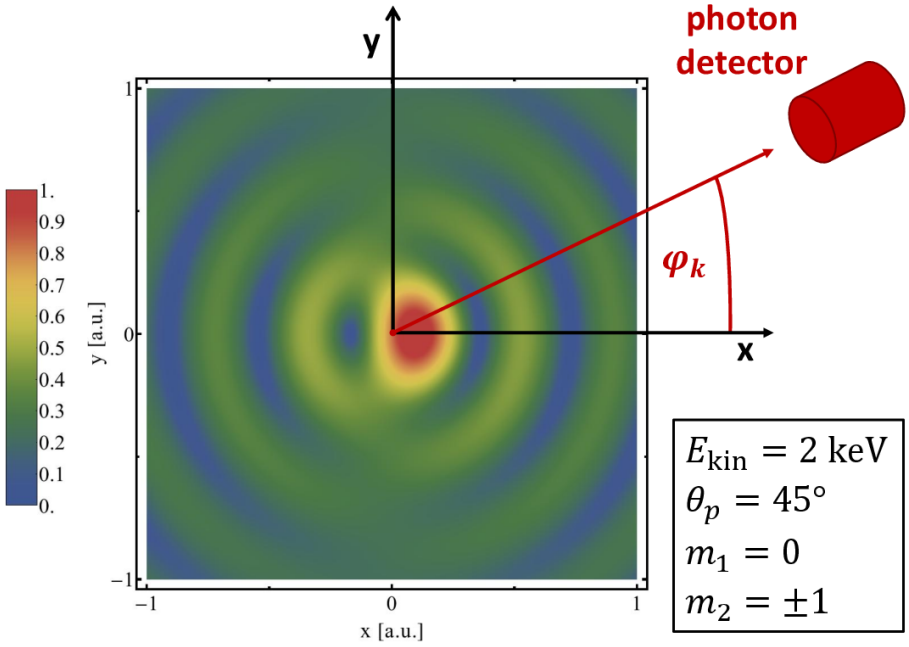

Figure 6.4. – Transverse shape of the electron density for an electron beam that resides in the superposition state (6.40) with parameters given by the second column of Tab. 6.1. With respect to the RR process, we observe the emitted photons under an azimuthal angle φ_k with respect to the "electron arm" of the density profile with a high electron concentration. The y-axis is defined such that it forms—together with the x-axis and the (propagation) z-axis—forms a right-handed coordinate system. Here the propagation axis of the electron beam points out of the page.

$m_2 = -1$ or $m_2 = +1$ for the second beam. For this scenario, we display in Fig. 6.4 the (time-independent) electron probability density as arising from the coherent superposition (6.40) of the two beams; this density is shown in the plane transverse to the propagation direction of the beams. As seen from the figure, the probability density possesses the same shape regardless of the topological charge, $m_2 = -1$ or $m_2 = +1$, of the second beam. For both cases, $m_2 = -1$ and $m_2 = +1$, this density possesses two strongly-aligned "arms"—one with a high and the other with a low electron concentration (right and left side of the figure). These "electron arms" allow us to specify the position of the photon detector in the plane transverse to the beam's propagation direction. In particular, let us define the x-axis of a coordinate system along the arm of the probability density that possesses the high electron concentration (cf. Fig. 6.4) and place the detector under an angle φ_k with respect to this axis. The y-axis, moreover, is chosen such that it forms—together with the x-axis and the propagation (z-)axis of the beam—a right-handed coordinate system.

Coming to the second scenario, we show in Fig. 6.5 the density profile of a beam with parameters as given by the third column of Tab. 6.1. The figure illustrates

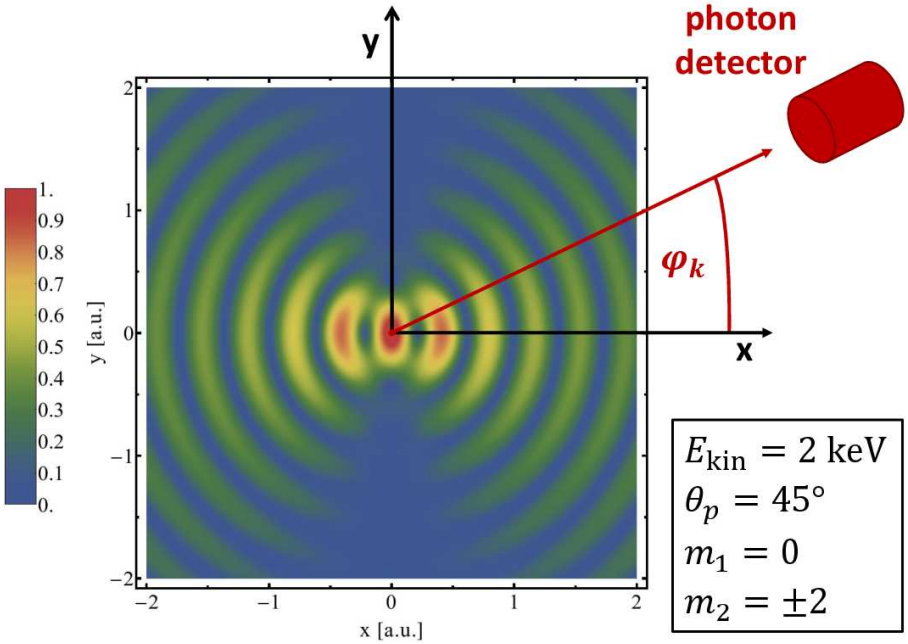

Figure 6.5. – Transverse shape of the electron density for an electron beam that resides in the superposition state (6.40) with parameters given by the third column of Tab. 6.1. With respect to the RR process, we observe the emitted photons under an azimuthal angle φ_k with respect to one of the "electron arms". The y-axis is defined such that it forms—together with the x-axis and the (propagation) z-axis—forms a right-handed coordinate system. Here the propagation axis of the electron beam points out of the page.

that the density profile has the same shape independently of the longitudinal OAM, $m_2 = +2$ or $m_2 = -2$ of the second beam. More specifically, such a profile consists of two similar "arms" in which the electron concentration alternates between high and low intensities. Again, these arms provide us with a convenient way to define the position of the photon detector. Let us take the x-axis along one of these arms and define the y-axis such that—together with the (propagation) z-axis—the coordinate system is right-handed (cf. Fig. 6.5). However, this choice is not unique, since we could also place the x-axis along the other arm (and define the y-axis accordingly to the right-handedness of the system). As we will see in Chapter 8, such an alternate choice will lead exactly to the same results and, hence, the definition from above is sufficient to characterize the emission process of the RR photons for this scenario.

Having discussed now both, the theoretical treatment of the atomic ionization with twisted photons (previous chapter) as well as the radiative recombination with twisted electrons (this chapter), we are finally ready to apply these theoretical formalisms to a variety of different scenarios. In the next chapter, let us begin now with such an analysis for the atomic photoionization process with twisted photons.

7. Atomic Ionization by Twisted Photons: Results and Discussion

In Chapter 5 we developed a theoretical formalism to investigate the ionization of hydrogen-like ions by twisted (Bessel) photons. This formalism is most general and can be applied to study the ionization process of arbitrary (but still non-relativistic) hydrogenic bound states. In the following, we will employ the developed formalism to analyze the ionization process with twisted Bessel beams of two different bound states of a hydrogen atom. We will focus in particular on the ionization of a hydrogen atom that initially resides in either (i) the $1s$ ground state (K-shell) or (ii) the $2p_y$-state. For both states, we will pay special attention to the angular distribution of the emitted electrons and study in detail how this distribution depends on the position of the hydrogen atom within the wave front of the incoming twisted light beam.

Here we are especially interested in the electron distribution perpendicular to the direction of the incoming photon beam, i.e. the *axial* or *azimuthal* angular distribution. Such an azimuthal distribution will strongly reflect the "azimuthal structure" of the incoming photon beam. Since the *azimuthal* phase structure is closely connected to the (longitudinal) TAM of the photon beam (see Eq. (2.82)), effects of the (longitudinal) TAM on the angular distribution can be clearly seen in the azimuthal direction as we will show in the next sections. For reasons of completeness, we will also append a section on the angular pattern of the photoelectrons as a function of the *polar* emission angle with respect to the propagation axis of the incoming beam.

Let us begin now to analyze the electron angular distributions for the K-shell ionization of a hydrogen atom by twisted (Bessel) light beams. We must note here that the following sections will be similar in structure to the corresponding sections in our published manuscript [68].

7.1. Ionization of Hydrogen $1s$-State by Twisted Photons

Here we will discuss the ionization process of the $1s$ ground state of a hydrogen atom by a twisted photon beam. The geometrical setup of such an ionization process has been laid out in Sec. 5.2 (cf. Fig. 5.2). Before we can start our analysis, however, we need to specify the properties of the incoming photon beam such as transverse and

beam parameter	first scenario	second scenario	third scenario
photon energy E_γ	100 eV	100 eV	100 eV
longitudinal momentum k_z	$2.68 \cdot 10^{-2}$ a.u.	$2.67 \cdot 10^{-2}$ a.u.	$1.89 \cdot 10^{-2}$ a.u.
transverse momentum $\varkappa$	$2.68 \cdot 10^{-4}$ a.u.	$2.67 \cdot 10^{-3}$ a.u.	$1.89 \cdot 10^{-2}$ a.u.
opening angle θ_k	0.57°	5.71°	45°
ratio $s = \varkappa/k_z$	0.01	0.1	1
helicity λ	$+1$	$+1$	$+1$
z–component of TAM m_γ	$+3$	$+3$	$+3$

Table 7.1. – Parameters of the twisted (Bessel) light beam used in the calculations.

longitudinal momentum $\varkappa$ and k_z as well as helicity λ and longitudinal TAM m_γ. In our calculations, we will characterize the beam by either of three different sets of parameters as summarized in Tab. 7.1. For each set, the energy of the incoming photon beam has been chosen as 100 eV, an energy which lies well above the ionization threshold of the $1s$ ground state so that the Born approximation used in our formalism is valid (see Chapter 5). We also note that twisted photon beams in such an energy range have recently been produced at the synchrotron light source BESSY II [17].

The first set of parameters (second column in Tab. 7.1) has been chosen such that the transverse momentum $\varkappa$ of the beam is much smaller than the longitudinal momentum k_z; the ratio $s = \varkappa/k_z$ of the momenta is taken as $s = 0.01$. Such a small ratio of the transverse and longitudinal momenta translates directly to a small opening angle $\theta_k = \arctan(\varkappa/k_z) = 0.57^\circ$ of the photon beam and, hence, the first scenario corresponds to the *paraxial* beam regime (see Sec. 2.3.4). For the latter two scenarios (third and fourth column of Tab. 7.1), however, the ratios s of the transverse and longitudinal momenta have been chosen as $s = 0.1$ and $s = 1$, respectively, which correspond to beams within the weakly and strongly *non-paraxial* regime, respectively.

Let us discuss now the K-shell ionization for the *paraxial* beam scenario as given by the second column in Tab. 7.1. We display in Fig. 7.1 the angular distribution of the electrons that are emitted in the ionization process with such a paraxial beam as a function of the azimuthal angle φ_p. Computations have been performed for impact parameters in the range $0\,\text{a.u.} \leq b \leq 100\,\text{a.u.}$ as well as for three polar angles $\theta_p = 45^\circ$ (left panel), $\theta_p = 60^\circ$ (middle panel), and $\theta_p = 90^\circ$ (right panel). We compare our results to the ones for the ionization process by plane wave photons with the same energy $E_\gamma = 100\,\text{eV}$ and helicity $\lambda = +1$. All distributions are normalized as

$$\int W^{\text{tw, pl}}(\theta_p, \varphi_p)\, \mathrm{d}\Omega_p = 4\pi\,, \tag{7.1}$$

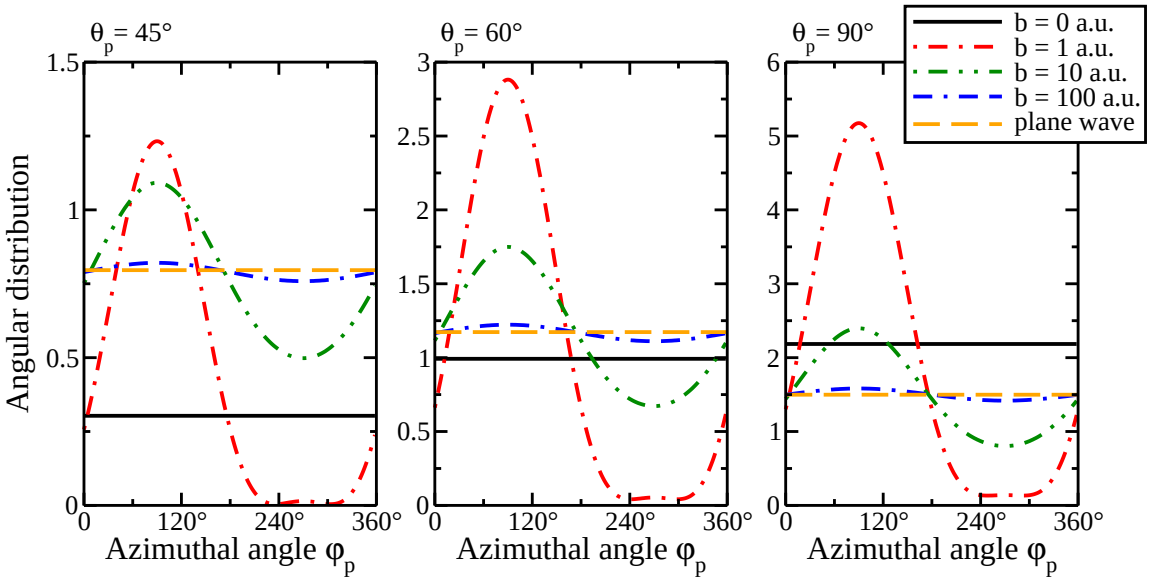

Figure 7.1. – Angular distribution of electrons emitted in K-shell ionization of a neutral hydrogen atom by twisted light. Results are presented for different impact parameters b, that characterize the position of the atom in the wavefront (cf. Fig. 5.2), and three polar angles $\theta_p = 45°$ (left panel), $\theta_p = 60°$ (middle panel), and $\theta_p = 90°$ (right panel) of the (continuum) electron. For comparison, the emission pattern for incoming plane wave photons with helicity $\lambda = +1$ is depicted by the yellow dashed line.

which allows us to study how the *shape* of the electron emission pattern is changed for different impact parameters.

As seen from all panels in Fig. 7.1, the shape of the azimuthal angular distribution of the photoelectrons varies significantly if we change the impact parameter b between the incoming twisted beam and the hydrogen atom. If the atom sits in the center of the beam's wavefront ($b = 0$ a.u.), the electron distribution is isotropic around the beam (z-)axis. This is expected since the initial system composed of the *centered* hydrogen atom in the ground state "plus" twisted photon beam is axial symmetric around the beam axis and, hence, all the photoelectrons are emitted with equal probability into an azimuthal direction φ_p. When we depart from such a symmetric case and move the atom out of the beam center, the emission pattern of the electrons exhibits a pronounced shape as can be seen, for example, for the impact parameters $b = 1$ a.u. or $b = 10$ a.u. in all panels of Fig. 7.1. However, as the impact parameter approaches $b = 100$ a.u., the angular distribution of the photoelectrons becomes nearly isotropic around the beam axis and begins to look like the distribution for the ionization process with plane wave photons.

How can we understand that twisted waves cause a pronounced emission pattern of the photoelectrons if the atom is placed near the beam axis but behave like plane

waves with regard to the ionization process if the impact parameter is (relatively) large? Two properties of the incoming light beam can affect the emission pattern of the electrons: (i) the phase structure and (ii) the intensity profile. The intensity profile of a paraxial Bessel beam with parameters as used here (cf. second column of Tab. 7.1) has been already depicted in Figs. 2.4–2.5. As seen from these figures, the intensity profile consists of concentric low- and high-intensity rings which alternate on a length scale of 10^4 a.u. In order that the hydrogen atom may "feel" these variations, this length scale has to be comparable to the extension of the electron cloud of the atomic bound state. For the $1s$ ground state of a hydrogen atom, however, the "size" of the electron cloud is of the order of 1 a.u. Thus, regardless of the atomic position within the beam's wavefront, the oscillations in the intensity profile of a paraxial light beam are not "seen" by the K-shell electron.

The phase structure of a *paraxial* Bessel beam within a plane transverse to the propagation direction is given by the azimuthal phase factor $\exp[\mathrm{i}(m_\gamma - \lambda)\varphi_r]$ as seen, for example, from Eq. (2.84). With respect to the ionization process, this phase factor changes considerably over the extension of the atom if it is placed near to the photon beam axis. Such a strong variation of the *azimuthal* phase can significantly affect the emission process of the photoelectrons in the azimuthal direction and, hence, is responsible for the pronounced shape of the electron angular distribution for (relatively) small impact parameters b. Far away from the beam center, in contrast, an atom "sees" a phase factor that changes only very slowly over the size of the (bound-state) electronic cloud. It follows, therefore, that in the large impact parameter regime the phase as well as the intensity are seen as constant by the atom. Constant phase and intensity are characteristic for *plane electromagnetic waves* and thus the emission pattern for large impact parameters $b > 100$ a.u. resembles that of the ionization with plane waves as can be seen from the three panels in Fig. 7.1. In conclusion, the ionization process of hydrogen atoms by electromagnetic Bessel beams can be intuitively understood by considering the intensity and phase profile of such beams.

7.1.1. Angular Distribution of Photoelectrons: Dependence on longitudinal TAM

So far, we have considered the ionization process of the hydrogen ground state by a twisted beam with a fixed longitudinal TAM $m_\gamma = +3$. In Fig. 7.2 we display the angular distribution for photons emitted in the K-shell photoionization of a hydrogen atom for the same beam parameters as above (see second column in Tab. 7.1) but for five different values of the longitudinal TAM, $m_\gamma = 1, \ldots, 5$. Results are shown as a function of the azimuthal angle φ_p and for a polar angle $\theta_p = 45°$; the separate panels of Fig. 7.2 correspond to different impact parameters of the atom with respect to the

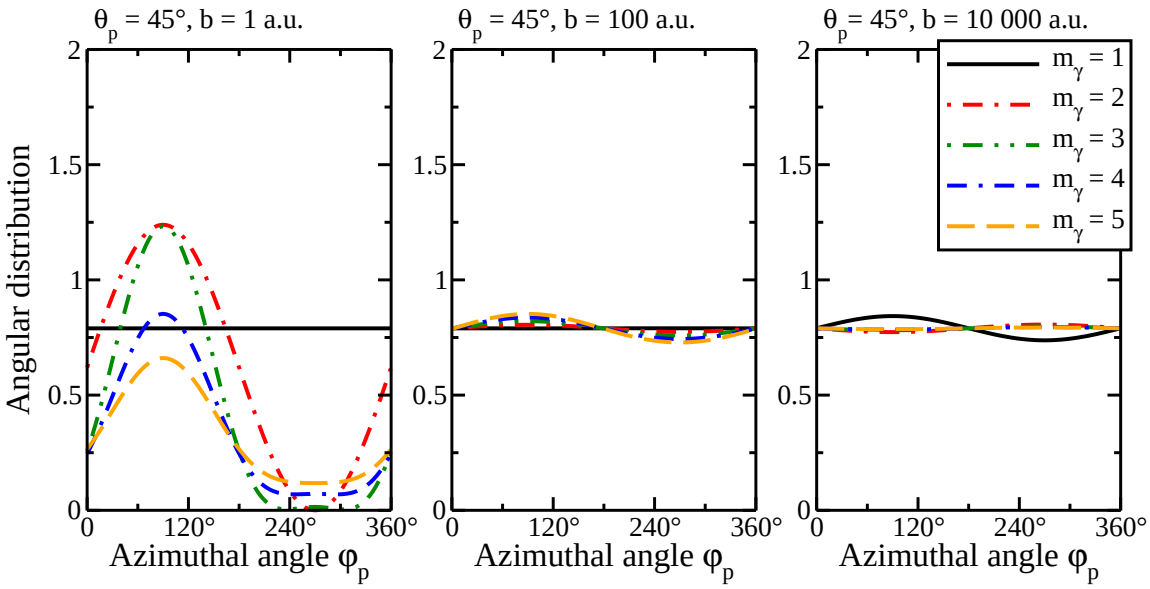

Figure 7.2. – Same as in Fig. 7.1 but for different values of the longitudinal TAM m_γ of the twisted photon beam.

beam center: $b = 1$ a.u. (left panel), $b = 100$ a.u. (middle panel), and $b = 10\,000$ a.u. (right panel).

The left panel of Fig. 7.2 illustrates that if the impact parameter is small ($b \approx 1$ a.u.), the emission pattern of the photoelectrons is significantly affected by changing the longitudinal TAM m_γ of the twisted light beam. For larger impact parameters $b \geq 100$ a.u. (middle and right panel of the figure), however, a variation of the beam's longitudinal TAM m_γ influences the distribution of the emitted electrons only slightly. Such a behaviour is expected and can be explained with the same arguments as in the previous section; that is, next to the beam center the azimuthal phase structure of the twisted light beam varies considerably and may strongly affect the (azimuthal) electron distribution. Therefore, if we place the atom near to the beam center, the emission pattern of the photoelectrons can be influenced significantly by changing the phase structure or equivalently by changing the longitudinal TAM m_γ of the light beam. Far away from the center, however, the beam's azimuthal phase varies weakly over the extension of the atom and therefore a change in m_γ has only a neglectable effect on the angular distribution of the emitted electrons.

Finally, we note that in particular instances the emission pattern of the photoelectrons may be (slightly) non-constant although the atom is positioned far away from the beam axis, a behaviour that can be seen, for example, in the right panel of Fig. 7.2 for the parameters $m_\gamma = 1$ and $b = 10\,000$ a.u. Such a behaviour occurs when the atom is located in or next to one of the intensity minima of the incoming light beam (cf. Fig. 2.4). In this case, since the intensity is vanishing inside the minima of

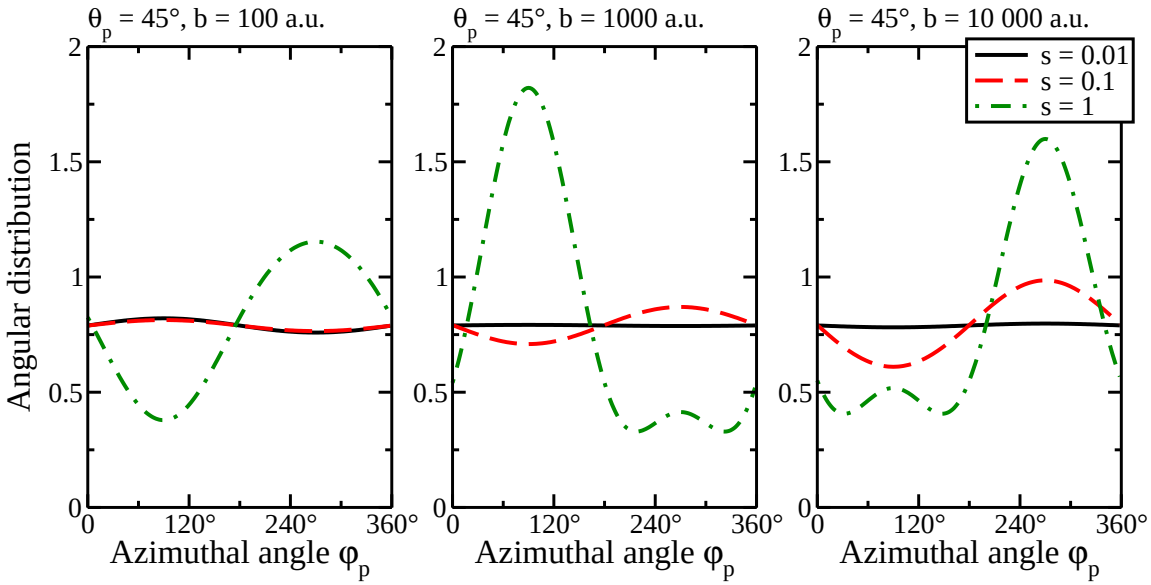

Figure 7.3. – Same as in Fig. 7.1 but for different ratios $s = \varkappa/k_z$ of the transverse and longitudinal momentum.

a (paraxial) Bessel beam, the bound electron has a chance to "feel" the slope of the intensity profile, which then leads to an asymmetric (with respect to the azimuthal angle φ_p) emission pattern.

7.1.2. Angular Distribution of Photoelectrons: Non-Paraxial Beam Regime

In the previous sections, we discussed the angular distributions of electrons emitted in the (K-shell) photoeffect of a hydrogen atom by a twisted light beam whose transverse momentum $\varkappa$ was much smaller than its longitudinal one k_z. Such a choice of the transverse and longitudinal momentum belonged to the so-called *paraxial* beam regime. To study how the *azimuthal* electron distribution behaves for beam parameters that correspond to the *non-paraxial* regime, we have also performed detailed calculations for twisted light beams with much larger ratios $s = \varkappa/k_z$ of the transverse and longitudinal momentum as given by the third and fourth column of Tab. 7.1. In Fig. 7.3 we display the emission patterns of the photoelectrons that are emitted in the ionization process with such non-paraxial beams and compare them to the angular distributions in the paraxial regime (as described by the second column of Tab. 7.1). Calculations have been performed for the (polar) emission angle $\theta_p = 45°$ and for three different impact parameters: $b = 100$ a.u. (left panel), $b = 1000$ a.u. (middle panel) and $b = 10\,000$ a.u. (right panel).

As seen from Fig. 7.3, in the highly non-paraxial regime where $s = 1$, the angular distribution of the photoelectrons exhibits a pronounced structure not only next to (left panel) but also far away from the beam axis (middle and right panel). A similar behaviour (but not as strong as before) is also present for the ionization process with Bessel beams whose ratio of transverse and longitudinal momentum amounts to $s = 0.1$; such beams correspond neither completely to the paraxial nor the non-paraxial regime but rather to an intermediate regime that lies at the border of these two.

How can we explain the pronounced (azimuthal) angular distribution of the photoelectrons in the intermediate as well as the non-paraxial beam regime? In turning to these regimes, we increase the ratio $s = \varkappa/k_z$ of the transverse and longitudinal momentum and, as a consequence, we also increase the transverse momentum $\varkappa$ of the photon beam. Such a modification of the transverse momentum strongly affects the (transverse) intensity profile of the incoming twisted light beam (cf. Eqs. (2.94)–(2.95) and Fig. 2.5). More specifically, if the transverse momentum $\varkappa$ increases, the spatial distance between the adjacent high and low intensity rings that constitute this profile gets smaller or, in other words, the intensity oscillations occur on a much shorter length scale. Now with respect to the ionization process, at some point the beam's transverse momentum is large enough so that the length scale of these oscillations becomes comparable to the extension of the hydrogen atom; such a matching between the length scales of the atom and the beam starts already for ratios of $s = \varkappa/k_z = 0.1$ as associated with the intermediate beam regime but is most pronounced in the non-paraxial regime ($s = 1$). Finally, when these (atomic and beam) scales are of the same size, the bound-state electron can "feel" the intensity oscillations within the beam, an effect which may strongly influence the emission process of the electrons. As a conclusion, increasing the beam's transverse momentum $\varkappa$ and turning therefore to the non-paraxial regime may significantly alter the beam's intensity profile and thereby change the emission pattern of the photoelectrons.

7.1.3. Angular Distribution of Photoelectrons: Dependency on Polar Angle

In the above, we performed a detailed analysis of the K-shell ionization of neutral hydrogen atoms by twisted light beams; in this analysis we especially focused on the emission patterns of the photoelectrons *axially* around the beam axis. When the atom initially resides in the K-shell, such an axial distribution of the emitted electrons can only occur for the atomic ionization by twisted (Bessel) beams and is absent in the plane wave photoeffect. Therefore, the axial electron distribution provided detailed insights into the atomic photoeffect with twisted photons and, in particular, points out the differences to the ionization process with plane wave photons.

To complete our study of the K-shell ionization process by twisted photons, we will discuss in the following the emission pattern of the photoelectrons in dependence on the *polar* emission angle (with respect to the beam axis). Results will be obtained for both, the paraxial and the non-paraxial beam regime.

In Fig. 7.4 we display the angular distribution of electrons emitted in the ionization of hydrogen atoms by *paraxial* twisted light beams as a function of the polar angle θ_p. The parameters of such a paraxial beam are again given by the second column of Tab. 7.1. Results have been obtained for a range $0 \leq b \leq 100\,\text{a.u.}$ of impact parameters and for three azimuthal angles: $\varphi_p = 0$ (left panel), $\varphi_p = 45°$ (middle panel), and $\varphi_p = 90°$ (right panel). These results are compared, moreover, to the corresponding ones of the plane wave photoeffect.

The figure demonstrates that, regardless of the impact parameter b or the azimuthal angle φ_p, the polar distributions of the photoelectrons possess a pronounced but symmetric structure with respect to the forward and backward emission. For impact parameters $b \geq 100\,\text{a.u.}$, moreover, these emission patterns resemble the ones that are obtained for the ionization process with plane wave photons. We must note, nevertheless, that even if the atom is positioned closer than 100 a.u. to the beam axis, the "overall shape" of the polar distributions looks quite similar as for the plane wave photoeffect.

To explain the structure and behaviour of the electron angular distributions, we remark that the emission process of the photoelectrons in the polar direction is strongly affected by the longitudinal structure of the photon beam. As discussed in Sec. 2.3.4, such a longitudinal structure is characterized by the phase factor $\exp(\mathrm{i}k_z z)$ (cf. Eq. (2.84)) of the beam's vector potential. This phase factor has exactly the same form as for the vector potential of a plane wave light beam (see Eq. (2.2)) and, hence, with respect to the ionization process by twisted photons, the polar emission pattern must be of a similar structure as for the photoeffect with plane waves (see Fig. 7.4).

The longitudinal factor $\exp(\mathrm{i}k_z z)$ is not the only term that can influence the ionization process within the paraxial beam regime. If the atom is positioned next to the beam axis, the transverse phase factor $\exp(\mathrm{i}(m_\gamma - \lambda)\varphi_r)$ can considerably affect the emission process as we have seen, for example, in the previous sections for the axial angular distributions. Even though such a transverse phase factor is not "strong" enough in comparison to the longitudinal one to change the overall shape of the polar distribution of the photoelectrons, it can significantly modify the (overall) magnitude of the angular distribution for certain emission angles, as seen from Fig. 7.4. However, if the atom is placed far away from the beam axis, the influence of the phase factor $\exp(\mathrm{i}(m_\gamma - \lambda)\varphi_r)$ decreases so that only the longitudinal term $\exp(\mathrm{i}k_z z)$ plays a role. Then the polar emission pattern of the photoelectrons completely resembles the one for the photoeffect with plane waves.

Finally, we remark that, as for the axial angular distribution, the intensity oscillations within the transverse profile of the paraxial Bessel beam (see Figs. 2.4–2.5)

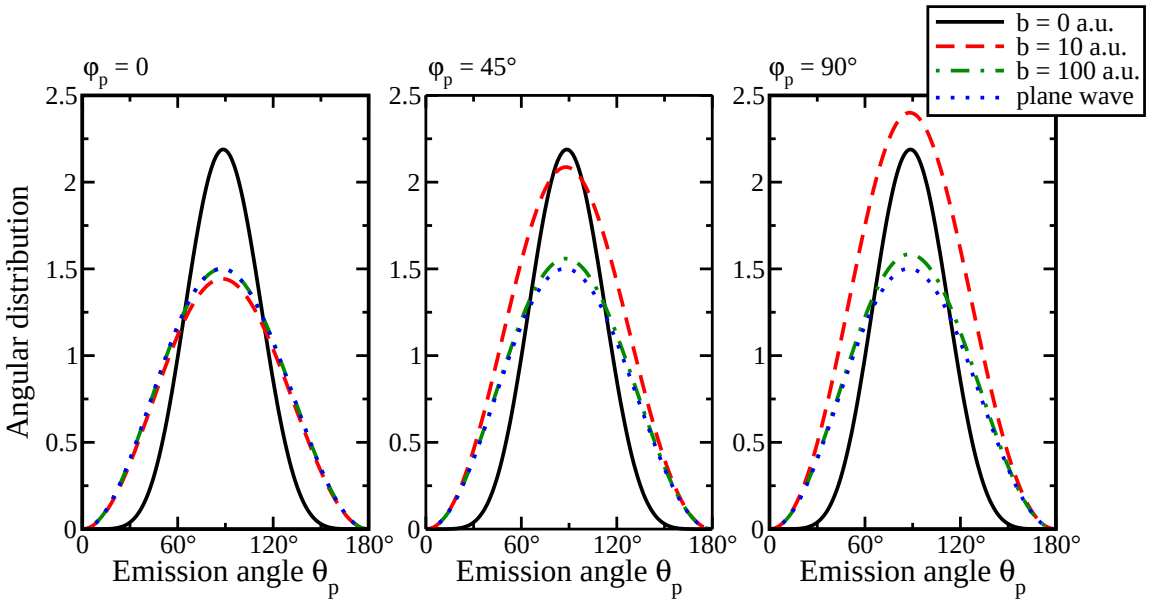

Figure 7.4. – Angular distribution of electrons emitted in K-shell ionization of a neutral hydrogen atom by twisted light as a function of the polar emission angle θ_p. Calculations have been performed within the paraxial regime for beam parameters as given by the second column of Tab. 7.1. Results are obtained for impact parameters $b = 0$ a.u. (black solid line), $b = 10$ a.u. (red dashed line), and $b = 100$ a.u. (green dashed-dotted line) and for three azimuthal angles: $\varphi_p = 0$ (left panel), $\varphi_p = 45°$ (middle panel), and $\varphi_p = 90°$ (right panel). The obtained results are compared, moreover, to the corresponding ones for the photoeffect with plane waves (blue dotted line).

do not affect the emission pattern of the photoelectrons, since the length scale of the oscillations is too large in comparison to the atomic size.

So far, we discussed the polar emission patterns of electrons that were emitted in the ionization process of a hydrogen atom by a *paraxial* Bessel beam. In Fig. 7.5 we depict the electron angular distributions as a function of the polar angle θ_p for the ionization process with *non-paraxial* light beams as described by the fourth column of Tab. 7.1. Results are again shown for different impact parameters b as well as the three azimuthal angles $\varphi_p = 0$ (left panel), $\varphi_p = 45°$ (middle panel), and $\varphi_p = 90°$ (right panel). As seen in all panels of Fig. 7.5, in the *non-paraxial* beam regime, the angular distribution of the photoelectrons varies significantly by changing the impact parameter b and a pronounced emission pattern can occur even if the atom is positioned far outside the beam center. Such pronounced emission patterns are again attributed to the intensity oscillations in the transverse profile of the Bessel light beam, since the "wave length" of these oscillations for a non-paraxial beam can be of the order of the atomic size so that they may significantly affect the emission

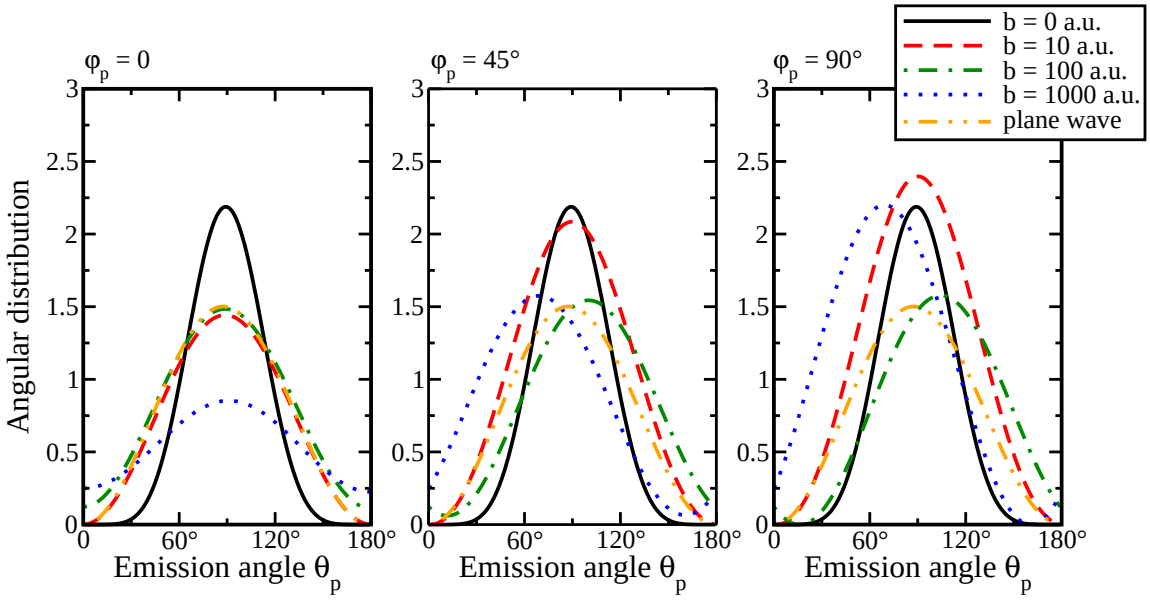

Figure 7.5. – Same as in Fig. 7.4 but for the non-paraxial beam regime as described by the fourth column of Tab. 7.1.

process. In contrast to the electron distributions for the paraxial beam regime, the electrons are now emitted asymmetrically with respect to the forward and backward direction. Such an asymmetry may come from a complex interplay between the longitudinal oscillations of the phase factor $\exp(\mathrm{i}k_z z)$ and the transverse oscillations of the intensity profile of the Bessel beam. The non-symmetric emission of the photoelectrons occurs, however, only if the atom is placed outside the beam center, whereas if it is positioned in the beam center the angular distribution reflects the polar symmetry of the initial atom "plus" beam system.

Let us finally conclude that the polar emission pattern of the electrons emitted in the K-shell ionization by *paraxial* as well as *non-paraxial* twisted photon beams may exhibit unique characteristics, which can be completely explained by the interplay between the different properties of the twisted light beam during the ionization process.

7.2. Ionization of Hydrogen $2p_y$-State by Twisted Photons

The $1s$ ground state of a hydrogen atom possesses an electronic probability density that is *spherically symmetric*. As a consequence, if an atom in such a symmetric state is ionized by a twisted light beam, an *asymmetric* (axial and polar) angular distribution is solely caused by the spatial displacement of the atom with respect to

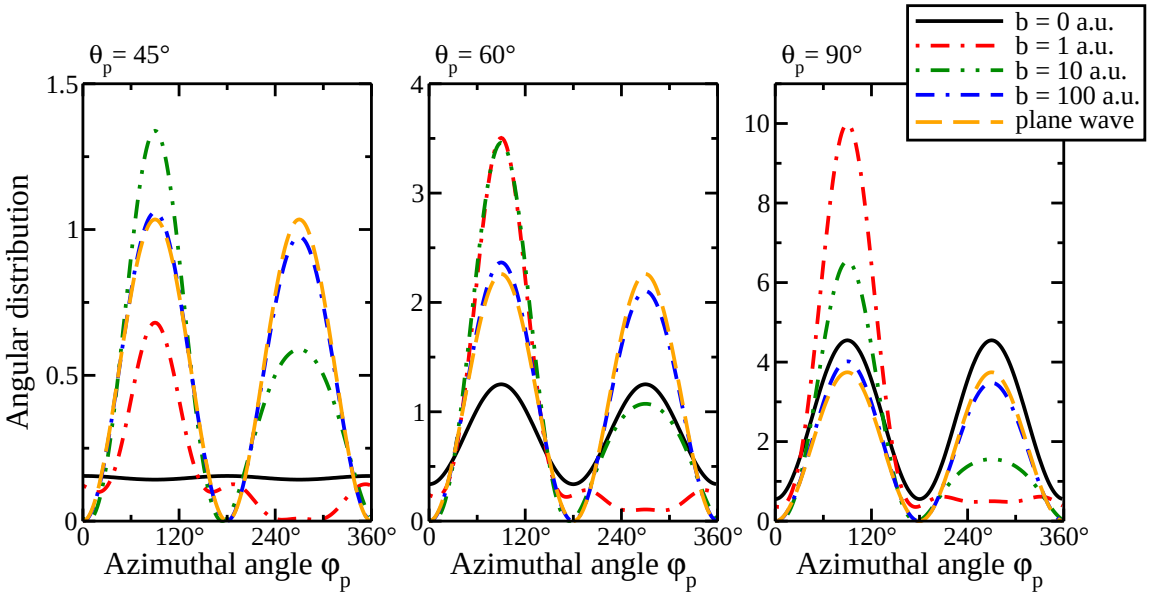

Figure 7.6. – Same as in Fig. 7.1 but for the ionization of the $2p_y$-level.

the beam center (cf. Fig. 7.1). Likewise, we can expect an asymmetric emission of the photoelectrons if we break the symmetry of the initial system of light beam "plus" atom by employing an atomic bound state that is *spatially oriented*. A particular state that exhibits such a spatial orientation is given by the $2p_y$-level of the hydrogen atom (see Sec. 3.2). The geometrical setup for the ionization process of such a state by twisted photons was introduced in Sec. 5.2.1. As a reminder, we employ here a setup where the electronic cloud of the $2p_y$-state is strongly concentrated along an axis perpendicular to the propagation direction of the incoming Bessel beam. We note that such a (transverse) orientation of the electronic bound state should be visible, in particular, for the emission patterns of the photoelectrons axially around the light beam axis.

In Fig. 7.6 we show the azimuthal angular distribution for electrons that are emitted during the ionization process of the $2p_y$-level of a hydrogen atom by a twisted light beam. Calculations have been performed for three different polar angles, $\theta_p = 45°$ (left panel), $\theta_p = 60°$ (middle panel), and $\theta_p = 90°$ (right panel) and for impact parameters in the range $0 \leq b \leq 100$ a.u. Results are compared to the corresponding electron distribution for the ionization process with plane electromagnetic waves.

As the figure illustrates, even if the atom is positioned in the center of the light beam, the electron emission pattern shows a pronounced shape along the emission angle φ_p. This is expected, since the emission pattern should reflect that the initial atom-photon system is not axial symmetric around the z-axis due to the spatial orientation of the $2p_y$-level. If we translate the atom out of the beam center, the angular distribution of the electrons varies strongly with respect to the axial angle

φ_p, but for impact parameters $b \geq 100$ a.u. it becomes similar to the distribution that is found for the ionization with plane wave photons. We can understand this behaviour with the same reasoning as for the photoeffect of the $1s$ ground state: near to the beam axis the azimuthal phase dependency of the beam can significantly affect the electron emission pattern. Far away from the beam center, however, the phase (as well as the beam intensity) are nearly constant over the extension of the electron cloud and, hence, the angular distribution converges to the one for the plane wave case. This concludes our discussion on the ionization process of the $2p_y$-level of a hydrogen atom by a twisted Bessel beam.

Let us give in the following some brief and final remarks regarding our general findings for the ionization process with twisted photons. In this chapter, we have performed a detailed analysis for the ionization process of neutral hydrogen atoms by twisted photons. The obtained results (see Figs. 7.1–7.6) illustrate, for example, that a pronounced φ_p- and θ_p-behaviour of the electron angular distribution $W^{\mathrm{tw}}(\theta_p, \varphi_p)$, which originates from the phase structure (paraxial regime) or oscillations in the intensity profile (non-paraxial regime) of the twisted light waves, can be observed for impact parameters in the range $0 \leq b \leq 100$ a.u. and $0 \leq b \leq 10\,000$ a.u., respectively. We note that an experimental measurement of the predicted effects would require an operational control of the impact parameter b [68]. Even though such a control is a complicated task, recent advances in atomic trap technologies promise that it might become feasible in the near future. For example, it is currently practicable to trap an atom with a spatial uncertainty of several nm [123–125], which is just of the order where the characteristic photoionization features of the Bessel beams become visible (cf. Fig. 7.3). With these remarks, we conclude our discussion on the ionization process of atoms by twisted Bessel beams and proceed in the next chapter with the radiative capture of twisted electrons by bare ions.

8. Radiative Recombination with Twisted Electrons: Results and Discussion

In Chapter 6 we established a theoretical method to analyze the radiative capture of twisted electrons into the ground state of (finally) hydrogen-like ions. Here we will use this method to investigate the angular distribution as well as the polarization state of the photons that are emitted in the radiative capture of twisted electrons by bare protons. The geometrical setup of this capture process will follow the prerequisites introduced in Sec. 6.3.1; that is, a proton beam with a (transverse) Gaussian density distribution shall collide head-on with a twisted (Bessel) electron beam—the beam axes are aligned with each other. The twisted beam carries, moreover, a well-defined OAM m along its propagation direction as well as transverse and longitudinal momenta $\varkappa$ and p_z. Overall, the geometrical setup is cylindrically symmetric around the beam axis and, hence, the properties of the RR photons will be insensitive to the azimuthal angle φ_k. Therefore, we will study the photon properties—angular distribution and polarization state—solely as a function of the polar emission angle θ_k. As we will show in the next sections, these *polar* (angle and polarization) distributions of the RR photons may be strongly affected by varying the parameters of the incoming twisted electron beam. We note again that parts of the following discussion will be similar to the corresponding sections in our (preprint) manuscript [122] (submitted to New J. Phys).

8.1. K-Shell Capture of Twisted Electrons by Bare Protons: Photon Properties

In the following, we will investigate the radiative capture of twisted electrons into the K-shell of (finally) hydrogen atoms for a fixed kinetic energy $E_{\text{kin}} = 2\,\text{keV}$ of the electron beam (different energies will be considered later). In particular, we will here focus on how the properties—angular distribution and polarization—of the emitted photons are affected by varying the opening angle $\theta_p = \arctan(\varkappa/p_z)$ and thus the transverse and longitudinal momenta $\varkappa$ and p_z of the electron beam (cf. Fig. 2.2). We note moreover that the longitudinal OAM m of the beam can be chosen arbitrarily,

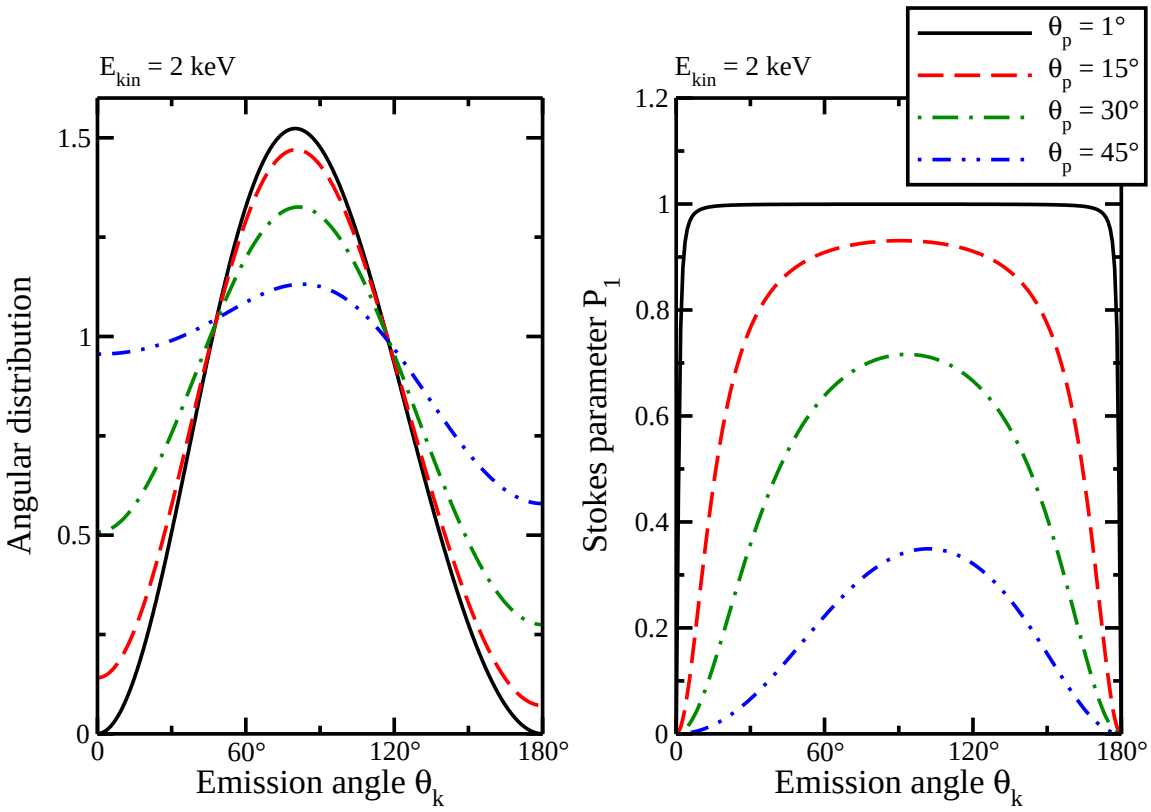

Figure 8.1. – Angular distribution (left panel) and Stokes Parameter P_1 (right panel) of RR photons emitted in the K-shell capture of twisted electrons by (finally) hydrogen atoms. Calculations have been performed for an electron energy of 2 keV and for different opening angles: $\theta_p = 1°$ (black solid line), $\theta_p = 15°$ (red dashed line), $\theta_p = 30°$ (green dashed-dotted line) and $\theta_p = 45°$ (blue dashed-double-dotted line).

since for the present geometrical setup the photon properties are insensitive to the beam's OAM as was found in Sec. 6.3.2.

In Fig. 8.1 we show the angular distribution (left panel) as well as the first Stokes parameter (right panel) of the photons emitted in the RR scenario described above as a function of the polar emission angle θ_k. Results are obtained for four different opening angles θ_p of the incoming twisted electron beam ranging from the paraxial to the non-paraxial beam regime: $\theta_p = 1°$, $\theta_p = 15°$, $\theta_p = 30°$, and $\theta_p = 45°$. The second and third Stokes parameters are not shown, since they vanish (see Sec. 6.3.3).

As seen from the left panel of Fig. 8.1, the angular distribution of the emitted photons changes significantly by varying the opening angle of the incoming electron beam. For instance, within the *paraxial* beam regime as given by the small opening angle $\theta_p = 1°$, the emission pattern of the RR photons follows a (slightly modified) $\sin^2\theta_k$-distribution (as is expected from our discussion in Sec. 6.3.4). Consequently,

within the paraxial regime the RR photons are preferentially emitted transverse (around $\theta_k = 90°$) to the propagation direction of the electron beam, whereas (nearly) no photons are observed along the beam axis ($\theta_k = 0$ and $\theta_k = 180°$). However, if we depart from the paraxial beam regime by turning to larger opening angles $\theta_p \geq 15°$, it is found that the probability to emit the RR photons in the forward ($\theta_k = 0°$) and backward ($\theta_k = 180°$) directions increases considerably, while it decreases in the transverse direction ($\theta_k = 90°$). In the forward direction, for example, the angular distribution of the RR photons raises from (nearly) zero in the paraxial regime ($\theta_p = 1°$) to a considerable value of 0.96 within the non-paraxial regime ($\theta_p = 45°$)—a value which is almost as high as the maximal value 1.13 of the distribution at $\theta_k = 83°$. The increase of RR photons in the backward direction is lower but still remarkable: while in the paraxial regime ($\theta_p = 1°$) the angular distribution is (again) almost zero at the angle $\theta_k = 180°$, it amounts to the considerable value 0.58 within the non-paraxial beam regime ($\theta_p = 45°$).

To understand the behaviour of the photon distribution as described above, we turn to the description of the incoming twisted (Bessel) beam in terms of plane waves; more specifically, we draw on the property that the wave vectors of the plane waves that compose the Bessel beam lie on a cone with the opening angle θ_p (cf. Fig. 2.2). As we discussed in Sec. 3.1.2, if this opening angle is close to zero, $\theta_p \approx 0$, the twisted electron beam starts to behave like an "ordinary" plane wave beam—a beam without OAM along its propagation axis. Hence, for the RR process with a *paraxial* twisted electron beam, i. e. a beam with a small opening angle θ_p, the emission pattern of the RR photons will reflect such a "plane wave" behaviour. For the K-shell capture of plane wave electrons, the emission pattern of the recombination photons follows a (modified) $\sin^2\theta_k$-law as was shown in Sec. 6.2.2—a pattern that is seen in the left panel of Fig. 8.1 for the paraxial beam with the opening angle $\theta_p = 1°$. It is an important characteristic of the RR process with plane wave electrons that the photon emission into the forward and backward direction is forbidden. This comes from the conservation law of the total angular momentum along the quantization (z-)axis: the captured (plane wave) electrons carry no angular momentum along the quantization axis, whereas the outgoing plane wave photons always possess a non-zero SAM along the propagation direction. Therefore, it is impossible to fulfill the angular momentum conversion between the incident electrons and the photons that are emitted in the forward or backward direction. However, if the propagation direction of the plane wave is tilted out of the z-axis, the angular momentum conservation is "weakened" and an emission of the RR photons along the z-axis becomes possible. Since the Bessel beam is composed of such tilted plane waves with the tilt angle given by the opening angle θ_p, the photon emission into the forward and backward direction is possible if the opening angle is sufficiently large—a condition that is fulfilled within the non-paraxial beam regime. This explains why a remarkable number of photons can be observed in the forward and backward direction as was seen in the left panel of Fig. 8.1 for the RR process with non-paraxial electron beams ($\theta_p \geq 15°$).

Apart from the angular distribution, we also depict the polarization state of the RR photons in terms of the first Stokes parameter P_1 in the right panel of Fig. 8.1. As the figure illustrates, the Stokes parameter P_1 changes significantly if we vary the opening angle θ_p of the electron beam. In the paraxial regime as corresponding to the small opening angle $\theta_p = 1°$, for instance, the parameter P_1 is nearly constant and equal to one over the wide range $10° \leq \theta_k \leq 170°$ of polar emission angles. For the forward ($\theta_k = 0$) and backward ($\theta_k = 180°$) direction, however, P_1 drops quickly to zero. When we turn to larger opening angles θ_p of the electron beam, however, the Stokes parameter P_1 decreases strongly for all emission angles θ_k of the photons. For example,the parameter P_1 reduces by 64% at the angle $\theta_k = 90°$ if we turn from the paraxial regime ($\theta_p = 1°$) to the non-paraxial regime ($\theta_p = 45°$) of the electron beam. We note that such a reduction of the photon polarization can be easily measured with state-of-the-art polarization detectors and may be used therefore to characterize the opening angle of the electron Bessel beam.

We can explain the behaviour of the Stokes parameter P_1 with the same reasoning as for the angular distribution of the RR photons. That is, within the paraxial regime a Bessel beam of electrons behaves (nearly) like a "standard" plane wave beam and, therefore, the first Stokes parameter should be similar to the one that is obtained for the RR process with plane wave electrons. As we have shown in Sec. 6.2.2, for the radiative capture of plane wave electrons that travel along the z-axis, the first Stokes parameter is identical to *one* (see Eq. (6.39)). However, when we depart from the paraxial beam regime and turn to larger opening angles θ_p, the polarization state of the RR photons does not have to reflect the behaviour for the capture process of plane wave electrons anymore and, hence, the Stokes parameter P_1 may show a pronounced shape with respect to the emission angle θ_k, as observed in the right panel of Fig. 8.1 for $\theta_p \geq 15°$. It is noticeable that—regardless if we are in the paraxial or non-paraxial beam regime—the Stokes parameter P_1 is always zero for the photon emission in the forward and backward direction. We can understand this if we recall that a Bessel beam is composed of plane waves that lie on a cone around the propagation axis. An "individual" wave of this cone may now result in some arbitrary value of the parameter P_1. However, when we measure the parameter P_1 for photons that are emitted along (or counter to) the propagation direction of the beam, each wave of the beam's cone will have a counter part which produces a value of the parameter P_1 that is exactly opposite in sign. The values for P_1 generated by these "opposing" pairs will cancel and therefore P_1 vanishes for the forward and backward emission.

So far, we have analyzed the RR process for a twisted electron beam with a fixed kinetic energy of $E_{\text{kin}} = 2\,\text{keV}$. Let us now extend our analysis also to other energies of the beam.

8.2. K-Shell Capture of Twisted Electrons by Bare Protons: Energy Dependency of Photon Properties

In the previous section, we discussed the properties of the RR photons in dependence on the opening angle θ_p of a twisted electron beam with a *fixed* kinetic energy. Let us come now to the "inverse" scenario, that is, we analyze the angular distribution and the polarization of the RR photons for different energies E_{kin} of the electron beam, while the opening angle θ_p is held constant. For our analysis, we will take an opening angle of $\theta_p = 45°$ as corresponding to the *non-paraxial* beam regime—a choice for which we expect to see the most pronounced effects on the photon properties by varying the kinetic energy of the electron beam.

In Fig. 8.2 we display the angular distribution (top-left panel) as well as the first Stokes parameter (top-right panel) for the RR photons that are emitted in the scenario described above. Results are shown for three different kinetic energies of the electron beam: $E_{\text{kin}} = 1\,\text{keV}$ (black solid line), $E_{\text{kin}} = 10\,\text{keV}$ (red dashed line), and $E_{\text{kin}} = 100\,\text{keV}$ (green dashed-dotted line). For comparison, we display in the bottom row of the figure the angular distribution (bottom-left panel) and the first Stokes parameter (bottom-right panel) for the RR process with plane wave electrons (possessing the same kinetic energies). As seen from the top-left panel of the figure, the angular distribution of the recombination photons is strongly affected if we change the order of magnitude for the energy E_{kin} of the incoming electron beam. The more we increase the energy of the beam, the more the emission of the RR photons in the forward direction ($\theta_k = 0$) is preferred in comparison to the backward emission ($\theta_k = 180°$). For example, for an energy $E_{\text{kin}} = 100\,\text{keV}$ of the non-paraxial Bessel beam, approximately thirty times more photons are emitted in the forward than in the backward direction. Such a preference of the forward direction for increasing beam energies is known from the RR process with plane wave electrons (cf. bottom-left panel of Fig. 8.2), but with the important difference that in the plane wave case the photon emission in the exact forward direction ($\theta_k = 0$) is forbidden, while it is allowed (and significantly preferred) for the RR process with (non-paraxial) twisted electrons.

Moreover, the polarization of the recombination photons in terms of the first Stokes parameter may also be significantly affected by varying the beam energy, as seen from the top-right panel of Fig. 8.2. While for the kinetic energies $E_{\text{kin}} = 1\,\text{keV}$ and $E_{\text{kin}} = 10\,\text{keV}$ the parameter P_1 is positive (or zero) for all polar emission angles θ_k, it can be negative for a beam energy of $100\,\text{keV}$ and emission angles $0 \leq \theta_k \leq 60°$ of the RR photons. Furthermore, we remark that the Stokes parameter P_1 for the RR photons emitted in the capture of twisted electrons shows a completely different angular dependency than for the RR process with plane wave electrons

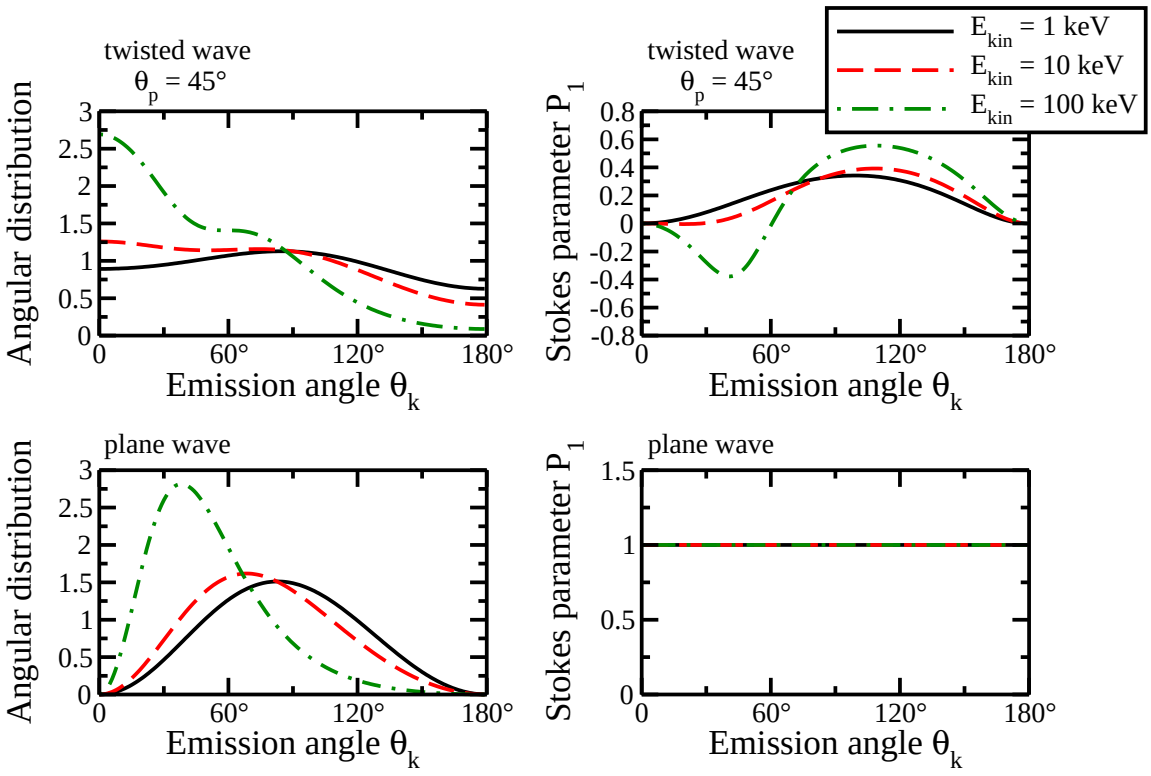

Figure 8.2. – Angular distribution (top-left panel) and Stokes parameter P_1 (top-right panel) of RR photons emitted in the radiative capture of twisted electrons into the K-shell of (finally) hydrogen atoms. Calculations have been performed for an opening angle $\theta_p = 45°$ of the electron beam (corresponding to the non-paraxial regime) and for three different electron energies: $E_{\rm kin} = 1\,{\rm keV}$ (black solid line), $E_{\rm kin} = 10\,{\rm keV}$ (red dashed line), and $E_{\rm kin} = 100\,{\rm keV}$ (green dashed-dotted line). For comparison we display in the bottom row the angular distribution and the first Stokes parameter for the RR process with plane wave electrons.

(cf. bottom-right panel of Fig. 8.2). While for the RR process with twisted electrons the parameter P_1 exhibits a pronounced shape along the polar emission angle θ_k, it is constant and equal to one for the capture of *non-relativistic* plane wave electrons (regardless of their particular kinetic energy in the range $1\,{\rm keV} \leq E_{\rm kin} \leq 100\,{\rm keV}$).

Finally, we must note that for a beam energy $E_{\rm kin} = 100\,{\rm keV}$ the electrons may start to behave relativistically and therefore our (non-relativistic) formalism may fail to accurately describe the emission pattern as well as polarization state of the recombination photons. Nevertheless, by going to the limit of the allowed energy range for the twisted electron beam, we see that the properties of the emitted RR photons may show pronounced features such as the clear preference of the forward emission of the RR photons.

So far, we have discussed the radiative recombination of twisted electrons that are in a *pure state* with a well-defined OAM along the propagation direction. However, as has been mentioned in Sec. 6.3, the photons that emerge from such a RR process are insensitive to the longitudinal OAM of the twisted electron beam. We can overcome such an insensitivity if we turn to a different geometrical setup where we employ—instead of a pure OAM state—a *superposition* of twisted electron beams with different topological charges. Let us analyze the RR process for such a superposition scenario in the next section.

8.3. K-Shell Capture of Twisted Electrons by Bare Protons: Superposition of Electron Beams

Suppose we are given the same RR scenario as in the previous section, but instead of a twisted electron beam in a *pure state* with a well-defined OAM m along the propagation direction, we *coherently superimpose* the twisted beam with a "reference" beam whose longitudinal OAM vanishes:

$$\psi_i^{\mathrm{tw}}(\mathbf{r}) = \frac{1}{\sqrt{2}} \Big[\psi^{\mathrm{tw}}_{\varkappa, m_1=0, p_z}(\mathbf{r}) + \psi^{\mathrm{tw}}_{\varkappa, m_2=m, p_z}(\mathbf{r}) \Big]. \tag{8.1}$$

As seen from this equation, both the reference state $\psi^{\mathrm{tw}}_{\varkappa, m_1=0, p_z}$ as well as the twisted "probe" state $\psi^{\mathrm{tw}}_{\varkappa, m_2=m, p_z}$ carry the same transverse and longitudinal momenta $\varkappa$ and p_z. Moreover, these states possess the same *weight*, that is, they are found with equal probability within the coherent mixture (8.1). Now with respect to the RR process, by providing such a reference state for the twisted electron beam, the recombination photons are subject to a completely new setting based on which they may "feel" the longitudinal OAM m of the twisted electron beam. In particular, it is expected that an OAM-dependent *interference* between the two superimposed states during the RR process may significantly affect the properties of the emitted photons (cf. Eq. (6.41)). We note that the geometrical setup as well as the theoretical treatment of such a superposition scenario was discussed in Sec. 6.3.5.

For the analysis of the RR process with the mixed electron state (8.1), we will use two different sets of parameters describing such a state as given by the second and third column of Tab. 8.1. For both sets, the kinetic energy of the beam is chosen as $E_{\mathrm{kin}} = 2\,\mathrm{keV}$, whereas the opening angle of the beam's momentum cone is given by $\theta_p = 45°$ as corresponding to the non-paraxial beam regime (the paraxial regime will be discussed later). The two scenarios differ, however, in the longitudinal OAM m that is carried by the twisted probe state; in the first scenario as given by the second column of Tab. 8.1, we analyze the RR process for a probe beam with an OAM of either $m = \pm 1$ along the propagation axis, whereas the second scenario

beam parameter	first scenario	second scenario
beam energy E_{kin}	2 keV	2 keV
opening angle θ_p	45°	45°
longitudinal momentum p_z	8.57 a.u.	8.57 a.u.
transverse momentum $\varkappa$	8.57 a.u.	8.57 a.u.
longitudinal OAM m of probe beam	± 1	± 2

Table 8.1. – Parameters of the superposition state (8.1) as used in the calculations.

(third column of the table) uses a probe beam with a longitudinal OAM of either $m = \pm 2$.

Let us begin now to analyze the RR process for an electron beam that is in a superposition state as described by Eq. (8.1) and where the beam parameters are given by the second column of Tab. 8.1. For this scenario, we display in Fig. 8.3 the angular distribution (top panels) as well as the Stokes parameters P_1 and P_2 (middle and bottom panels) of the RR photons as a function of the polar angle θ_k and for two azimuthal angles: $\varphi_k = 45°$ (left column) and $\varphi_k = 90°$ (right column). Results have been obtained numerically with the help of Eq. (6.41) for the photon-spin density matrix together with Eqs. (6.7)–(6.10) for the angular distribution and the Stokes parameters. The obtained results are compared, moreover, to the corresponding ones for the (OAM-independent) capture process of twisted electrons in a pure OAM state (see Sec. 8.1).

As seen from both panels in the top row of Fig. 8.3, the polar emission pattern of the RR photons changes considerably by varying the longitudinal OAM m of the probe beam. For example, while at the solid angle $(\theta_k = 45°, \varphi_k = 90°)$ the angular distribution of the RR photons as caused by the electron state with $m = -1$ is double as high as the one for $m = +1$, it is only half as high (as the one for $m = +1$) at $(\theta_k = 160°, \varphi_k = 90°)$. Moreover, regardless of the longitudinal OAM m of the probe beam, it is seen that the emission pattern of the RR photons as caused by the mixed beam state (8.1) oscillates around the one obtained for an electron beam in a pure OAM state with the same beam parameters. This oscillation originates from an *interference* during the RR process between the two superimposed electron beams—the corresponding *interference term* appeared in the associated photon-spin density matrix (6.41) and depends on the difference $\Delta m = m_2 - m_1 = m$ of the topological charges of the two superimposed beams. Finally, we note that although the transverse structure of the electron density for the mixed state (8.1) is insensitive to whether the longitudinal OAM m of the twisted beam is plus or minus one (see Fig. 6.4), different shapes arise for the emission pattern of the RR photons and allow to distinguish between these two cases. Such different patterns can be attributed to the *internal* phase structure of the superposition state, which is determined by the longitudinal OAM m of the probe state and may strongly affect the emission

process of the photons (but which is indiscernible by the beam's density profile). As a conclusion, by measuring the angular distribution of the emitted photons for the RR process with an electron beam in the superposition state (8.1), we obtain access to the longitudinal OAM m of the twisted probe beam—a feature that was absent for the RR process with a twisted beam in a pure OAM state (see Sec. 8.1).

Apart from the angular distribution, we show in the middle and bottom panels of Fig. 8.3 the Stokes parameters P_1 and P_2 of the emitted photons, again as a function of the polar angle θ_k and for the two azimuthal angles $\varphi_k = 45°$ (left column) and $\varphi_k = 90°$ (right column). As is seen there, the magnitude of the Stokes parameter depends not only crucially on the polar and axial angles θ_k and φ_k but also on the value m of the longitudinal OAM of the twisted probe beam. For example, the middle-right panel illustrates that there is the large range of polar emission angles $0 \leq \theta_k \lesssim 63°$ for the RR photons (the axial angle is fixed to $\varphi_k = 90°$), where the Stokes parameter P_1 is negative (down to a value of -0.47 at $\theta_k \approx 35°$) if the OAM state $m = +1$ is employed, but where it is positive (up to a value of 0.41 at $\theta_k \approx 58°$) if the longitudinal OAM of the probe state is $m = -1$. Moreover, in contrast to the RR process with an electron beam in a pure OAM state, where only the first Stokes parameter is non-zero, in the present case the parameter P_2 may have a considerable magnitude for both, superposition of electron beams with $m_1 = 0$ and either $m_2 = -1$ or $m_2 = +1$ (the third Stokes parameter, however, still vanishes). The exact magnitude of the parameter P_2, however, depends strongly on the polar and axial emission angles θ_k and φ_k of the RR photons. While for an axial angle of $\varphi_k = 45°$, the second Stokes parameter possesses a considerable (negative or positive) value for nearly all polar angles θ_k (except for $\theta_k \approx 0$ and $\theta_k \approx 180°$), it vanishes for all polar angles θ_k regardless of the OAM state of the probe beam if the axial angle is chosen as $\varphi_k = 90°$. We note that the strong variations in the magnitude of the Stokes parameters can be easily measured with state-of-the-art polarization detectors. Such polarization measurements are not only important for the analysis of the RR process with twisted electron beams but may also help to characterize the incoming electron beam and determine, for example, its OAM state.

Until now, we focused our analysis of the RR (superposition) scenario on the θ_k-dependency of the photon observables. However, since the density profile of an electron beam in the superposition state (8.1) can possess a transverse structure that is not axially symmetric around the beam's propagation direction (see Fig. 6.4), it is to expect that the properties of the RR photons will also depend on the *axial* emission angle φ_k. To illustrate this axial behaviour, we display in Fig. 8.4 the angular distribution (top row) as well as the Stokes parameters P_1 (middle row) and P_2 (bottom row) of the RR photons as a function of the axial angle φ_k and for two polar angles $\theta_k = 45°$ (left column) and $\theta_k = 90°$ (right column). Calculations have again been performed for beam parameters as given by the second column of Tab. 8.1. As can be seen from Fig. 8.4, regardless of the longitudinal OAM m of

the probe beam, all of the photon properties—the angular distribution as well as the Stokes parameters—may be affected strongly by changing the axial angle φ_k under which the emitted photons are observed. For example, for both values of the longitudinal OAM of the probe state, $m = -1$ and $m = +1$, the axial angular distribution for the RR photons at a polar angle $\theta_k = 45°$ oscillates between the values 0.68 and 1.39 by varying the axial angle φ_k. This is in stark contrast to the constant distribution of an (axially symmetric) electron beam in a pure OAM state, which is also plotted in Fig. 8.4 (solid black line) for comparison. However, for the polar angle $\theta_k = 90°$ (top-right panel), the magnitude of the oscillations in the axial angular distribution of the RR photons is not as pronounced as for $\theta_k = 45°$. Beside the emission pattern of the RR photons, the Stokes parameters P_1 and P_2 may also show a pronounced φ_k-dependency as seen, for example, in the middle-left and bottom-left panel for a polar angle $\theta_k = 45°$. However, while the second Stokes parameter still shows this pronounced dependency for the polar angle $\theta_k = 90°$ (bottom-right panel), i.e. transverse to the propagation direction of the incoming electron beam, the variation of the parameter P_1 along the axial angle φ_k is nearly neglectable (middle-right panel). Overall, we conclude that a complex axial structure is present within the angular distribution as well as the Stokes parameters of the RR photons that are emitted in the superposition scenario described above.

Let us now analyze the RR process for the state (8.1) with beam parameters given by the third column of Tab. 8.1; that is, instead of a superposition state (8.1) with $m_1 = 0$ and $m_2 = \pm 1$, we employ a state where the probe beam possesses a longitudinal OAM of $m_2 = \pm 2$. In Fig. 8.5 we display the properties, angular distribution (first row), Stokes parameter P_1 (second row), and Stokes parameter P_2 (third row) of the photons that are emitted in such a RR scenario as a function of the polar emission angle θ_k. Calculations have been performed for two azimuthal angles $\varphi_k = 45°$ (left column) and $\varphi_k = 90°$ (right column). In the following, however, rather than providing again a lengthy discussion of these photon properties, we will focus on the main differences of the present case in comparison to the scenario presented above. As all panels of Fig. 8.5 illustrate, the most noticeable difference is that here the emitted photons do not "distinguish" between the longitudinal OAM $m = \pm 2$ of the probe beam, so that the observables show the same θ_k-behaviour regardless if m is plus or minus two. Nevertheless, for certain emission angles (θ_k, φ_k) the properties of the recombination photons may still be different from the corresponding ones for the RR process with a twisted electron beam in a pure state—a behaviour that can be seen, for example, for the (polar) angular distribution at an axial angle $\varphi_k = 90°$ (top-right panel), or for the Stokes parameters P_1 and P_2 at $\varphi_k = 90°$ and $\varphi_k = 45°$, respectively (middle-right and bottom-left panels). As a conclusion, although it is not possible to distinguish between the OAM states with $m = \pm 2$ of the probe beam by measuring the (angle-differential) properties of the RR photons, such a measurement allows to access the *absolute* value of the longitudinal OAM m. To observe these

effects, however, it is important under which solid angle (θ_k,φ_k) the photon detector is placed, since for certain detector arrangements the OAM effects may vanish.

Apart from the polar dependency of the photon observables as discussed above, we show in Fig. 8.6 the properties of the recombination photons as a function of the axial emission angle φ_k. Results are displayed for two polar angles $\theta_p = 45°$ (left column) and $\theta_p = 90°$ (right column). As seen from all panels of the figure, the observables show a pronounced φ_k-dependency if a probe beam in an OAM state with either $m = +2$ or $m = -2$ is employed within the RR process. For the present scenario, however, such an (angle-differential) measurement of the observables does not discriminate between the different values of the longitudinal OAM m, as was already seen above for the θ_k-dependency of the observables. Yet, by detecting the axial characteristics of the emitted photons, it is easily possible to distinguish the present superposition scenario from the case where a "single" twisted beam with a well-defined projection of its OAM is used, as can be seen in all panels of Fig. 8.6. We note, moreover, that all observables—emission pattern and Stokes parameters of the RR photons—show a 180°-periodicity as a function of the azimuthal angle φ_k. This behaviour complies with the structure of the beam's density profile (see Fig. 6.5), which is symmetric under a rotation by an axial angle of 180° around the propagation axis of the beam.

Finally, we would like to remark how the emission pattern as well as the polarization state of the RR photons emitted in the superposition scenario are changed if we turn to (i) the *paraxial* regime, $\varkappa \ll p_z$, or (ii) to larger values of the longitudinal OAM m of the probe beam, $m > 2$. Detailed analysis of these cases has shown that by turning to either one, (i) or (ii), the results obtained for the RR scenario with the superimposed electron beams become indistinguishable from the corresponding ones for the capture of a pure twisted beam in a well-defined OAM state. For both settings, such a behaviour can be entirely attributed to *weak* interference effects between the superimposed beams during the RR process, that is, the interference term in the photon-spin density matrix (6.41) for the cases (i) and (ii) nearly vanishes. As a result, the beams act *independently* from each other during the RR process and, hence, each of the beams *individually* causes the same (OAM-independent) patterns of the photon observables that have been obtained for the pure OAM state. With this final remark, we close our discussion on the RR process with twisted electron beams. In the next chapter, we will summarize our main findings for this recombination process as well as for the atomic photoeffect by twisted photons that we analyzed in the previous chapter.

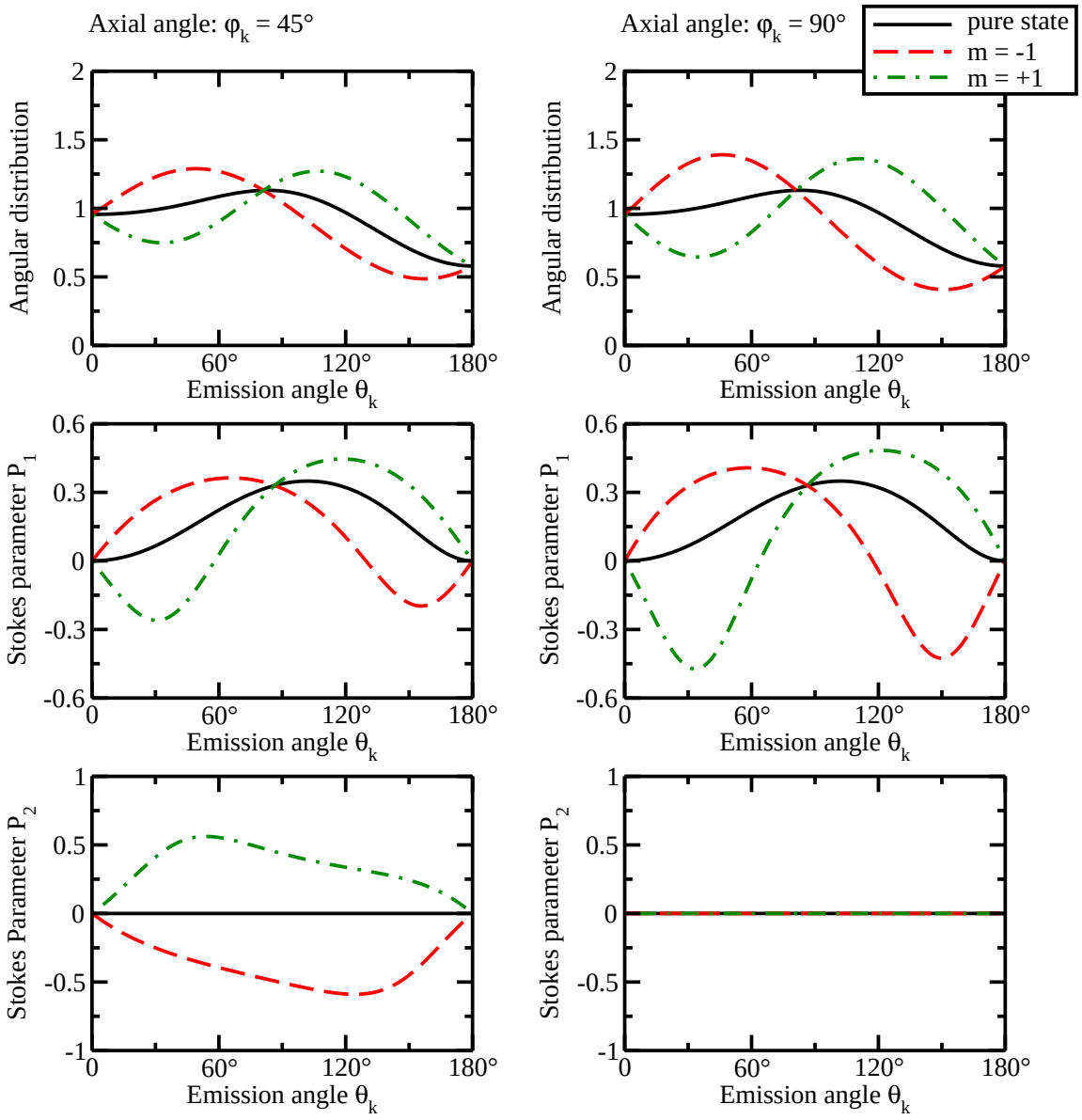

Figure 8.3. – Angular distribution (top row) and Stokes parameters P_1 (middle row) and P_2 (bottom row) of RR photons for the radiative capture of twisted electrons by (finally) hydrogen atoms. The electrons are assumed to be in the superposition (8.1) of two states with different longitudinal OAM: $m_1 = 0$ and $m_2 = m = -1$ (red dashed line) or $m_1 = 0$ and $m_2 = m = +1$ (green dashed-dotted line). Calculations have been performed within the non-paraxial regime ($\theta_p = 45°$) and for an electron energy of 2 keV as well as for two azimuthal angles: $\varphi_k = 45°$ (left column) and $\varphi_k = 90°$ (right column). Results are shown as a function of the polar emission angle θ_k and are compared, moreover, to the (OAM-independent) distributions for the RR process with a twisted electron beam in a pure OAM state (black solid line).

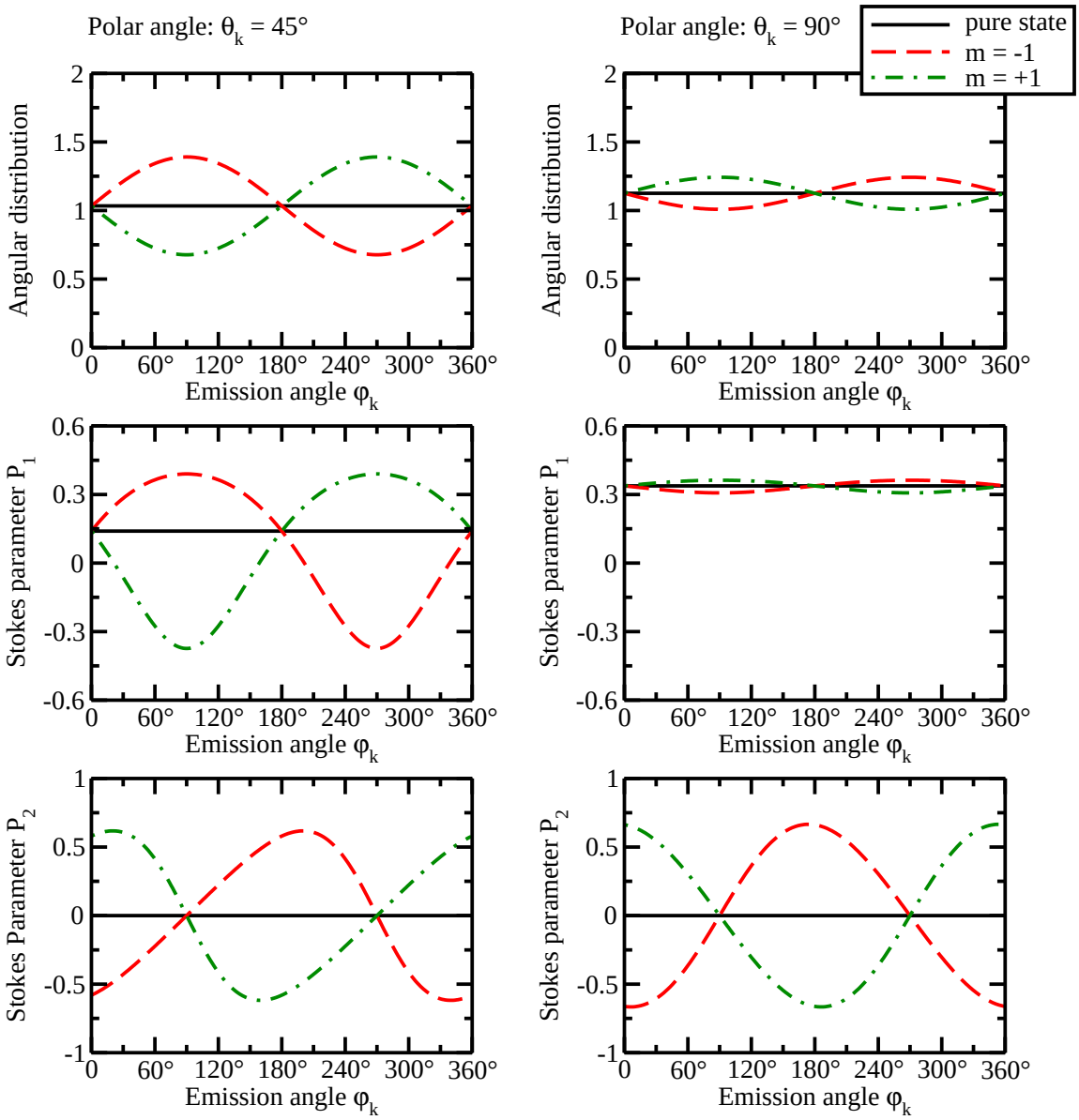

Figure 8.4. – Angular distribution (top row) and Stokes parameters P_1 (middle row) and P_2 (bottom row) of RR photons for the radiative capture of twisted electrons by (finally) hydrogen atoms. The electrons are assumed to be in the superposition (8.1) of two states with different longitudinal OAM: $m_1 = 0$ and $m_2 = m = -1$ (red dashed line) or $m_1 = 0$ and $m_2 = m = +1$ (green dashed-dotted line). Calculations have been performed within the non-paraxial regime ($\theta_p = 45°$) and for an electron energy of 2 keV as well as for two polar angles: $\theta_k = 45°$ (left column) and $\theta_k = 90°$ (right column). Results are shown as a function of the axial emission angle φ_k and are compared, moreover, to the (OAM-independent) distributions for the RR process with a twisted electron beam in a pure OAM state (black solid line).

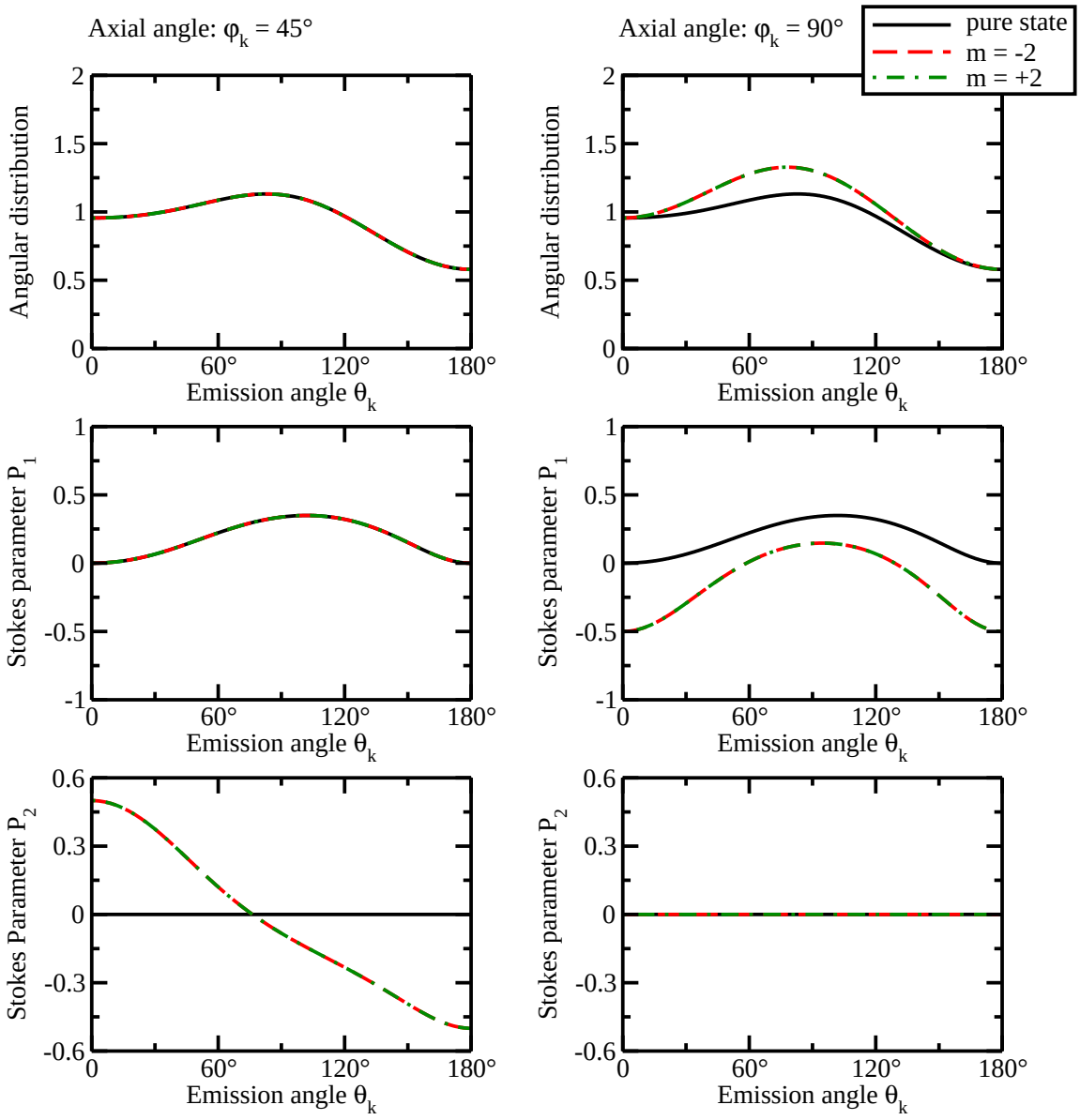

Figure 8.5. – Same as in Fig. 8.3 but for $m = \pm 2$.

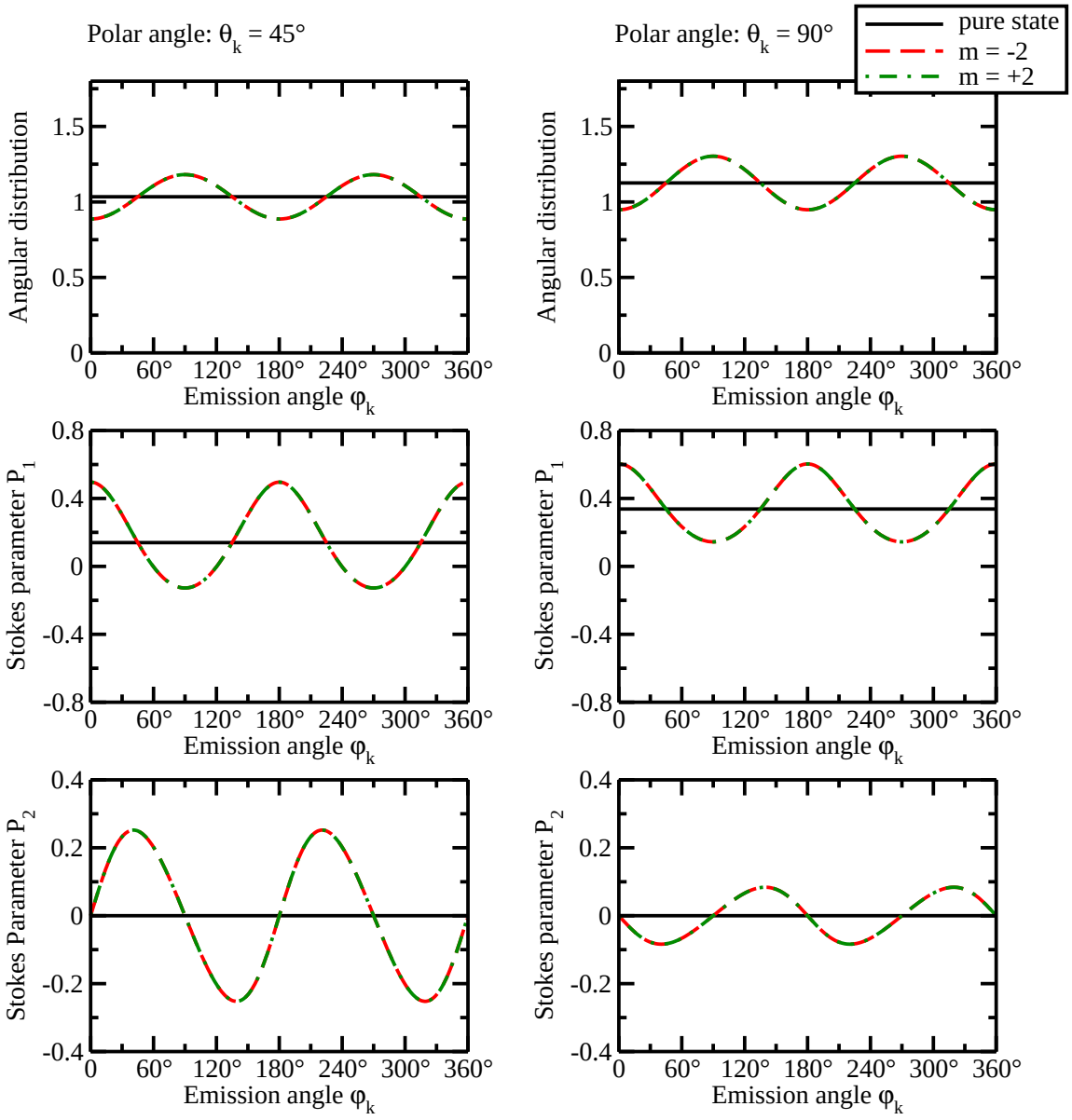

Figure 8.6. – Same as in Fig. 8.4 but for $m = \pm 2$.

9. Summary and Outlook

In this work, we established a novel theoretical formalism to analyze the atomic processes of (a) ionization of (initially) hydrogen-like ions by twisted photons and (b) radiative capture of twisted electrons by (initially) bare ions. To do so, we first introduced how we describe the different (initial and final) states of the particles—photons and electrons—for these processes. For the *plane* and *twisted* photon states, this led us in Chapter 2 to Maxwell's equations of light. The hydrogenic *bound* as well as (plane and twisted) *continuum* states of the electrons were characterized in Chapter 3 by the (non-relativistic) Schrödinger equation. Apart from the description of the particle states, we had to lay out how we "guide" these states through the different atomic processes. A well-established method to describe this guiding is given by the time-dependent first-order perturbation theory, which we presented in Chapter 4. The central quantities of this theory are the so-called *transition amplitudes*, quantities that provide access to the main observables of the interaction process in question. In Chapter 5 we derived these amplitudes for the photoeffect of hydrogen-like ions by twisted (Bessel) photons. By employing the transition amplitudes, we were able to obtain the angular distribution of the photoelectrons emitted in the ionization of hydrogenic ions by twisted photons. Beside the ionization process, we analyzed in Chapter 6 the radiative capture of (non-relativistic) twisted electrons into the K-shell of (finally) hydrogen-like ions by employing the associated transition amplitudes within the so-called *density matrix framework*. This framework allowed us to derive concise analytical formulas that describe the emission characteristics of the recombination photons—the angular distribution as well as the polarization state in terms of the Stokes parameters. Altogether, for both the ionization and the recombination process, our theoretical formalism is most general: it is applicable for arbitrary opening angles $\theta_p = \arctan(\varkappa/p_z)$ of the twisted particle beam—$\varkappa$ and p_z being the transverse and longitudinal momentum of the beam—and, hence, can be employed not only in the *paraxial* beam regime as constituted by small opening angles $\theta_p \ll 45°$ but also in the non-paraxial regime, where the transverse momentum has the same order of magnitude as the longitudinal one such that the opening angle is $\theta_p \approx 45°$.

In Chapter 7, we applied our theoretical formalism to examine the ionization process by twisted light beams for several atomic systems and for different settings of the beam parameters (corresponding not only to the paraxial but also the non-paraxial beam regime). For instance, we performed a detailed analysis of the angular distri-

bution of electrons that are emitted in the K-shell ionization of (initially) hydrogen atoms by (twisted) electromagnetic Bessel waves. In particular, we analyzed how the position of the atom within the wave front of the incoming light beam may affect the emission pattern of the photoelectrons. Our results show that for *paraxial* light beams with rather low energies ($E_\gamma \approx 100\,\mathrm{eV}$), it is only the *azimuthal* phase and not the intensity structure of the twisted light beam that may influence the emission process of the electrons. Such an azimuthal phase factor originates from the longitudinal TAM of the light beam and may strongly affect the emission pattern of the electrons if the atom is placed near to the (vortex) center of such a paraxial beam. However, if the atom is placed far away from the (central) vortex line, $b > 100\,\mathrm{a.u.}$, the paraxial twisted light beam behaves like an "ordinary" plane wave and, hence, the emission pattern of the photoelectrons resembles the one for the plane wave photoeffect.

Moreover, we found that if we depart from the paraxial beam regime and turn to larger opening angles $\theta_p > 1^\circ$, the length scale of the oscillations in the intensity pattern of the twisted photon beam may be of the same order than the extension of the atomic K-shell. In this case, additionally to its azimuthal phase, the intensity oscillations of the light beam may affect the emission process of the photoelectrons. Since these (short-scale) oscillations occur everywhere within the transverse beam profile, an atom may "feel" such intensity oscillations regardless of its position within the beam's wavefront, that is, even when it is placed far away from the beam center. Hence, in the non-paraxial beam regime, the emission pattern of the electrons can be strongly influenced by the transverse structure of the beam's intensity profile—even for large (atomic) impact parameters $b \approx 10\,000\,\mathrm{a.u.}$ with respect to the beam center.

The electron (probability) distribution for the K-shell of a hydrogen-like ion is spherically symmetric. To study the RR process with twisted photons for an atomic system that has a more complex structure of its electron cloud, we employed the strongly oriented $2p_y$-level of a hydrogen atom. Our analysis showed that the structure of this bound state will be strongly reflected by the emission pattern of the photoelectrons and can lead to a pronounced axial distribution of the electrons even if the atom is placed within the (twisted) beam center—a behaviour that is completely different from the K-shell ionization process. For this central case , $b = 0\,\mathrm{a.u.}$, and even the non-central case, $b > 0\,\mathrm{a.u.}$, the emission pattern of the electrons can again be considerably influenced by the azimuthal phase structure of the twisted beam as caused by its longitudinal TAM.

Apart from the atomic ionization with twisted photons, we used our formalism to investigate the radiative capture of twisted electrons into the K-shell of (finally) hydrogen atoms. In particular, we focused here on a scenario where a *macroscopic* proton beam with a transverse Gaussian density distribution collided head-on with a twisted electron beam; for this case, we analyzed the properties—angular distribution and polarization in terms of Stokes parameters—of the emitted photons. Our results illustrated that both, the emission pattern and the polarization state of the

emitted photons, can be considerably affected by varying the opening angle θ_p of the momentum cone of the incoming twisted electron beam. In the *paraxial* beam regime, where the twisted electrons behave nearly like "ordinary" plane waves, the angular distribution followed a $\sin^2\theta_k$-law, whereas only the first Stokes parameter was non-zero ($P_1 = 1$) while the other parameters vanished—a behaviour that is characteristic for the recombination process with plane wave electrons. In the non-paraxial beam regime, however, the emission pattern shows a completely different behaviour: whereas the probability (almost) vanishes in the paraxial regime to emit the photons in the forward ($\theta_k = 0$) and backward ($\theta_k = 180°$) directions, the photon distribution for the capture of non-paraxial twisted electrons shows that a considerable amount of light can be detected in these (on-axis) directions. Moreover, in contrast to the paraxial regime, the first Stokes parameter P_1 is significantly reduced for all emission angles of the photons. Such a reduction of the parameter P_1 can easily be measured by state-of-the-art polarization detectors and allows, therefore, to control the kinematic properties of the twisted electron beam.

For an electron beam that is in a *pure state* with a well-defined longitudinal OAM and that collides with a *macroscopic* ion target, the photon properties were found to be insensitive to the OAM state of the beam. To overcome such an insensitivity, we turned to a different scenario where—instead of a pure OAM state—a superposition of two twisted electron beams with different longitudinal OAM has been used. For this scenario, it was seen that the properties of the emitted photons can be strongly affected by an interference between the two beams during the RR process. The magnitude of this interference effect, however, strongly depends on the topological charges m_1 and m_2 of the two beams as well as on their kinematic parameters such as the opening angle θ_p of the momentum cone: while the angular distribution as well as the Stokes parameters may exhibit a pronounced OAM-dependency if two non-paraxial twisted beams with topological charges $m_1 = 0$ and $m_2 = \pm 1$ or $m_2 = \pm 2$ are superimposed, such OAM-effects vanish if we turn to the paraxial beam regime or if we increase the value of the topological charge $m_2 > 2$ of the second beam. With the end of this paragraph we have finished the summary of the present work, so that we can proceed now with an outlook on possible, future studies.

Outlook—As an outlook, let us discuss in the following a number of promising, future studies that may be performed by employing (and extending) our theoretical formalism. In the first part of the present work, we were concerned with analyzing the ionization process of *hydrogen-like ions* by twisted photons. By exploring the photoeffect with twisted light for such simple atomic systems, we were able to gain valuable insights into the underlying physics, in particular, how the novel properties of the twisted photon beam such as its longitudinal OAM or transverse momentum may affect the emission of the photoelectrons. Additional information on this ionization process can be obtained by exploiting more complex systems such as few- and many-electron ions (or atoms) as well as molecules. To describe the ionization

of such complex systems would require two major changes within our formalism: (a) the (initial) electronic bound state should characterize the (multi-electron) atomic or molecular system and (b) the initial (bound) as well as final (plane wave) electron states should respect the (multi-electron) Fock space structure, that is, the associated wave functions should be constructed as anti-symmetric Slater determinants. However, the complex structure of the bound state wave function for many-electron atomic and molecular systems makes it often impossible to analyze the corresponding ionization process in an analytical way and, hence, one has to rely on advanced *numerical methods*. A well-established method, for example, to obtain the wave functions for the bound states of many-electron atoms or ions is given by the multi-configuration Hartree-Fock formalism [126–129]. Molecular bound states, moreover, may be accurately calculated by using the method of linear combination of atomic orbitals (LCAO) and its further developments [130–132]. Which effects may we expect from the ionization process by twisted photons of such complex systems? Let us illustrate one of the possible effects that may occur for a diatomic molecule, e.g. H_2, N_2, or O_2, whose center of mass is positioned on the (vortex) axis of a twisted photon beam, and where the "atomic arms" of the molecules are oriented perpendicular to the beam's propagation direction. For this geometrical setup, each of the atoms that compose the molecule "sees" a different phase of the photon beam during the ionization process. Similar to the famous double-slit experiment of Young [133, 134] (i.e. each of the arms behaves like one of the slits), such a coherent ionization of the two atomic arms may lead to pronounced interference effects which may be seen in the angular distribution of the emitted electrons and which may crucially depend on the helical phase structure of the twisted light beam.

Both processes—ionization of hydrogen-like ions by twisted photons and radiative capture of twisted electrons by bare ions—have been treated here within the non-relativistic regime, that is, for low nuclear charges of the ions ($Z \leq 25$) and low kinetic energies of the emitted or incident electrons (up to a few keV). In such a regime it is sufficient to characterize the continuum and bound electron states by the (non-relativistic) Schrödinger equation. To obtain a relativistic description of both processes that is valid for larger nuclear charges and electron energies, one should employ the *Dirac equation*, instead of the Schrödinger equation, to describe the (bound and continuum) electron states [135, 136]. The hydrogenic bound states as well as (distorted) plane wave states of electrons are well-known within the Dirac formalism [135, 136]. In addition, solutions of the Dirac equation describing (freely-propagating) twisted electrons have been developed recently [137–139]. We must note, however, that these twisted electron states have been obtained within the vacuum (or inside a laser field), i.e. they do not incorporate the Coulombic distortion that can be caused by (hydrogenic) ions with a large nuclear charge Z. With respect to the RR process, therefore, one has to generalize these twisted electron waves in order to account for the Coulombic interaction with the target ions that occurs before

the radiative capture process. Beside the relativistic form of the bound and continuum electron states, it is also necessary to turn to the relativistic description of the electromagnetic interaction operator, that is, instead of using the operator $\mathbf{p} \cdot \mathbf{A}$ as done in the present work, one should employ the (relativistic) operator $\boldsymbol{\alpha} \cdot \mathbf{A}$, where $\boldsymbol{\alpha} = (\alpha_1, \alpha_2, \alpha_3)^T$ is a vector consisting of Dirac α-matrices [135, 136]. Altogether, by using the relativistic forms of the electron wave functions and the electromagnetic interaction operator, an analysis of the ionization and recombination process with twisted photons and electrons, respectively, can be performed even for high-Z ions and large kinetic energies of the emitted and incident electrons.

Apart from the atomic ionization by twisted photons and the radiative capture of twisted electrons by ions, there exist other (collision) processes that can be studied (and may be better understood) by utilizing twisted beams. An important process that may provide valuable insights on the fundamental role of the OAM in particle collisions is the (elastic or inelastic) scattering of a particle beam on some target sample. First studies in this direction have already been performed by Ivanov and coworkers in Refs. [140–143], where cross sections for different (twisted) beam-beam collision scenarios have been analyzed. In these investigations it has been shown, for example, that the elastic scattering of a twisted Bessel beam on a counter-propagating plane wave may lead to the formation of two OAM-entangled outgoing beams. Coulombic scattering of twisted electrons on a hydrogen atom has been discussed by Lloyd *et al.* [63,64]. In this study it was found that such an electron-atom scattering may lead to an OAM exchange between the twisted electron beam and (a) the bound state electrons as well as (b) the (overall) center of mass motion of the atom; moreover, selection rules for the OAM exchange in such a collision process have been derived. A still outstanding task is to develop a simple theoretical formalism that can describe the (angle-differential) cross sections for the scattering of charged twisted particle beams on arbitrary scalar potentials. Such a formalism would have the great advantage to be applicable to a large number of different problems such as, for example, the scattering of twisted electron beams on molecules, where the molecular structure is described by an effective scalar potential. To establish the theoretical framework for this *potential scattering* of twisted particle beams, one would proceed similar as for the "standard" potential scattering of plane wave beams [71, 144], that is, one would need to re-derive the so-called *S-matrix elements* (or scattering amplitudes), but taken now for an incoming twisted particle beam. We note that such a derivation of the "twisted" S-matrix elements can be achieved by combining the plane wave expansion of the twisted particle states (cf. Eq. (3.10)) with the (well-known) S-matrix elements for the case of plane wave scattering [71, 144]. With the help of the (twisted) S-matrix elements, one can then describe all observables of the potential scattering process with twisted particles such as, for example, the corresponding (angle-differential) cross sections.

Having provided a comprehensive summary of our work and an account on possible future studies, let us finally conclude this thesis with a brief closing remark. In the present work, we performed a detailed analysis of both, the ionization of hydrogen-like ions by twisted photons as well as the radiative capture of twisted electrons by bare ions, and showed that the behaviour of the emitted electrons and photons in these processes may be significantly affected by the novel properties of the incoming twisted particle beams such as their transverse momentum or their OAM along the propagation direction. We established, moreover, not only the basic theoretically description of this behaviour in the form of concise analytical formulas but we also explained how the occurring effects are caused by the internal properties of the twisted particle beams. The present theoretical study may serve, therefore, as a guideline for the design of novel experiments that aim at accessing the properties of a twisted particle beam within the atomic regime.

Appendix

A. Helicity Eigenstates: Polarization Vector

Here we will show that the polarization vector of a plane electromagnetic wave with helicity $\lambda = \pm 1$ has the following form

$$\mathbf{e}_{\mathbf{p}\lambda} = \frac{-\lambda}{\sqrt{2}} \begin{pmatrix} \cos\theta_p \cos\varphi_p - \mathrm{i}\,\lambda \sin\varphi_p \\ \cos\theta_p \sin\varphi_p + \mathrm{i}\,\lambda \cos\varphi_p \\ -\sin\theta_p \end{pmatrix}. \tag{A.1}$$

As was mentioned in Sec. 2.2, the polarization vectors (A.1) should derive from the eigenvalue problem

$$\widehat{\Lambda}\,\widetilde{\mathbf{A}}(\mathbf{p},\omega) = \lambda\,\widetilde{\mathbf{A}}(\mathbf{p},\omega), \tag{A.2}$$

or correspondingly

$$\widehat{\Lambda}\,\mathbf{e}_{\mathbf{p}\lambda} = \lambda\,\mathbf{e}_{\mathbf{p}\lambda}, \tag{A.3}$$

where $\widehat{\Lambda}$ is the helicity operator as given by Eq. (2.29). In spherical coordinates

$$p = \sqrt{p_x^2 + p_y^2 + p_z^2}, \quad \varphi_p = \arctan(p_y/p_x), \quad \theta_p = \arccos(p_z/p), \tag{A.4}$$

the helicity operator can be written as

$$\widehat{\Lambda} = \mathrm{i} \begin{pmatrix} 0 & -\cos\theta_p & \sin\varphi_p \sin\theta_p \\ \cos\theta_p & 0 & -\cos\varphi_p \sin\theta_p \\ -\sin\varphi_p \sin\theta_p & \cos\varphi_p \sin\theta_p & 0 \end{pmatrix}. \tag{A.5}$$

By standard algebraic methods [145], we can find the properly normalized eigenvectors and the corresponding eigenvalues to problem (A.3) as

$$\mathbf{e}_{\mathbf{p},\lambda=\pm1} = \frac{-\lambda}{\sqrt{2}} \begin{pmatrix} \cos\theta_p \cos\varphi_p - \mathrm{i}\lambda \sin\varphi_p \\ \cos\theta_p \sin\varphi_p + \mathrm{i}\lambda \cos\varphi_p \\ -\sin\theta_p \end{pmatrix}, \ \lambda = \pm 1, \tag{A.6}$$

$$\mathbf{e}_{\mathbf{p},\lambda=0} = \begin{pmatrix} \sin\theta_p \cos\varphi_p \\ \sin\theta_p \sin\varphi_p \\ \cos\theta_p \end{pmatrix}, \ \lambda = 0. \tag{A.7}$$

But the vector $\mathbf{e}_{\mathbf{p},\lambda=0}$ with eigenvalue $\lambda = 0$ fails to fulfill the transversality condition (2.26), i.e.

$$\mathbf{p} \cdot \mathbf{e}_{\mathbf{p},\,\lambda=0} \neq 0, \tag{A.8}$$

and, hence, cannot serve for the description of a polarization state. Only the vectors with eigenvalues $\lambda = \pm 1$ comply with the transversality condition:

$$\begin{aligned} \mathbf{p} \cdot \mathbf{e}_{\mathbf{p},\,\lambda=\pm\mathbf{1}} &= \frac{-p\,\lambda}{\sqrt{2}} \begin{pmatrix} \cos\varphi_p \sin\theta_p \\ \sin\varphi_p \sin\theta_p \\ \cos\theta_p \end{pmatrix} \cdot \begin{pmatrix} \cos\theta_p \cos\varphi_p - i\lambda \sin\varphi_p \\ \cos\theta_p \sin\varphi_p + i\lambda \cos\varphi_p \\ -\sin\theta_p \end{pmatrix} \\ &= \frac{-p\,\lambda}{\sqrt{2}} \left(\cos\theta_p \sin\theta_p \cos^2\varphi_p + \cos\theta_p \sin\theta_p \sin^2\varphi_p - \cos\theta_p \sin\theta_p\right) \\ &= 0, \end{aligned} \tag{A.9}$$

and can therefore be used for the description of a polarization state.

B. Optical Pumping of Hydrogen-Like Ions into $2p_y$-Level

In this part, we will show that it is possible to populate the $2p_y$-level of a hydrogen-like from the ground state by optical pumping with linearly polarized light. A complete basis of the magnetic substates of the hydrogen-like levels with $n = 2$ and $l = 1$ is given by

$$\psi_{2p_x}(\mathbf{r}) = \frac{1}{\sqrt{2}}\big(\psi_{2,1,1}(\mathbf{r}) - \psi_{2,1,-1}(\mathbf{r})\big), \tag{B.1}$$

$$\psi_{2p_y}(\mathbf{r}) = \frac{1}{\sqrt{2}\mathrm{i}}\big(\psi_{2,1,1}(\mathbf{r}) + \psi_{2,1,-1}(\mathbf{r})\big), \tag{B.2}$$

$$\psi_{2p_z}(\mathbf{r}) = \psi_{2,1,0}(\mathbf{r}). \tag{B.3}$$

The states (B.1)–(B.3) are normalized as

$$\int |\psi_{2p_x}(\mathbf{r})|^2 \, \mathrm{d}^3\mathbf{r} = \int \left|\psi_{2p_y}(\mathbf{r})\right|^2 \, \mathrm{d}^3\mathbf{r} = \int |\psi_{2p_z}(\mathbf{r})|^2 \, \mathrm{d}^3\mathbf{r} = 1 \tag{B.4}$$

and are mutually orthogonal.

To demonstrate that the $2p_y$-state can be populated from the ground state of a hydrogen-like ion by absorption of light with a linear polarization along the y-axis, we calculate the corresponding transition amplitudes within the dipole approximation:

$$M_{fi} = -\int \psi^*_{2p_y}(\mathbf{r}) \; (\mathbf{e}_y \cdot \mathbf{r}) \, \psi_{1,0,0}(\mathbf{r}) \, \mathrm{d}^3\mathbf{r}, \tag{B.5}$$

where

$$\mathbf{e}_y = (0, 1, 0)^T \tag{B.6}$$

represents the polarization vector of the light that points along the y-axis. If we write

$$(\mathbf{e}_y \cdot \mathbf{r}) = r\, \sin\varphi_r \sin\theta_r = \mathrm{i}\sqrt{\frac{2\pi}{3}}\, r\, \left(Y_{1,1}(\theta_r, \varphi_r) + Y_{1,-1}(\theta_r, \varphi_r)\right), \tag{B.7}$$

we obtain for the transition matrix elements (B.5):

$$\begin{aligned} M_{fi} = \frac{1}{2}\sqrt{\frac{1}{3}} \int g_{21}(r)\, r^3\, g_{10}(r)\, \mathrm{d}r \\ \times \int \Big(Y^*_{1,1}(\theta_r, \varphi_r)\, Y_{1,1}(\theta_r, \varphi_r) + Y^*_{1,1}(\theta_r, \varphi_r)\, Y_{1,-1}(\theta_r, \varphi_r) \\ + Y^*_{1,-1}(\theta_r, \varphi_r)\, Y_{1,1}(\theta_r, \varphi_r) + Y^*_{1,-1}(\theta_r, \varphi_r)\, Y_{1,-1}(\theta_r, \varphi_r) \Big)\, \mathrm{d}\Omega_r. \end{aligned} \tag{B.8}$$

With the orthogonality relation of the spherical harmonics

$$\int Y^*_{l,m}(\theta_r, \varphi_r)\, Y_{l',m'}(\theta_r, \varphi_r)\, \mathrm{d}\Omega_r = \delta_{ll'}\delta_{mm'}, \tag{B.9}$$

one can directly solve the angular integral in Eq. (B.8) so that

$$M_{fi} = \sqrt{\frac{1}{3}} \int g_{21}(r)\, r^3\, g_{10}(r)\, \mathrm{d}r. \tag{B.10}$$

Expression (B.10) can be further evaluated if one plugs in the exact form of the radial wave functions as given by Eq. (3.15). After solving the integral (B.10), one obtains

$$M_{fi} = \sqrt{2}\, \frac{128}{243}\, \frac{1}{Z}. \tag{B.11}$$

Since the transition amplitude (B.11) is *non-zero* the transition from the ground state to $2p_y$-level is allowed in the electric dipole approximation.

In a similar fashion as above and again for a light beam with linear polarization along the y-axis, one can calculate the transition elements for the excitation to the $2p_x$ or $2p_z$ levels. For both states, one obtains that such a transition is forbidden within the dipole approximation. Thus, plane electromagnetic waves with linear polarization along the y-axis populate only the $2p_y$-state.

C. Transition Amplitudes for Atomic Photoionization by Twisted Photons

In this part of the Appendix, we will calculate the transition matrix elements, as given by Eq. (5.12), for the photoionization process by Bessel light beams. These calculations have already been performed in detail in our article [68] and therefore we have decided to include this passage here (nearly) word-by-word from our article. Similar to the ionization by plane wave photons, any analysis of the electron emission induced by the incident twisted light requires the knowledge of the transition amplitude (5.12). As discussed in Sec. 5.2, this amplitude can be written, upon the Fourier transformation of the bound-state wavefunction, in the form (5.12). In order to proceed further, we insert the explicit expression (3.20) of $\widetilde{\psi}_{nlm}(\mathbf{p}-\mathbf{k})$ into Eq. (5.12) and find

$$M_{fi}^{\rm tw}(\theta_p,\varphi_p) = c_{\rm tw}\int_0^{2\pi} {\rm e}^{{\rm i}m_\gamma\varphi_k}\,{\rm e}^{-{\rm i}\mathbf{b}_\perp\cdot\mathbf{q}}\,q^l\,\frac{(\mathbf{e}_{k\Lambda}\cdot\mathbf{p})}{(q^2+\delta^2)^{l+2}}\,C_{n-l-1}^{l+1}\left(\frac{q^2-\delta^2}{q^2+\delta^2}\right)\,Y_{lm}(\theta_q,\varphi_q)\,{\rm d}\varphi_k\,, \tag{C.1}$$

where $\mathbf{q}=\mathbf{p}-\mathbf{k}$ and the prefactor $c_{\rm tw}$ is given by

$$c_{\rm tw} = (-{\rm i})^{m_\gamma+l}\,2^{2l+2}\,n^{-l-2}\,Z^{l+4}\,l!\,\sqrt{\frac{2\varkappa\,(n-l-1)!}{\pi Z^3(n+l)!}}\,. \tag{C.2}$$

It follows from these formulas, that the computation of the transition amplitude $M_{fi}^{\rm tw}(\theta_p,\varphi_p)$ is reduced to an integration over the azimuthal angle φ_k. To perform such an integration *analytically* we need to re-write the integrand in the right-hand side of Eq. (C.1) in such a way that its φ_k-dependence becomes explicit. We start from the product of the polarization $\mathbf{e}_{\mathbf{k}\lambda}$ and the momentum $\mathbf{p}$ vectors which can be simplified to

$$(\mathbf{e}_{\mathbf{k}\lambda}\cdot\mathbf{p}) = \frac{p_\perp}{\sqrt{2}}\,c_{-1}(\lambda,\theta_k)\,{\rm e}^{{\rm i}(\varphi_k-\varphi_p)} + p_z\,c_0(\lambda,\theta_k) - \frac{p_\perp}{\sqrt{2}}\,c_{+1}(\lambda,\theta_k)\,{\rm e}^{-{\rm i}(\varphi_k-\varphi_p)} \tag{C.3}$$

with

$$p_\perp = p\sin\theta_p, \quad p_z = p\cos\theta_p\,. \tag{C.4}$$

As a second step, we shall expand the spherical harmonics $Y_{lm}(\theta_q,\varphi_q)$ in terms of $Y_{\sigma\mu}(\theta_k,\varphi_k)$. To perform this expansion, we introduce the solid spherical harmonics:

$$\mathcal{R}_{lm}(\mathbf{r}) = \sqrt{\frac{4\pi}{2l+1}}\, r^l\, Y_{lm}(\theta_r,\varphi_r), \tag{C.5}$$

for which the following addition theorem [146] holds

$$\mathcal{R}_{lm}(\mathbf{r}+\mathbf{a}) = \sum_{\sigma=0}^{l}\sum_{\mu=-\sigma}^{\sigma}\binom{2l}{2\sigma}^{1/2}\langle\sigma,\mu;l-\sigma,m-\mu|lm\rangle\,\mathcal{R}_{\sigma\mu}(\mathbf{r})\,\mathcal{R}_{l-\sigma,m-\mu}(\mathbf{a})\,, \tag{C.6}$$

where $\langle ...|...\rangle$ is a Clebsch-Gordan coefficient and $\mathbf{a}$ is some displacement vector. By writing

$$q^l\, Y_{lm}(\theta_q,\varphi_q) = \sqrt{\frac{2l+1}{4\pi}}\,\mathcal{R}_{lm}(\mathbf{q}) \tag{C.7}$$

with

$$\mathbf{q} = \mathbf{p} - \mathbf{k} \tag{C.8}$$

and applying Eq. (C.6), we obtain

$$\begin{aligned} q^l\; Y_{lm}(\theta_q,\varphi_q) = &\sum_{\sigma=0}^{l}\sum_{\mu=-\sigma}^{\sigma}\binom{2l}{2\sigma}^{1/2}\sqrt{\frac{4\pi(2l+1)}{(2\sigma+1)(2(l-\sigma)+1)}} \\ &\times(-1)^{l-\sigma}p^\sigma k^{l-\sigma}\,\langle\sigma,\mu;l-\sigma,m-\mu|lm\rangle\,Y_{\sigma\mu}(\theta_p,\varphi_p)Y_{l-\sigma,m-\mu}(\theta_k,\varphi_k)\,. \end{aligned} \tag{C.9}$$

By re-writing the spherical harmonics $Y_{l-\sigma,m-\mu}(\theta_k,\varphi_k)$ in this expression in terms of $\mathrm{e}^{\mathrm{i}(m-\mu)\varphi_k}$, we get

$$q^l\; Y_{lm}(\theta_q,\varphi_q) = \sum_{\sigma=0}^{l}\sum_{\mu=-\sigma}^{\sigma} h_{\sigma\mu}(\theta_p,\varphi_p)\,\mathrm{e}^{\mathrm{i}(m-\mu)\varphi_k} \tag{C.10}$$

with

$$h_{\sigma\mu}(\theta_p,\varphi_p) = \sqrt{\frac{2l+1}{2\sigma+1}}\sqrt{\frac{(l-\sigma-m+\mu)!}{(l-\sigma+m-\mu)!}}\binom{2l}{2\sigma}^{1/2}(-1)^{l-\sigma}p^{\sigma}k^{l-\sigma} \\ \times \langle\sigma,\mu;l-\sigma,m-\mu|lm\rangle\, Y_{\sigma\mu}(\theta_p,\varphi_p)P_{l-\sigma,m-\mu}(\cos\theta_k)\,. \tag{C.11}$$

Having deduced the explicit φ_k-dependence of the product $(\mathbf{e}_{\mathbf{k}\lambda}\cdot\mathbf{p})$ and of the expression $q^l\,Y_{lm}(\theta_q,\varphi_q)$ from Eq. (C.1), it remains to perform the Fourier expansion

$$\frac{1}{(q^2+\delta^2)^{l+2}}\,C^{l+1}_{n-l-1}\left(\frac{q^2-\delta^2}{q^2+\delta^2}\right) = \sum_{\nu=-\infty}^{\infty} f_\nu(\theta_p,\varphi_p)\,\mathrm{e}^{\mathrm{i}\nu\varphi_k}, \tag{C.12}$$

of the Gegenbauer polynomial $C^{l+1}_{n-l-1}(x)$ divided by some polynomial. In order to compute the expansion coefficients

$$f_\nu(\theta_p,\varphi_p) = \frac{1}{2\pi}\int_0^{2\pi}\frac{1}{(q^2+\delta^2)^{l+2}}\,C^{l+1}_{n-l-1}\left(\frac{q^2-\delta^2}{q^2+\delta^2}\right)\mathrm{e}^{-\mathrm{i}\nu\varphi_k}\,\mathrm{d}\varphi_k\,, \tag{C.13}$$

we write the Gegenbauer polynomials explicitly [108] as

$$C^{l+1}_{n-l-1}\left(\frac{q^2-\delta^2}{q^2+\delta^2}\right) = \sum_{\eta=0}^{\lfloor(n-l-1)/2\rfloor} t_\eta\left(\frac{q^2-\delta^2}{q^2+\delta^2}\right)^{n-l-1-2\eta}, \tag{C.14}$$

where $\lfloor x\rfloor$ is the largest integer not greater than x and

$$t_\eta = 2^{n-l-1-2\eta}\frac{(-1)^\eta\;(n-\eta-1)!}{\eta!\;l!\;(n-l-1-2\eta)!}\,. \tag{C.15}$$

By inserting Eq. (C.14) into (C.13) we find the Fourier expansion coefficients in the form

$$f_\nu(\theta_p,\varphi_p) = \frac{1}{2\pi}\sum_{\eta=0}^{\lfloor(n-l-1)/2\rfloor} t_\eta\int_0^{2\pi}\frac{(q^2-\delta^2)^{n-l-1-2\eta}}{(q^2+\delta^2)^{n+1-2\eta}}\mathrm{e}^{-\mathrm{i}\nu\varphi_k}\,\mathrm{d}\varphi_k\,. \tag{C.16}$$

In order to compute the integral from above, we perform the substitution $\varphi_k \to \varphi_p - \varphi_k$ and introduce the new (integration) variable

$$z = \mathrm{e}^{\mathrm{i}\varphi_k}\,, \tag{C.17}$$

and, hence, re-write (C.16) as

$$f_\nu(\theta_p, \varphi_p) = \frac{-\mathrm{i}}{2\pi}\,\alpha^{-l-2}\,\mathrm{e}^{-\mathrm{i}\nu\varphi_p} \sum_{\eta=0}^{\lfloor (n-l-1)/2 \rfloor} t_\eta \int_\chi g_{\eta\nu}(z)\,\mathrm{d}z\,. \tag{C.18}$$

Here, the integration contour χ is the complex unit circle, and the function $g_{\eta\nu}(z)$ is given by

$$g_{\eta\nu}(z) = z^{\nu+l+1}(z-z_1)^{n-l-1-2\eta}(z-z_2)^{n-l-1-2\eta}(z-z_3)^{-n-1+2\eta}(z-z_4)^{-n-1+2\eta}\,, \tag{C.19}$$

with

$$\alpha = -p_\perp \varkappa, \tag{C.20}$$

$$z_1 = (2p_\perp\varkappa)^{-1}\left[p^2+k^2-\delta^2-2p_zk_z+\sqrt{(p^2+k^2-\delta^2-2p_zk_z)^2-4p_\perp^2\varkappa^2}\,\right], \tag{C.21}$$

$$z_2 = (2p_\perp\varkappa)^{-1}\left[p^2+k^2-\delta^2-2p_zk_z-\sqrt{(p^2+k^2-\delta^2-2p_zk_z)^2-4p_\perp^2\varkappa^2}\,\right], \tag{C.22}$$

$$z_3 = (2p_\perp\varkappa)^{-1}\left[p^2+k^2+\delta^2-2p_zk_z+\sqrt{(p^2+k^2+\delta^2-2p_zk_z)^2-4p_\perp^2\varkappa^2}\,\right] \tag{C.23}$$

and

$$z_4 = (2p_\perp\varkappa)^{-1}\left[p^2+k^2+\delta^2-2p_zk_z\sqrt{(p^2+k^2+\delta^2-2p_zk_z)^2-4p_\perp^2\varkappa^2}\,\right]. \tag{C.24}$$

As seen from Eq. (C.19), the $g_{\eta\nu}(z)$ is a rational function with poles at $z = 0$ and $z = z_4$ in the unit circle of order $-\nu - l - 1$ and $n + 1 - 2\eta$, respectively. We can

use, therefore, the residue theorem [119] to calculate the integral over z in Eq. (C.18) analytically

$$f_\nu(\theta_p\,,\varphi_p) = \mathrm{e}^{-\mathrm{i}\nu\varphi_p}\alpha^{-l-2}\sum_{\eta=0}^{\lfloor (n-l-1)/2\rfloor} t_\eta\ \left(\mathrm{Res}(g_{\eta\nu},0) + \mathrm{Res}(g_{\eta\nu},z_4)\right)\,, \tag{C.25}$$

where

$$\mathrm{Res}(g_{\eta\nu},z_{\mathrm{pole}}) = \frac{1}{(k-1)!}\lim_{z\to z_{\mathrm{pole}}}\frac{\partial^{k-1}}{\partial z^{k-1}}(z-z_{\mathrm{pole}})^k g_{\eta\nu}(z), \tag{C.26}$$

and k is the order of the pole z_{pole}. By inserting the function $g_{\eta\nu}(z)$ into the right-hand side of Eq. (C.26) and evaluating the derivative for the two poles $z=0$ and $z=z_4$, we finally obtain

$$\begin{aligned}
\mathrm{Res}(g_{\eta\nu},0) = {} & \frac{1}{(-\nu-l-2)!}\sum_{i_0=0}^{-\nu-l-2}\ \sum_{i_1=0}^{-\nu-l-2-i_0}\ \sum_{i_2=0}^{-\nu-l-2-i_0-i_1}(-1)^{\nu-l-2}\binom{-\nu-l-2}{i_0} \\
& \times \binom{-\nu-l-2-i_0}{i_1}\binom{-\nu-l-2-i_0-i_1}{i_2}(n-l-1-2\eta)_{i_0} \\
& \times (n-l-1-2\eta)_{i_1}\,(-n-1+2\eta)_{i_2}\,(-n-1+2\eta)_{-\nu-l-2-i_0-i_1-i_2} \\
& \times z_1^{n-l-1-2\eta-i_0}\,z_2^{n-l-1-2\eta-i_1}\,z_3^{-n-1+2\eta-i_2}\,z_4^{-n+1+2\eta+\nu+l+i_0+i_1+i_2}\,,
\end{aligned} \tag{C.27}$$

and

$$\begin{aligned}
\mathrm{Res}(g_{\eta,\nu},z_4) = {} & \frac{1}{(n-2\eta)!}\sum_{i_0=0}^{n-2\eta}\ \sum_{i_1=0}^{n-2\eta-i_0}\ \sum_{i_2=0}^{n-2\eta-i_0-i_1}\binom{n-2\eta}{i_0}\binom{n-2\eta-i_0}{i_1} \\
& \times \binom{n-2\eta-i_0-i_1}{i_2}(\nu+l+1)_{i_0}(n-l-1-2\eta)_{i_1} \\
& \times (n-l-1-2\eta)_{i_2}(-n-1+2\eta)_{n-2\eta-i_0-i_1-i_2}\,z_4^{\nu+l+1-i_0} \\
& \times (z_4-z_1)^{n-l-1-2\eta-i_1}(z_4-z_2)^{n-l-1-2\eta-i_2}(z_4-z_3)^{-2n-1+4\eta+i_0+i_1+i_2}\,,
\end{aligned} \tag{C.28}$$

where $(x)_j = x\,(x-1)\,(x-2)\ldots(x-j)$ is the falling factorial. With the help of Eqs. (C.25)-(C.28) one may evaluate the expansion coefficients $f_\nu(\theta_p,\varphi_p)$ that enter the Fourier expansion (C.12). Numerical analysis of these coefficients has shown, moreover, that for the ground and low-lying excited atomic states and for small

photon energies ($\approx 100\,\mathrm{eV}$), the summation over ν in Eq. (C.12) may be restricted just to terms with $|\nu| \lesssim 3$.

After separate evaluation of the three parts of the integrand in Eq. (C.1), we are ready now to compute the matrix element $M_{fi}^{\mathrm{tw}}(\theta_p, \varphi_p)$. That is, by inserting Eqs. (C.3), (C.10) and (C.12) in the right-hand side of Eq. (C.1), we find

$$M_{fi}^{\mathrm{tw}}(\theta_p, \varphi_p) = c_{\mathrm{tw}} \sum_{\sigma=0}^{l} \sum_{\mu=-\sigma}^{\sigma} \sum_{\nu=-\infty}^{\infty} \int_0^{2\pi} h_{\sigma\mu}(\theta_p, \varphi_p) f_\nu(\theta_p, \varphi_p)\, \mathrm{e}^{\mathrm{i}(m_\gamma + m + \nu - \mu)\varphi_k}\, \mathrm{e}^{-\mathrm{i}\mathbf{b}_\perp \mathbf{q}} \times \left(\frac{p_\perp}{\sqrt{2}}\, c_{-1}(\lambda, \theta_k)\, \mathrm{e}^{-\mathrm{i}(\varphi_p - \varphi_k)} + p_z\, c_0(\lambda, \theta_k) - \frac{p_\perp}{\sqrt{2}}\, c_{+1}(\lambda, \theta_k)\, \mathrm{e}^{\mathrm{i}(\varphi_p - \varphi_k)} \right) \mathrm{d}\varphi_k \,. \tag{C.29}$$

We further utilize the well-known integral representation [108] of the Bessel functions

$$\int_0^{2\pi} \mathrm{e}^{\mathrm{i}l\varphi} \mathrm{e}^{\mathrm{i}x\cos(\phi - \varphi)} \mathrm{d}\varphi = 2\pi\, \mathrm{i}^l\, \mathrm{e}^{\mathrm{i}l\phi} J_l(x) \,, \tag{C.30}$$

to analytically perform the integration over the φ_k-angle in Eq. (C.29), and to yield finally the general expression

$$\begin{aligned} M_{fi}^{\mathrm{tw}}(\theta_p, \varphi_p) = {} & 2\pi\, c_{\mathrm{tw}} \sum_{\sigma=0}^{l} \sum_{\mu=-\sigma}^{\sigma} \sum_{\nu=-\infty}^{\infty} h_{\sigma,\mu}(\theta_p, \varphi_p) f_\nu(\theta_p, \varphi_p) \\ & \times\ \mathrm{i}^{m_\gamma + m + \nu - \mu}\, \mathrm{e}^{-\mathrm{i}\mathbf{b}_\perp \cdot \mathbf{p}}\, \mathrm{e}^{\mathrm{i}(m_\gamma + m + \nu - \mu)\varphi_b} \\ & \times\ \Big(\mathrm{i}\, \frac{p_\perp}{\sqrt{2}}\, c_{-1}\, \mathrm{e}^{-\mathrm{i}(\varphi_p - \varphi_b)}\, J_{m_\gamma + m + \nu - \mu + 1}(\varkappa b_\perp) + p_z\, c_0\, J_{m_\gamma + m + \nu - \mu}(\varkappa b_\perp) \\ & \quad + \mathrm{i}\, \frac{p_\perp}{\sqrt{2}}\, c_{+1}\, \mathrm{e}^{\mathrm{i}(\varphi_p - \varphi_b)}\, J_{m_\gamma + m + \nu - \mu - 1}(\varkappa b_\perp) \Big) \end{aligned} \tag{C.31}$$

for the amplitude that describes the bound-free electron transition in the field of the twisted (Bessel) light. In this expression, φ_b is the azimuthal angle of the impact parameter, which should be taken to be *zero* for the geometry used in the present study (cf. Fig. 5.2).

D. Evaluation of Density Matrix Averaged over Impact Parameter: Part A

Here we would like to show that one can reduce the density matrix (6.21) as given by

$$\langle \mathbf{k}\,\lambda|\widehat{\rho}_\gamma^{\rm tw}|\mathbf{k}\lambda'\rangle = \int f(\mathbf{b}_\perp)\, M^{{\rm tw},*}_{\varkappa m p_z \mathbf{b}_\perp}(\mathbf{k},\lambda)\, M^{\rm tw}_{\varkappa m p_z \mathbf{b}_\perp}(\mathbf{k},\lambda')\,{\rm d}^2\mathbf{b}_\perp \tag{D.1}$$

to the expression

$$\begin{aligned}\langle \mathbf{k}\lambda|\,\widehat{\rho}_\gamma^{\rm tw}\,|\mathbf{k}\lambda'\rangle = \int \exp\left[-2\varkappa^2\sigma_b^2\sin^2\left(\frac{\varphi_p-\varphi_p'}{2}\right)\right] \\ \times\, a^*_{\varkappa m}(\mathbf{p}_\perp)\, a_{\varkappa m}(\mathbf{p}'_\perp)\, M^{{\rm pl},*}_{\mathbf{p}}(\mathbf{k},\lambda)\, M^{\rm pl}_{\mathbf{p}'}(\mathbf{k},\lambda')\,{\rm d}^2\mathbf{p}_\perp {\rm d}^2\mathbf{p}'_\perp.\end{aligned} \tag{D.2}$$

By substituting the explicit form (6.19) of the transition amplitudes $M^{\rm tw}_{\varkappa m p_z \mathbf{b}_\perp}(\mathbf{k},\lambda)$ and (6.16) of the ion density distribution $f(\mathbf{b}_\perp)$ in expression (D.1), we obtain

$$\begin{aligned}\langle \mathbf{k}\,\lambda|\widehat{\rho}_\gamma|\mathbf{k}\lambda'\rangle = (2\pi\sigma_b^2)^{-1}\int {\rm e}^{-b^2/(2\sigma_b^2)}\,{\rm e}^{{\rm i}\mathbf{b}_\perp\cdot(\mathbf{p}'-\mathbf{p})}\, a^*_{\varkappa m p_z}(\mathbf{p})\, a_{\varkappa m p_z}(\mathbf{p}') \\ \times\, M^{{\rm pl},*}_{\mathbf{p}}(\mathbf{k},\lambda)\, M^{\rm pl}_{\mathbf{p}'}(\mathbf{k},\lambda')\,{\rm d}^3\mathbf{p}\,{\rm d}^3\mathbf{p}'\,{\rm d}^2\mathbf{b}_\perp.\end{aligned} \tag{D.3}$$

where the transverse and longitudinal momentum of $\mathbf{p}$ and $\mathbf{p}'$ in the integrand of Eq. (D.3) are fixed to $\varkappa$ and p_z by the functions $a_{\varkappa m p_z}(\mathbf{p})$. We focus now on the integral over $\mathbf{b}_\perp$ in expression (D.3) and define

$$\begin{aligned}\mathcal{I}(\mathbf{p},\mathbf{p}') &= (2\pi\sigma_b^2)^{-1}\int {\rm e}^{-b^2/(2\sigma_b^2)}\,{\rm e}^{{\rm i}\mathbf{b}_\perp\cdot(\mathbf{p}'-\mathbf{p})}{\rm d}^2\mathbf{b}_\perp \\ &= (2\pi\sigma_b^2)^{-1}\int_0^{2\pi}\int_0^\infty {\rm e}^{-b^2/(2\sigma_b^2)}\,{\rm e}^{{\rm i}\mathbf{b}_\perp\cdot(\mathbf{p}'-\mathbf{p})}\, b\,{\rm d}b\,{\rm d}\varphi_b,\end{aligned} \tag{D.4}$$

with

$$\mathbf{p} = (\varkappa \cos\varphi_p, \varkappa \sin\varphi_p, p_z)^T, \mathbf{p}' = (\varkappa \cos\varphi'_p, \varkappa \sin\varphi'_p, p_z)^T, \mathbf{b}_\perp = (b\cos\varphi_b, b\sin\varphi_b, 0)^T. \tag{D.5}$$

To perform the integration in Eq. (D.4), we first simplify parts of its integrand. Let us focus now on the second exponent in the integrand:

$$\begin{aligned} \mathbf{b}_\perp \cdot (\mathbf{p}' - \mathbf{p}) &= b\,\varkappa \left[\cos(\varphi'_p - \varphi_b) - \cos(\varphi_p - \varphi_b)\right] \\ &= -2\,b\,\varkappa \sin\left(\frac{\varphi'_p + \varphi_p}{2} - \varphi_b\right) \sin\left(\frac{\varphi'_p - \varphi_p}{2}\right), \end{aligned} \tag{D.6}$$

where we have used the following relation for the second equality [108]:

$$\cos\theta - \cos\varphi = -2\sin\left(\frac{\theta+\varphi}{2}\right)\sin\left(\frac{\theta-\varphi}{2}\right). \tag{D.7}$$

By using Eq. (D.6) and by employing the following representation of the zero-order Bessel functions [147, pp. 228–231]

$$\int_0^{2\pi} \mathrm{e}^{-\mathrm{i}x\sin\varphi} \mathrm{d}\,\varphi = 2\pi\, J_0(x) \tag{D.8}$$

we can perform the φ_b-integral in Eq. (D.6) with the result:

$$\mathcal{I}(\mathbf{p}, \mathbf{p}') = \sigma_b^{-2} \int_0^\infty \mathrm{e}^{-b^2/(2\sigma_b^2)} J_0\left(-2\,b\,\varkappa \sin\left(\frac{\varphi'_p - \varphi_p}{2}\right)\right) b\,\mathrm{d}b. \tag{D.9}$$

The integral (D.9) can be evaluated further by using the following integral of the zero-order Bessel functions [108, Sec. 11.4.28]

$$2a^2 \int_0^\infty r\,\mathrm{e}^{-a^2 r^2} J_0(kr)\,\mathrm{d}r = \mathrm{e}^{-\frac{k^2}{4a^2}}. \tag{D.10}$$

With the help of Eq. (D.10), we finally obtain

$$\mathcal{I}(\mathbf{p}, \mathbf{p}') = \exp\left[-2\sigma_b^2 \varkappa^2 \sin^2\left(\frac{\varphi'_p - \varphi_p}{2}\right)\right]. \tag{D.11}$$

Inserting now Eq. (D.11) into Eq. (D.3) and performing the p_z and p'_z integrations with the help of the functions $a^*_{\varkappa m p_z}(\mathbf{p})$ and $a_{\varkappa m p_z}(\mathbf{p}')$ leads to the desired result (D.2).

E. Evaluation of Density Matrix Averaged over Impact Parameter: Part B

In this section of the Appendix, we will show how one can evaluate the φ_p-integration in the density matrix (6.24) for the process of radiative recombination with twisted electrons. As a reminder, the density matrix is given as:

$$\langle \mathbf{k}\lambda |\, \widehat{\rho}_\gamma^{\rm tw}\, | \mathbf{k}\lambda' \rangle \propto \int_0^{2\pi} M_{\mathbf{p}}^{\rm pl,*}(\mathbf{k},\lambda)\, M_{\mathbf{p}}^{\rm pl}(\mathbf{k},\lambda')\, {\rm d}\varphi_p . \tag{E.1}$$

Inserting the explicit form (6.11) of the (plane-wave) transition amplitudes and the helicity vector (2.32) leads to

$$\langle \mathbf{k}\lambda |\, \widehat{\rho}_\gamma^{\rm tw}\, | \mathbf{k}\lambda' \rangle \propto \int_0^{2\pi} \frac{(\mathbf{e}_{\mathbf{k}\lambda}\cdot\mathbf{p})(\mathbf{e}_{\mathbf{k}^*\lambda'}\cdot\mathbf{p})}{\left(p^2+k^2-2\varkappa k\sin\theta_k\cos(\varphi_p-\varphi_k)-2p_z k\cos\theta_k+Z^2\right)^4}\,{\rm d}\varphi_p \tag{E.2}$$

with

$$\varkappa = p\sin\theta_p\,, \quad p_z = p\cos\theta_p . \tag{E.3}$$

Let us now focus on the nominator of the integrand in Eq. (E.2):

$$\begin{aligned} \mathcal{M}(\varphi_p,\varphi_k) &= (\mathbf{e}_{\mathbf{k}\lambda}\cdot\mathbf{p})(\mathbf{e}^*_{\mathbf{k}\lambda'}\cdot\mathbf{p}) \\ &= \mathcal{M}_{\rm g}(\varphi_p-\varphi_k)+\mathcal{M}_{\rm u}(\varphi_p-\varphi_k), \end{aligned} \tag{E.4}$$

where

$$\begin{aligned} \mathcal{M}_{\rm g}(\varphi_p-\varphi_k) = p^2\,\frac{\lambda\lambda'}{2}\big[&(\sin^2\theta_k\cos^2\theta_p+\lambda\lambda'\sin^2\theta_p) \\ &-(1/2)\sin(2\theta_k)\sin(2\theta_p)\cos(\varphi_p-\varphi_k) \\ &(\cos^2\theta_k\sin^2\theta_p-\lambda\,\lambda')\cos^2(\varphi_p-\varphi_k)\big] \end{aligned} \tag{E.5}$$

and

$$\mathcal{M}_{\mathrm{u}}(\varphi_p-\varphi_k) = p^2\,\frac{\lambda\lambda'}{2}\big[\mathrm{i}(\lambda-\lambda')\sin^2\theta_p\cos\theta_k\sin(\varphi_p-\varphi_k)\cos(\varphi_p-\varphi_k) \\ \mathrm{i}(\lambda'-\lambda)\sin\theta_p\sin\theta_k\cos\theta_p\sin(\varphi_p-\varphi_k)\big]. \tag{E.6}$$

Applying the simple substitution $\varphi_p \to \varphi_p + \varphi_k$ and using that the integrand is periodic in φ_p with period 2π show that the density matrix is independent of φ_k:

$$\langle \mathbf{k}\lambda|\,\widehat{\rho}_\gamma^{\mathrm{tw}}\,|\mathbf{k}\lambda'\rangle \propto \int_0^{2\pi} \frac{\mathcal{M}_{\mathrm{g}}(\varphi_p)+\mathcal{M}_{\mathrm{u}}(\varphi_p)}{\left(p^2+k^2-2\varkappa k\sin\theta_k\cos(\varphi_p)-2p_z k\cos\theta_k+Z^2\right)^4}\,\mathrm{d}\varphi_p. \tag{E.7}$$

Such an insensitivity to φ_k is expected, since the overall system of atomic target and electron beam in the RR process is spherically symmetric. Since $\mathcal{M}_{\mathrm{u}}(\varphi_p)$ is an odd function in φ_p, i.e. $\mathcal{M}_{\mathrm{u}}(-\varphi_p) = \mathcal{M}_{\mathrm{u}}(\varphi_p)$, it does not contribute to the integral, so that we are left with (after re-arranging the denominator)

$$\langle \mathbf{k}\lambda|\,\widehat{\rho}_\gamma^{\mathrm{tw}}\,|\mathbf{k}\lambda'\rangle \propto \int_0^{2\pi} \frac{\mathcal{M}_{\mathrm{g}}(\varphi_p)}{\left(p^2+k^2-2p_z k\cos\theta_k+Z^2-2\varkappa k\sin\theta_k\cos(\varphi_p)\right)^4}\,\mathrm{d}\varphi_p. \tag{E.8}$$

From the form (E.5) of $\mathcal{M}_{\mathrm{g}}(\varphi_p)$ follows that in Eq. (E.8) we need to evaluate integrals of the following form:

$$\mathcal{I}_k = \int_0^{2\pi} \frac{\cos^k(\varphi_p)}{(1-u\,\cos\varphi_p)^4}\,\mathrm{d}\varphi_p\,,\ k=0,1,2, \tag{E.9}$$

with

$$u = \frac{2pk}{v}\sin\theta_p\,\sin\theta_k,\ 0\le u<1, \tag{E.10}$$

$$v = p^2+k^2-2pk\cos\theta_p\cos\theta_k+Z^2,\ 0<v. \tag{E.11}$$

The integrals (E.9) can be evaluated by standard integration techniques [108]:

$$\mathcal{I}_0 = \frac{2+3u^2}{2(1-u^2)^{7/2}},\quad \mathcal{I}_1 = \frac{4u+u^3}{2(1-u^2)^{7/2}},\quad \mathcal{I}_2 = \frac{1+4u^2}{2(1-u^2)^{7/2}}. \tag{E.12}$$

Inserting the results (E.12) into Eq. (E.13) gives

$$\langle \mathbf{k}\lambda |\, \widehat{\rho}_{\gamma}^{\,\mathrm{tw}}\, | \mathbf{k}\lambda' \rangle \propto A(\mathbf{k}) + \lambda\, \lambda' B(\mathbf{k}), \tag{E.13}$$

where

$$A(\mathbf{k}) = \frac{1}{2v^4}(\mathcal{I}_0 - \mathcal{I}_2)\, \sin^2(\theta_p), \tag{E.14}$$

$$B(\mathbf{k}) = \frac{1}{2v^4}\big(\mathcal{I}_0\, \sin^2\theta_k \cos^2\theta_p - (1/2)\,\mathcal{I}_1\, \sin(2\theta_k)\, \sin(2\theta_p) + \mathcal{I}_2 \cos^2\theta_k \sin^2\theta_p\big). \tag{E.15}$$

or equivalently, as we have written in Eq. (6.26),

$$A(\mathbf{k}) = \frac{1}{4v^4(1-u^2)^{7/2}}\left(1-u^2\right)\sin^2\theta_p, \tag{E.16}$$

$$\begin{aligned} B(\mathbf{k}) = \frac{1}{8v^4(1-u^2)^{7/2}}\Big[&2\left(2+3u^2\right)\sin^2\theta_k\cos^2\theta_p - \left(4u+u^3\right)\sin 2\theta_k \sin 2\theta_p \\ &+ 2\left(1+4u^2\right)\cos^2\theta_k \sin^2\theta_p\Big]. \end{aligned} \tag{E.17}$$

Danksagung (Acknowledgements)

Eine Doktorarbeit ist kein Einzelprojekt—es gibt zahlreiche Menschen, die einen bei diesem Projekt unterstützen, einen während dieser Zeit begleiten, und einem mit Rat und Tat zur Seite stehen. Der folgende Abschnitt ist diesen Menschen gewidmet, denen ich hiermit meinen Dank ausdrücken möchte.

Zutiefst danke ich meinem Doktorvater Andrey Surzhykov für die spannenden und abwechslungsreichen Aufgaben, die ich im Rahmen meiner Doktorarbeit bearbeiten durfte, sowie für die hervorragende Betreuung. Mit Freude denke ich auch an die zahlreichen Konferenzen zurück, die er mir ermöglicht hat. Ebenso möchte ich mich bei meinem Zweitbetreuer Stephan Fritzsche für seine stets wertvolle Hilfe und die zahlreichen persönlichen und wissenschaftlichen Gespräche bedanken. Ich danke außerdem Antonino DiPiazza, dass er sich bereit erklärt hat, einer der Gutachter meiner Dissertation zu sein.

Weiterhin möchte ich mich bei meinen Arbeitskollegen für die schöne Zeit, die freundschaftliche Atmosphäre und die guten Gespräche bedanken. Ein großer Dank geht daher an Anton Artemyev, Armen Hayrapetyan, Chintan Shah, Daniel Seipt, Filippo Fratini, Johan Holmberg, Jonas Gunst, Lalita Sharma, Manuel Mai, Max Schwemlein, Oleksiy Kovtun, Pierre-Michel Hillenbrand, Robert Müller, Sean McConnel, Stanislav Tashenov, Stefan Kraft, Thorsten Jahrsetz, Valeriy Serbo, Walter Hahn und Zhongwen Wu.

Herzlichst danke ich auch Bastian Märkisch und seiner Arbeitsgruppe für ihre Gastfreundschaft. Vielen Dank an Carmen Ziener, Christoph Roick, Henry Carrera, Holger Mest und Nataliya Reborva.

Ein großer Dank gebührt auch der “Helmholtz Graduate School for Hadron and Ion Research” sowie der “Heidelberg Graduate School of Fundamental Physics”, die mir durch Finanzierungsmöglichkeiten von Forschungs- und Konferenzaufenthalten sowie durch interessante Lehrveranstaltungen eine ansprechende und erfüllende Doktorandenzeit ermöglicht haben.

Ebenfalls möchte ich Lorenz Milla danken. Er war mir ein wertvoller Gesprächspartner und stand mir insbesondere mit seinem Wissen über Integralberechnungen zur Seite.

Kolja Szillat danke ich für das Korrekturlesen meiner Arbeit.

Ganz besonders danke ich meiner Freundin Xiaojun Xu, die mich durch ein selbst entwickeltes Spiel täglich aufs Neue dazu gebracht hat, motiviert und erfolgreich an dieser Arbeit zu schreiben.

Einen persönlichen Dank verdient meine Familie für ihre Fürsorge und finanzielle Unterstützung. Ich danke herzlichst meinen Großeltern Christa und Wolfgang Spieth sowie Irmgard und Max Matula, meiner Schwester Sarah Matula und besonders meinen Eltern Sylvia und Michael Matula.

List of Figures

List of Tables

Bibliography

[1] J. H. Poynting, Proc. R. Soc. Lond. A **82**, 560 (1909).

[2] R. A. Beth, Phys. Rev. **50**, 115 (1936).

[3] H. J. Metcalf and P. van der Straten, *Laser Cooling and Trapping* (Springer-Verlag, New York, 1999).

[4] W. D. Phillips, Rev. Mod. Phys. **70**, 721 (1998).

[5] M. A. Nielsen and I. L. Chuang, *Quantum Computation and Quantum Information* (Cambridge Univ. Press, Cambridge, 2000).

[6] C. H. Bennett, F. Bessette, G. Brassard, L. Salvail, and J. Smolin, J. Cryptology **5**, 3 (1992).

[7] A. Muller, J. Breguet, and N. Gisin, Europhys. Lett. **23**, 383 (1993).

[8] J. Chen, W. Cranton, and M. Fihn, *Handbook of Visual Display Technology* (Springer, Berlin/Heidelberg, 2012).

[9] L. Allen, M. W. Beijersbergen, R. J. C. Spreeuw, and J. P. Woerdman, Phys. Rev. A **45**, 8185 (1992).

[10] M. W. Beijersbergen, L. Allen, H. E. L. O. van der Veen, and J. P. Woerdman, Opt. Commun. **96**, 123 (1993).

[11] M. W. Beijersbergen, R. P. C. Coerwinkel, M. Kristensen, and J. P. Woerdman, Opt. Commun. **112**, 321 (1994).

[12] L. Marucci, C. Manzo, and D. Paparo, Phys. Rev. Lett. **96**, 163905 (2006).

[13] E. Karimi, B. Piccirillo, E. Nagali, L. Marrucci, and E. Santamato, Appl. Phys. Lett. **94**, 231124 (2009).

[14] J. Arlt and K. Dholakia, Opt. Commun. **177**, 297 (2000).

[15] N. V. Bloch, K. Shemer, A. Shapira, R. Shiloh, I. Juwiler, and A. Arie, Phys. Rev. Lett. **108**, 233902 (2012).

[16] X. Cai *et al.*, Science **338**, 363 (2012).

[17] J. Bahrdt, K. Holldack, P. Kuske, R. Müller, M. Scheer, and P. Schmid, Phys. Rev. Lett. **111**, 034801 (2013).

[18] E. Hemsing, A. Knyazik, M. Dunning, D. Xiang, A. Marinelli, C. Hast, and J. B. Rosenzweig, Nat. Phys. **9**, 549 (2013).

[19] V. Y. Bazhenov, M. S. Soskin, and M. V. Vasnetsov, J. Mod. Opt. **39**, 985 (1992).

[20] N. R. Heckenberg, R. McDuff, C. P. Smith, and A. G. White, Optics Lett. **17**, 221 (1992).

[21] F. S. Roux, Applied Optics **32**, 4191 (1993).

[22] C. Paterson, J. Mod. Optics **41**, 757 (1994).

[23] J. E. Curtis, B. A. Koss, and D. G. Grier, Opt. Commun. **207**, 169 (2002).

[24] M. Padgett, J. Courtial, and L. Allen, Phys. Today **57**, 35 (2004).

[25] Y. Shen, G. T. Campbell, B. Hage, H. Zou, B. C. Buchler, and P. K. Lam, J. Opt. **15**, 044005 (2013).

[26] U. D. Jentschura and V. G. Serbo, Phys. Rev. Lett. **106**, 013001 (2011).

[27] U. D. Jentschura and V. G. Serbo, Eur. Phys. J. C **71**, 1571 (2011).

[28] H. H. Arnaut and G. A. Barbosa, Phys. Rev. Lett. **85**, 286 (2000).

[29] J. Leach, M. J. Padgett, S. M. Barnett, S. Franke-Arnold, and J. Courtial, Phys. Rev. Lett. **88**, 257901 (2002).

[30] J. Leach, J. Courtial, K. Skeldon, S. M. Barnett, S. Franke-Arnold, and M. J. Padgett, Phys. Rev. Lett. **92**, 013601 (2004).

[31] C. S. Wu and I. Shaknov, Phys. Rev. **77**, 136 (1950).

[32] Y. H. Shih, A. V. Sergienko, M. H. Rubin, T. E. Kiess, and C. O. Alley, Phys. Rev. A **50**, 23 (1994).

[33] D. Bouwmeester, J.-W. Pan, K. Mattle, M. Eibl, H. Weinfurter, and A. Zeilinger, Nature **390**, 575 (1997).

[34] A. Mair, A. Vaziri, G. Weihs, and A. Zeilinger, Nature **412**, 313 (2001).

[35] A. Vaziri, J.-W. Pan, T. Jennewein, G. Weihs, and A. Zeilinger, Phys. Rev. Lett. **91**, 227902 (2003).

[36] R. Fickler, R. Lapkiewicz, W. N. Plick, M. Krenn, C. Schaeff, S. Ramelow, and A. Zeilinger, Science **338**, 640 (2012).

[37] M. P. Lavery, F. C. Speirits, S. M. Barnett, and M. J. Padgett, Science **341**, 537 (2013).

[38] H. He, M. E. J. Friese, N. R. Heckenberg, and H. Rubinsztein-Dunlop, Phys. Rev. Lett. **75**, 826 (1995).

[39] M. E. J. Friese, T. A. Nieminen, N. R. Heckenberg, and H. Rubinsztein-Dunlop, Nature **394**, 348 (1998).

[40] G. Gibson, J. Courtial, M. Padgett, M. Vasnetsov, V. Pas'ko, S. M. Barnett, and S. Franke-Arnold, Opt. Express **12**, 5448 (2004).

[41] F. Tamburini, E. Mari, A. Sponselli, B. Thidé, A. Bianchini, and F. Romanato, New J. Phys. **14**, 033001 (2012).

[42] J. Wang, J.-Y. Yang, I. M. Fazal, N. Ahmed, Y. Yan, H. Huang, Y. Ren, Y. Yue, S. Dolinar, M. Tur, and A. E. Willner, Nature Photon. **6**, 488 (2012).

[43] N. Bozinovic, Y. Yue, Y. Ren, M. Tur, P. Kristensen, H. Huang, A. E. Willner, and S. Ramachandran, Science **340**, 1545 (2013).

[44] K. Y. Bliokh, Y. P. Bliokh, S. Savel'ev, and F. Nori, Phys. Rev. Lett. **99**, 190404 (2007).

[45] M. Uchida and A. Tonomura, Nature (London) **464**, 737 (2010).

[46] P. Schattschneider, M. Stöger-Pollach, and J. Verbeeck, Phys. Rev. Lett. **109**, 084801 (2012).

[47] J. Verbeeck, H. Tian, and P. Schattschneider, Nature (London) **467**, 301 (2010).

[48] J. Verbeeck, H. Tian, and A. Béché, Ultramicroscopy **113**, 83 (2012).

[49] J. Verbeeck, P. Schattschneider, S. Lazar, M. Stöger-Pollach, S. Löffler, A. Steiger-Thirsfeld, and G. Van Tendeloo, Appl. Phys. Lett. **99**, 203109 (2011).

[50] P. Schattschneider, M. Stöger-Pollach, S. Löffler, A. Steiger-Thirsfeld, J. Hell, J. Verbeeck, Ultramicroscopy **115**, 21 (2012).

[51] K. Saitoh, Y. Hasegawa, N. Tanaka, and M. Uchida, J. Electron Microsc. **61**, 171 (2012).

[52] B. J. McMorran, A. Agrawal, I. M. Anderson, A. A. Herzing, H. J. Lezec, J. J. McClelland, and J. Unguris, Science **331**, 192 (2011).

[53] G. M. Gallatin and B. McMorran, Phys. Rev. A **86**, 012701 (2012).

[54] K. Y. Bliokh, P. Schattschneider, J. Verbeeck, and F. Nori, Phys. Rev. X **2**, 041011 (2012).

[55] C. Greenshields, R. L. Stamps, and S. Franke-Arnold, New J. Phys. **14**, 103040 (2012).

[56] I. G. da Paz, P. L. Saldanha, M. C. Nemes, and J. G. Peixoto de Faria, New J. Phys. **13**, 125005 (2011).

[57] G. Guzzinati, P. Schattschneider, K. Y. Bliokh, F. Nori, and J. Verbeeck, Phys. Rev. Lett. **110**, 093601 (2013).

[58] E. Karimi, L. Marrucci, V. Grillo, and E. Santamato, Phys. Rev. Lett. **108**, 044801 (2012).

[59] K. Y. Bliokh and F. Nori, Phys. Rev. Lett. **108**, 120403 (2012).

[60] M. Babiker, C. R. Bennet, D. L. Andrews, and L. C. D. Romero, Phys. Rev. Lett. **89**, 143601 (2002).

[61] A. Afanasev, C. E. Carlson, and A. Mukherjee, Phys. Rev. A **88**, 033841 (2013).

[62] B. S. Davis, L. Kaplan, and J. H. McGuire, J. Opt. **15**, 035403 (2013).

[63] S. M. Lloyd, M. Babiker, and J. Yuan, Phys. Rev. Lett. **108**, 074802 (2012).

[64] S. M. Lloyd, M. Babiker, and J. Yuan, Phys. Rev. A **86**, 023816 (2012).

[65] A. Picón, J. Mompart, J. R. V. de Aldana, L. Plaja, G. F. Calvo, and L. Roso, Opt. Express **18**, 3660 (2010).

[66] A. Picón, A. Benseny, J. Mompart, J. R. V. de Aldana, L. Plaja, G. F. Calvo, and L. Roso, New J. Phys. **12**, 083053 (2010).

[67] A. M. Yao and M. J. Padgett, Adv. Opt. Photon. **3**, 161 (2011).

[68] O. Matula, A. G. Hayrapetyan, V. G. Serbo, A. Surzhykov, and S. Fritzsche, J. Phys. B **46**, 2050022 (2013).

[69] E. Cartlidge, *How light can put atoms in a twist*, accessed January 12, 2014, http://physicsworld.com/cws/article/news/2013/oct/15/how-light-can-put-atoms-in-a-twist.

[70] H. A. Bethe and E. E. Salpeter, *Quantum Mechanics of One- and Two-Electron Atoms* (Springer, Berlin, 1957).

[71] B. H. Bransden and C. J. Joachain, *Physics of Atoms and Molecules*, 2nd ed. (Pearson, Harlow, 2003).

[72] G. W. F. Drake, *Atomic, Molecular & Optical Physics Handbook*, 2nd ed. (Springer, New York, 2006).

[73] J. Eichler and Th. Stöhlker, Phys. Rep. **439**, 1 (2007).

[74] R. H. Pratt, R. D. Levee, R. L. Pexton, and W. Aron, Phys. Rev. **134**, A916 (1964).

[75] A. Ichihara and J. Eichler, At. Data Nucl. Data Tables **74**, 1 (2000).

[76] S. V. Popruzhenko, V. D. Mur, V. S. Popov, and D. Bauer, Phys. Rev. Lett. **101**, 193003 (2008).

[77] W.-C. Chu, H.-L. Zhou, A. Hibbert, and S. T. Manson, J. Phys. B **42**, 205003 (2009).

[78] M. A. Bautista, P. Romano, and A. K. Pradhan, ApJS **118**, 259 (1998).

[79] W. R. Johnson and K. T. Cheng, Phys. Rev. A **20**, 978 (1979).

[80] K.-N. Huang, Phys. Rev. A **22**, 223 (1980).

[81] A. Ichihara and J. Eichler, At. Data Nucl. Data Tables **79**, 187 (2001).

[82] S. Fritzsche, A. N. Grum-Grzhimailo, E. V. Gryzlova, and N. M. Kabachnik, J. Phys. B **41**, 165601 (2008).

[83] W. Spies *et al.*, Phys. Rev. Lett. **69**, 2768 (1992).

[84] Th. Stöhlker *et al.*, Phys. Rev. Lett. **85**, 3109 (2000).

[85] A. Gumberidze *et al.*, Phys. Rev. Lett. **94**, 223001 (2005).

[86] R. Reuschl *et al.*, Phys. Rev. A **77**, 032701 (2008).

[87] D. A. Knapp, P. Beiersdorfer, M. H. Chen, J. H. Scofield, and D. Schneider, Phys. Rev. Lett. **74**, 54 (1995).

[88] J. H. Scofield, Phys. Rev. A **40**, 3054 (1989).

[89] S. Fritzsche, A. Surzhykov, and Th. Stöhlker, Phys. Rev. A **72**, 012704 (2005).

[90] J. Eichler, A. Ichihara, and T. Shirai, Phys. Rev. A **51**, 3027 (1995).

[91] Th. Stöhlker *et al.*, Phys. Scr. **2004**, 384 (2004).

[92] A. Surzhykov, S. Fritzsche, and Th. Stöhlker, Phys. Lett. A **289**, 213 (2001).

[93] A.Surzhykov, S. Fritzsche, Th. Stöhlker, and S. Tashenov, Phys. Rev. A **68**, 022710 (2003).

[94] S. Tashenov *et al.*, Phys. Rev. Lett. **97**, 223202 (2006).

[95] C. Maxwell, *Treatise on Electricity and Magnetism* 1st vol. (Oxford Univ. Press, London, 1873).

[96] J. D. Jackson, *Klassische Elektrodynamik*, 4th ed. (de Gruyter, Berlin, 2006).

[97] D. J. Griffiths, *Introduction to Electrodynamics*, 4th ed. (Pearson, Harlow, 2012).

[98] L. Grafakos, *Classical Fourier Analysis*, 2nd ed. (Springer, New York, 2008).

[99] M. E. Rose, *Multipole Fields* (Wiley, New York, 1955).

[100] A. I. Akhiezer and V. B. Berestetskii, *Quantum Electrodynamics* (Interscience, New York, 1965).

[101] S. J. van Enk and G. Nienhuis, Europhys. Lett. **25**, 497 (1994); J. Mod. Opt. **41**, 963 (1994).

[102] S. M. Barnett and L. Allen, Opt. Commun. **110**, 670 (1994).

[103] S. M. Barnett, J. Opt. B: Quantum and Semiclass. Opt. **4**, S7 (2002).

[104] S. M. Barnett, J. Mod. Opt. **57**, 1339 (2010).

[105] E. Leader and C. Lorcé, arxiv:1309.4235 (2013).

[106] M. E. Rose, *Elementary Theory of Angular Momentum* (Dover, New York, 1995).

[107] J. Durnin, J. J. Miceli, and J. H. Eberly, Phys. Rev. Lett. **58**, 1499 (1987).

[108] M. Abramowitz and I. A. Stegun, *Handbook of Mathematical Functions* (Dover, New York, 1970).

[109] A. Afanasev, C. E. Carlson, and A. Mukherjee, arxiv:1401.1227 (2014).

[110] E. Schrödinger, Phys. Rev. **28**, 1049 (1926).

[111] L. D. Landau and E. M. Lifshitz, *Quantum Mechanics (Non-Relativistic Theory): Volume 3*, 3rd ed. (Butterworth-Heinemann, Oxford, 1976).

[112] C. Cohen-Tannoudji, B. Diu, F. Laloë, *Quantum Mechanics: Volume One* (Wiley, New York, 1977).

[113] C. Cohen-Tannoudji, B. Diu, F. Laloë, *Quantum Mechanics: Volume Two* (Wiley, New York, 1977).

[114] R. Omnès, *Understanding Quantum Mechanics* (Princeton University Press, Princeton, New Jersey, 1999).

[115] J. J. Sakurai and J. Napolitano, *Modern Quantum Mechanics*, 2nd ed. (Prentice Hall, New Jersey, 2007).

[116] P. Schattschneider and J. Verbeeck, Ultramicroscopy **111**, 1461 (2011).

[117] V. V. Balashov, A. N. Grum.-Grzhimailo, and N. M. Kabachnik, *Polarization and Correlation Phenomena in Atomic Collisions*, (Kluwer, New York, 2000).

[118] B. Podolsky and L. Pauling, Phys. Rev. **34**, 109 (1929).

[119] W. Rudin, *Real and Complex Analysis* (McGraw-Hill, New York, 1987).

[120] K. Blum, *Density Matrix Theory and Applications*, 3rd ed. (Springer, New York, 2012).

[121] I. Peschel, X. Wang, M. Kaulke, and K. Hallberg, *Density-Matrix Renormalization*, (Springer, New York, 1999).

[122] O. Matula, A. G. Hayrapetyan, V. G. Serbo, A. Surzhykov, and S. Fritzsche, arXiv:1401.1646 (2014), submitted to New J. Phys.

[123] M. A. Wilson *et al.*, Phys. Rev. Lett. **91**, 213602 (2003).

[124] J. Eschner, Eur. Phys. J. D **22**, 341 (2003).

[125] B. Murphy and L. V. Hau, Phys. Rev. Lett. **102**, 033003 (2009).

[126] J. R. Swanson and L. Armstrong, Phys. Rev. A **15**, 661 (1977).

[127] M. Kitzler, J. Zanghellini, Ch. Jungreuthmayer, M. Smits, A. Scrinzi, and T. Brabec, Phys. Rev. A **70**, 041401 (2004).

[128] J. Caillat, J. Zanghellini, M. Kitzler, O. Koch, W. Kreuzer, and A. Scrinzi, Phys. Rev. A **71**, 012712 (2005).

[129] W. Li, W. Xu, and T. Chu, Comp. Theor. Chem. **1004**, 18 (2013).

[130] J. C. Slater and G. F. Koster, Phys. Rev. **94**, 1498 (1954).

[131] F. O. Ellison and H. Shull, J. Chem. Phys. 23, 2348 (1955).

[132] B. J. Ransil, Rev. Mod. Phys. **32**, 245 (1960).

[133] M. Born and E. Wolf, *Principles of Optics* (Pergamon, Oxford, 1980).

[134] O. S. Heavens and R. W. Ditchburn, *Insight into Optics* (Wiley, New York, 1991).

[135] J. Eichler, *Lectures on Ion-Atom Collisions* (Elsevier, Amsterdam, 2005).

[136] I. P. Grant, *Relativistic Quantum Theory of Atoms and Molecules* (Springer, New York, 2007).

[137] K. Y. Bliokh, M. R. Dennis, and F. Nori, Phys. Rev. Lett. **107**, 174802 (2011).

[138] D. V. Karlovets, Phys. Rev. A **86**, 062102 (2012).

[139] A. G. Hayrapetyan, O. Matula, A. Aiello, A. Surzhykov and S. Fritzsche, *to be published in* Phys. Rev. Lett.

[140] I. P. Ivanov, Phys. Rev. D **83**, 093001 (2011).

[141] I. P. Ivanov and V. G. Serbo, Phys. Rev. A **84**, 033804 (2011).

[142] I. P. Ivanov, Phys. Rev. A **85**, 033813 (2012).

[143] I. P. Ivanov, Phys. Rev. D **85**, 076001 (2012).

[144] M. E. Peskin and D. V. Schroeder, *Quantum Field Theory* (Perseus Book, New York, 1995).

[145] P. R. Halmos, *Finite Dimensional Vector Spaces*, 2nd ed. (Princeton University Press, Princeton, New Jersey, 1947).

[146] J. A. Tough and A. J. Stone, J. Phys. A **10**, 1261 (1977).

[147] N. M. Temme, *Special Functions: an Introduction to the Classical Functions of Mathematical Physics*, 2nd ed. (Wiley, New York, 1996).